Quantitative methods for MRI-microscopy comparisons

Daniel Z.L. Kor

St. Peter's College

University of Oxford

A thesis submitted for the degree of

Doctor of Philosophy

Michaelmas 2023

Acknowledgements

It is said that it takes a village to raise a child. For me, it felt like an entire country. Here, I aim to sincerely express my immense gratitude to a tiny subset of that country.

To my first supervisor and "academic mother", Professor Karla Miller, thank you so much for trusting and guiding me through this whole journey. Your professionalism, since the first email, was truly exemplary, balanced only by your deep compassion and care. I will never forget how you were always willing to ensure that I obtained the supervision I needed, even meeting me twice a week at one point in time. Thank you for always keeping me on track to the destination, and for never giving up on me.

To my other primary supervisor and "academic sister", Dr. Amy Howard; thank you for being the stablising presence in my turbulent day-to-day DPhil struggle. I have always said this, and I will say it again—I wouldn't have finished my DPhil without you agreeing to supervise me midway through my DPhil. Your patience in answering all my stupid questions carried me through my daily struggles, while your foresight and wisdom ensured that I stayed on the path to graduate, even till the very end. Thank you for always believing in me.

To my secondary supervisor Professor Saad Jbabdi, thank you for being the person to walk me through the mathematics and statistics whenever I needed it. Although our interactions may not have been the longest or most frequent, I fondly remember how they have greatly illuminated and clarified. Thank you for having my back throughout this whole degree.

I also could not have asked for better colleagues. Hossein, I will look back fondly at all of our experiences together (e.g. Iranian new year and the Wolfson BOPs), the inquisitive and stimulating conversations we have had, and all the times you spent teaching me BENCH. To the hotel gang, Thijs and James, thank you for all the wonderful memories of ISMRM, punting during the platty jubes, and watching the epic 3-hour baseball game. Cristiana, thank you for all the times we've spent playing board games, and for all the conversations we have had. It was truly wonderful seeing you navigate your incredibly broad project and grow as a

researcher. Xi, thank you for your spontaneity and caring for Joanne. Ying-qiu, your selfless gestures, especially the beautiful wedding video, are etched in my heart. To all the other students who made this journey fascinating: Silei, Qijia, Ziyu, Zhiyu, Xinyu, Hongwei, and Qianwen, thank you making every step much more interesting and memorable.

There were others in WIN and NDCN who have supported me. Jeroen, thank you for onboarding me onto this project. Istvan, I aspire to one day have your deep technical understanding (especially with image co-registration) and willingness always to help. Adele, your expertise in pathology and patience in curating data are extremely admirable. Menuka, thank you for always having the time to answer my questions about pathology. And Michiel, in my eyes, you will always be the genius with clear and concise answers to anything related to physics and mathematics. Thank you for always being so patient with me when explaining what you mean.

My journey would not have even started without the support I have received from my undergraduate years in Vancouver. To Jamie and Henry, thank you for always balancing me and forcing me to socialise even though I was not the easiest to invite. To my Engineering Physics friends, Angela, Cornell, Andrew, Andy, and Candice, thank you for dragging me through the constant onslaught of assignments and teaching me whenever I was in doubt. Without you all, I wouldn't even have made the grades to enter my DPhil program. To Professors Vladan Jovovic and Kristin Schleich, thank you for being the best possible physics teachers. You both changed my life.

Throughout these years, the Lord has been my Shepherd. Sometimes, this was conveyed through my fellow brothers and sisters in Christ. Chi Yang, thank you for being my companion and always being there to catch up. David and Queenie, if it wasn't for you both, I'm not sure where I will be today. Thank you both for showing me that it is possible to love someone in Christ. Thank you, Yashua, for showing me what it means to pray with others, and for cherishing me in my soul. To Jessica, Boyang, Esther and Bethany, thank you being a family away from home. Your care in your cooking and driving to-and-from Reading is truly appreciated. To Richard, Ching and Abigail, thank you all for your cherishing and nourishing over the past year. And finally, Bernard and Lynn, I will always treasure how you both have consistently prayed with and for me.

I am simply a product of my family, who have always opened their home to anyone who needed a meal. Pa, thank you for inspiring me to professionally be the person I am today, and for always supporting me. I know we argue sometimes, but I deeply

appreciate that I am comfortable to speak my mind with you. Mom, thank you for shaping how I think and care for people. What I have learnt from you is worth more than any degree. To Joseph and Zhen Qin, your willingness to take me in during the COVID pandemic, undoubtedly the hardest time in my degree, and care for me and Joanne, has allowed me to finish this degree. David and Paula, I appreciate your thoughtfulness and reaching out to care for us. And to my nieces, watching you both grow has been an absolute joy.

I end this acknowledgement with my wife and "co-DPhil" holder, Joanne. This DPhil is equally yours, for I would not have finished this program without you. Thank you for your pure love, care, and support over our last 2.5 years of marriage together, not to mention your willingness to uproot yourself and move over to the UK. While it has not been easy for you, your adaptability to a new community and environment deeply inspires me. I thank the Lord for having you as my soulmate, and I can't wait to grow together with you in the next phase of our lives.

Thank you, Lord Jesus.

Abstract

Magnetic resonance imaging (MRI) is a powerful tool for the in-vivo diagnosis and assessment of neurodegenerative disorders. While numerous MRI techniques have yielded parameters sensitive to microstructural changes in the brain, MRI parameters are infamously non-specific. Different changes in brain tissue structure may result in the same change in MRI signal, making it challenging to pinpoint the exact source of these signal changes.

Biophysical modelling aims to achieve better biological specificity by relating dMRI signals to biologically interpretable tissue parameters. Yet, the fitting of these complex models with many parameters to unremarkable dMRI signals is challenging, often resulting in a degeneracy where multiple combinations of parameters explain the dMRI signal equally well.

Conversely, microscopy offers high biological specificity by targetting specific aspects of microstructure. By acquiring and relating MRI and microscopy metrics for the same tissue section, one can therefore leverage microscopy's specificity to elucidate the microstructural basis of MRI signal change. However, microscopy is incredibly time-intensive, restricting examination to a few tissue sections at a time. A significant gap remains in the lack of a standardised pipeline for MRI-microscopy comparisons, with existing methods necessitating substantial manual intervention.

This thesis delves into methods that enhance MRI-microscopy comparisons. Specifically, we introduce an automated pipeline that rapidly and reliably extracts multiple quantitative microscopy parameters from sections that are histologically-stained. Utilising this pipeline alongside high-quality MRI-microscopy co-registrations, we performed whole-slide voxelwise comparisons between multimodal MRI- and microscopy-derived metrics. Finally, we present an alternative analysis method designed to relate degenerate biophysical model parameters to a continuous metric (e.g. from microscopy).

Overall, the techniques outlined in this thesis are intended to facilitate a more precise interpretation of microstructural change from MRI parameters and encourage a more systematic approach to processing microscopy data when relating them to MRI data.

Contents

List of Figures

1

Introduction

Contents

The human brain has always been an enigma, a complex network of billions of neurons and glial cells that hold the secrets of our thoughts, actions, and emotions. Since the ancient Egyptians [1], theories have been proposed about the function of the brain. However, it was the advent of microscopy in the 1600s and its evolution that ultimately offered a window to the brain's microscopic components. By the late 19th century, Santiago Ramón y Cajal used the Golgi stain [2] to discern individual neurons. Around the same time, Korbinian Brodmann examined the variations in the density and organisation of these neurons—the cytoarchitecture—across different brain regions with Nissl staining. His pioneering work culminated in the 52 Brodmann areas [3], which are still used to this day.

Microscopy of the brain has developed substantially over the years with its use of different staining techniques, fluorescent dyes, electron microscopy, and two-photon microscopy [4]–[6], offering unparalleled specificity in identifying and localising

cellular structures. A commonly used histological staining technique is immunohistochemistry (IHC). IHC uses antibodies to stain target proteins with high specificity, which provide important, albeit qualitative, information about tissue function, structure, and health [6]. However, IHC, like many microscopy techniques, is ultimately limited to ex-vivo tissue sections. Further, IHC is often only performed on a few tissue samples due to its time-intensive nature, making it difficult to investigate between-subject variability.

In the 1970s, Paul Lauterbur and Sir Peter Mansfield conceptualised and developed magnetic resonance imaging (MRI) [7]. Lauterbur pioneered the application of spatially-varying magnetic fields to create images. Meanwhile, Mansfield introduced mathematical methods and innovative acquisition protocols that accelerated the imaging process, paving the way for MRI's widespread use in the clinic and in research. Unlike earlier imaging techniques, MRI offered an in-vivo and non-invasive window into the complexities of the brain, enabling the investigation of brain structure and function across many subjects. MRI's advent marked a paradigm shift in both basic and clinical neuroscience, generating numerous sub-disciplines, each focused on elucidating different facets of the brain.

However, while MRI has proven to be sensitive to subtle differences at the cellular level, a significant challenge remains: it lacks specificity. Though MRI can detect changes in brain tissue, it often cannot pinpoint the exact source or nature of those changes. This issue in specificity is due to different changes in brain tissue structure resulting in the same change in MRI signal [8], [9]. For instance, the diffusion MRI (dMRI) signal is influenced by factors relating to cellular components and tissue geometry [10], [11]. Moreover, dMRI measurements are typically averaged over millimetres of tissue, posing challenges when drawing inferences about micrometre-scale processes. Thus, understanding MRI findings often requires interpreting them with caution and/or in combination with other complementary techniques.

Recently, quantitative MRI (qMRI) techniques, including relaxometry and diffusion MRI (dMRI), have advanced our pursuit for specificity by offering signals and metrics that enable comparison between subjects and across time. In other words, it is specific with respect to the MR properties it quantifies. Nevertheless, qMRI still stops short of achieving specificity at the biological level of cells: it allows us to detect changes in the cellular composition of the tissue, but it cannot ascribe that change to a specific cellular property.

Biophysical modelling of dMRI signals brings us another step closer to biological specificity; these models infer more biologically meaningful tissue parameters ("biophysical parameters") by modelling the contributions of microstructural compartments to the dMRI signal. However, typically acquired dMRI signal is often non-descriptive, yielding a flat parameter-fitting landscape. Consequently, the inferred tissue parameters are degenerate, with different sets of parameters fitting the dMRI equally well.

To elucidate the microstructural basis of MRI signal change, one can leverage the specificity of microscopy by comparing qMRI and microscopy-derived metrics acquired from the same postmortem tissue sample. Typically, MRI-microscopy comparisons are done by first 1) manually deriving a few microscopy metrics in a limited set of regions-of-interest due to its time-intensive nature, before 2) performing a simple correlation between microscopy metrics with region-matched qMRI metrics. There are limitations to each step, which we will highlight and address in the individual research chapters of this thesis.

1.1 Thesis outline

In this thesis, we explore methods to improve MRI-microscopy comparisons, enabling a more specific microstructural interpretation of MRI signals. It consists of a background chapter that overviews the basics of MRI and microscopy (**Chapter 2**),

three research chapters, and a concluding chapter presenting future directions. In the research chapters, we tackle two challenges: 1) microscopy data curation by rapidly extracting quantitative metrics reliably from IHC stains for MRI-IHC comparisons (**Chapters 3** and **4**), and 2) the relating of biophysical parameters from degenerate models to microscopy using an alternative analysis method (**Chapter 5**).

In **Chapter 3**, we introduce an automated pipeline that extracts a quantitative microscopy metric from multiple IHC stains to facilitate voxelwise MRI-IHC comparison. Crucially, this pipeline is designed to directly address IHC artefacts related to tissue staining and slide digitisation, which may otherwise confound relationships between MRI- and IHC-derived metrics. We propose data-driven methods for each processing step of the pipeline and demonstrate how they improve the analysis process relative to manual approaches.

In **Chapter 4**, we apply the automated pipeline to an IHC dataset spanning different brain regions and subjects. Utilising high-quality MRI-IHC co-registrations, we perform whole-slide voxelwise comparisons (simple correlations, partial correlations and multiple regression analyses) to disentangle how tissue features (axons, glia, etc.) influence metrics derived from MRI signal models (T_1, T_2, FA, MD). Further, the automated nature of this pipeline facilitates the processing of a large-scale dataset. We demonstrate this by applying the pipeline to 41 myelin-stained slides before relating them to their corresponding MRI parameter maps.

In **Chapter 5**, we focus on models linking dMRI signal changes to biophysical parameters. We focus on a biophysical model that requires a larger number of model parameters, which increases the likelihood of having different combinations of biophysical parameters explaining the signal equally well (i.e. a degeneracy). We overcome this degeneracy by reframing the goal: instead of fitting biophysical parameters, we infer which parameter best explains the change in the dMRI signal described by the continuous microscopy metrics. We developed and validated this

method on simulation data and then applied it to ex-vivo data, where we identified microstructural parameters linked to axons and glial cell soma.

Chapter 6 concludes this thesis with future avenues. We show the microscopy pipeline applied to other microscopy datasets (e.g. mouse brain data), and how it can be used to aid the curation of future IHC datasets. We demonstrate our alternative analysis method for overcoming model degeneracy in in-vivo data through preliminary results that link dMRI data with clinical phenotypes (e.g. blood pressure).

2

Background

Contents

2.1 Brain structure

Under the microscope, the brain is predominantly comprised of the neurons [2] and the glia [12]. Neurons, or nerve/neuronal cells, are primarily responsible for the transmission of information between brain regions. Information is transmitted via electrical impulses ("action potentials") within the neuron. This information is com-

municated with other neurons or other cells using chemicals—neurotransmitters—at junctions called synapses. Glia, or glial cells, support and protect these neuronal cells through a diverse set of roles, such as the engulfing ("phagocytosis") of foreign pathogens, the myelination of neurons for efficient information transmission, or the formation and maintenance of the blood brain barrier. In this thesis, we highlight three main glial cells: oligodendrocytes, astrocytes, and microglia.

Together, neurons and glial cells, with their different shapes and sizes, are organised in distinct arrangements to produce the brain's macroscopic architecture. This gives rise to two structurally and functionally different tissue types: white matter (WM) and grey matter (GM). The WM contains densely packed neuronal bundles wrapped with myelin sheaths that facilitate rapid information transmission across distant brain regions. The lipid-rich myelin gives WM its characteristic pale appearance. GM is typically located at the surface of the brain (i.e. cerebral cortex) and is mainly populated with the cell bodies, dendrites, and synapses of neurons. These neurons process information transmitted from neuronal bundles for complex activities, such as movement, memory, and sensory interpretation.

2.1.1 Neuron

A neuron's capability to transmit information is enabled by its specialised components—the cell body or soma, the dendrites, and the axon. The former two almost always inhabit the GM, while the axon resides in both the WM and GM. In Figure 2.1, we show a sample neuron with a myelinated axon.

The cell body or soma is the neuron's metabolic and genetic hub. It houses the nucleus, manages energy production, and regulates the cell's internal environment for proper electrical activity. Signals are received when neurotransmitters from adjacent neurons bind to receptors located on the dendrites' membrane, generating voltage changes in the neuron. The "tree-like" structure of the dendrites ensures that input signals from multiple neurons can be received. The cell soma then

integrates all incoming inputs. If these inputs reach a certain threshold, an action potential is generated and transmitted along the axon.

The axon is a cable-like projection that conducts the action potentials away from the cell soma. This conduction is facilitated by its sub-components: the nodes of Ranvier, the myelin sheath, and the axon terminal. Fundamentally, the propagation of action potentials along the axon is a chain reaction of ion movements in and out of the neuron's axonal membrane, driven by potential differences and ion channels. The nodes of Ranvier and myelin sheaths work together to accelerate information transmission through saltatory conduction. The nodes of Ranvier are unmyelinated gaps of axons rich with ion channels, allowing action potentials to "skip" from node to node, where they are "regenerated". Myelin sheaths are lipid (fat) layers that wrap around the axon for insulation, where the degree of myelination often relates to the axon's diameter and length [13], [14]. In some cases, axons may not have any myelin ("unmyelinated"). These myelin sheaths ensure that action potentials are generated only at these nodes. Upon reaching the axon terminal as part of a synapse, the action potential prompts the release of neurotransmitters, communicating the signal to a neighbouring neuron.

There are several types of neurons, most commonly differentiated based on their structure, function, and location. For instance, Purkinje neurons, with their broad, fan-like dendritic tree can handle massive synaptic input from cerebellar granule cells' parallel fibers [15]. Conversely, interneurons, with their short axons, primarily relay information within a specific area, not between distant brain regions. In some cases, the type of neuron present may correspond to a recognisable macroscopic structure (i.e. pyramidal neurons relating to the layers in the cerebral cortex).

2.1.2 Glia

Glia, or glial cells, are non-neuronal cells dispersed throughout the brain's WM and GM. How they are distributed depends on the type of glial cell, each of which

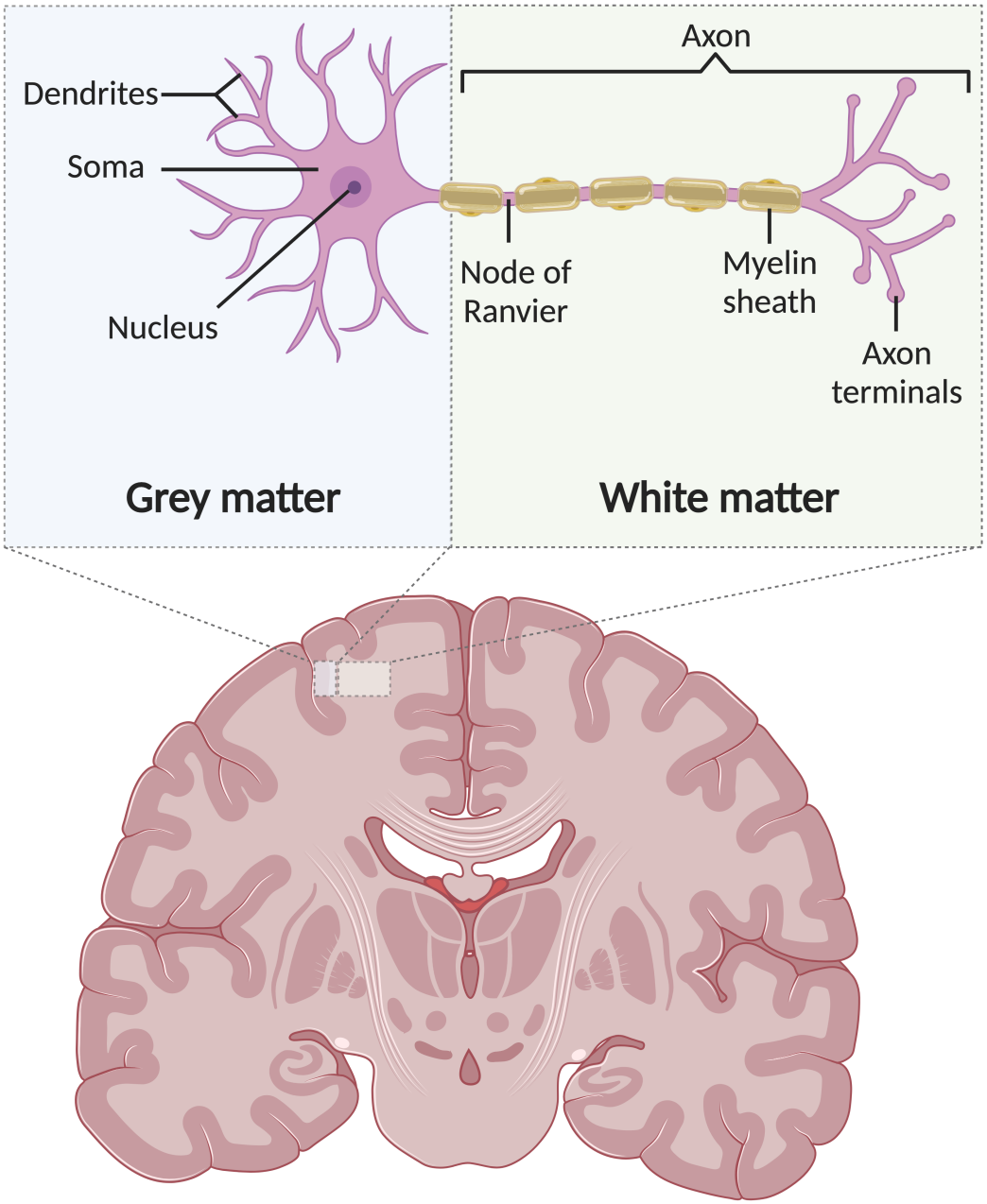

Figure 2.1: A schematic displaying the sub-components of a neuron, and where these components are generally located in the brain anatomy. The neuronal cell bodies inhabit the brain's GM, where they receive signals via their dendrites. These signals then travel down the axon as electrical impulses. An axon is typically part of a fibre bundle located in the brain's WM. Factors such as axon diameter and myelination determine the conduction velocity of these impulses. These impulses reach the axon terminals, where they are then transmitted to other neurons via neurotransmitters. This figure was created in BioRender.com.

has different specialised functions. In brief, we describe three main glial cells: oligodendrocytes, astrocytes, and microglia [16] (Figure 2.2).

Oligodendrocytes are myelinating cells that wrap their processes around axons to create myelin sheaths (Figure 2.2 right) [17]. Beyond myelination, oligodendrocytes help maintain axonal integrity and function by transferring essential nutrients and compounds to neurons.

Astrocytes interact with neurons, blood vessels, and other glial cells [16], [18]. They contribute to and maintain the blood-brain barrier—the barrier that restricts specific substances in the bloodstream from entering the brain. Astrocytes also support neuronal signalling by regulating the extra-cellular chemical environment, and by converting the neurotransmitter glutamate into glutamine for reuse (Figure 2.2 middle).

Microglia are the resident immune cells in the central nervous system [19]. In its ramified (i.e. branched out) state ("non-activated state"), microglial processes continually survey the brain environment. When a microglial cell detects abnormalities (e.g. pathogens) or damage due to injury, the cell "activates" by undergoing morphological change to possess an amoeboid shape ("activated state"). This change in shape results in a change in function. Activated microglia phagocytise—engulf and digest—cellular debris and pathogens (Figure 2.2 left). Finally, they produce and release pro-inflammatory and anti-inflammatory cytokines and chemokines necessitated for neuroinflammation and repair.

2.1.3 Anatomy

The high-level organisation of glia and neurons and the associated functional specialisation give rise to the macroscopic architecture, or anatomy, of the brain. The architecture of the brain can be distinguished as white WM and GM. The macroscopic differentiation between WM and GM is a manifestation of how neu-

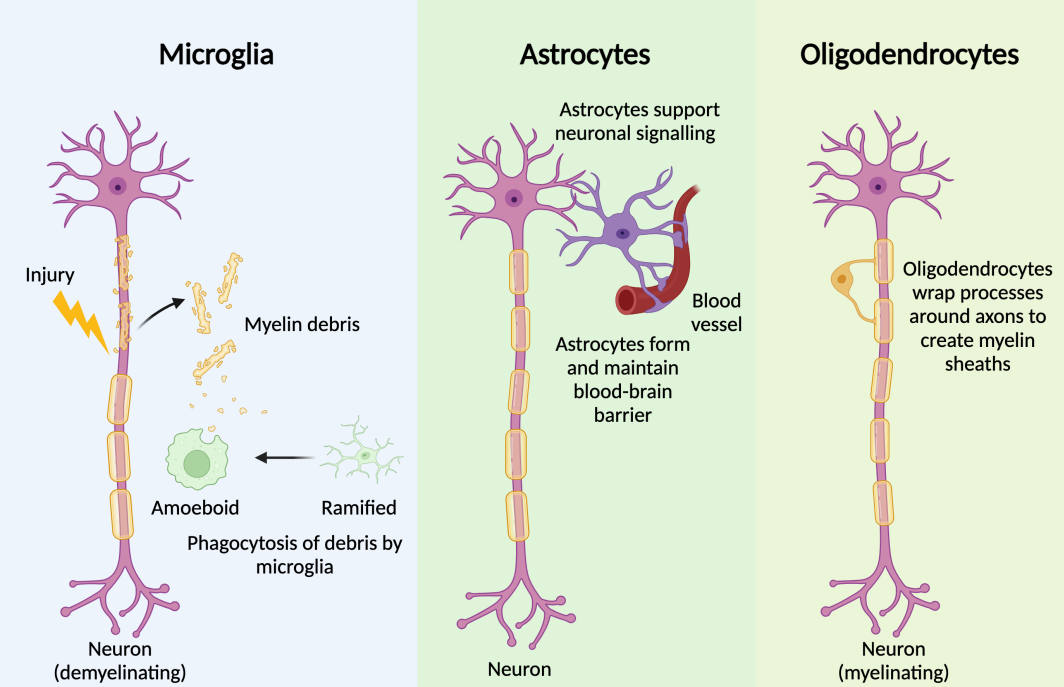

Figure 2.2: A schematic summarising the key roles of glial cells in the brain. This figure was created in BioRender.com.

rons, their extensions, and accompanying glia are spatially organised and distributed in the brain.

WM is most notably characterised by a predominance of myelinated axons that are produced and maintained by oligodendrocytes. The myelin sheaths are rich in lipids (i.e. fatty compounds), which give WM its characteristic pale appearance. These axons are organised into specialised tracts (e.g. projection, association, and commissural) (Figure 2.3) that are responsible for connecting brain regions. The commissural tracts describe any inter-hemispheric connection. An example of this tract is the corpus callosum, a dominant neural "highway" that connects many regions across the brain. The projection tracts link the cerebral cortex to the lower brain regions and the spinal cord. They relay sensory and motor information from other body parts to and from the brain. The corticospinal tract is an example pathway that transmits motor information from the cortex to the spinal cord. Finally, association tracts are tracts that connect regions within-hemisphere. An

example of this is the superior longitudinal fasciculus, which are long-range within-hemisphere connections that subserve high-level cognitive functions that require integrating input from many sources of information.

GM is largely composed of neuronal cell bodies, dendrites, and unmyelinated axons, though there are also myelinated axons and oligodendrocytes. The neurons are supported by astrocytes and microglia. Its grey appearance is derived from the lack of myelination in the region, and the high density of capillaries. While GM has a canonical set of cell types, these regions tend to be highly specialised in the computations that these circuits form, based on the information input from multiple sources. These specialised functions include muscle control, sensory perception, memory, emotions, and speech.

2.2 Histology

Histological neuropathology or histology combines the staining of specific tissue features with light microscopy to visualise cellular structures at high resolution. It has been utilised for many years to study microanatomy [3] and is widely regarded as the "gold standard" for many pathological diagnoses, particularly in parts of the body that, unlike the brain, can be readily sampled for biopsy. More recently, it has been used extensively to understand the biological basis of MRI signals and/or validate the sensitivity of MRI signals to various aspects of brain tissue microstructure [21]–[23]. This is due to several key benefits of histology: 1) Histological staining is a high-specificity technique with protocols developed over many years to study different tissue features and cell types. 2) Stained slides can be imaged using brightfield microscopes to visualise cellular structures at the micron or sub-micron resolution. 3) The development of high-throughput slide scanning microscopes enables the rapid imaging of larger field-of-views or brain regions, allowing us to cover more MRI voxels when relating histology sections to MRI images.

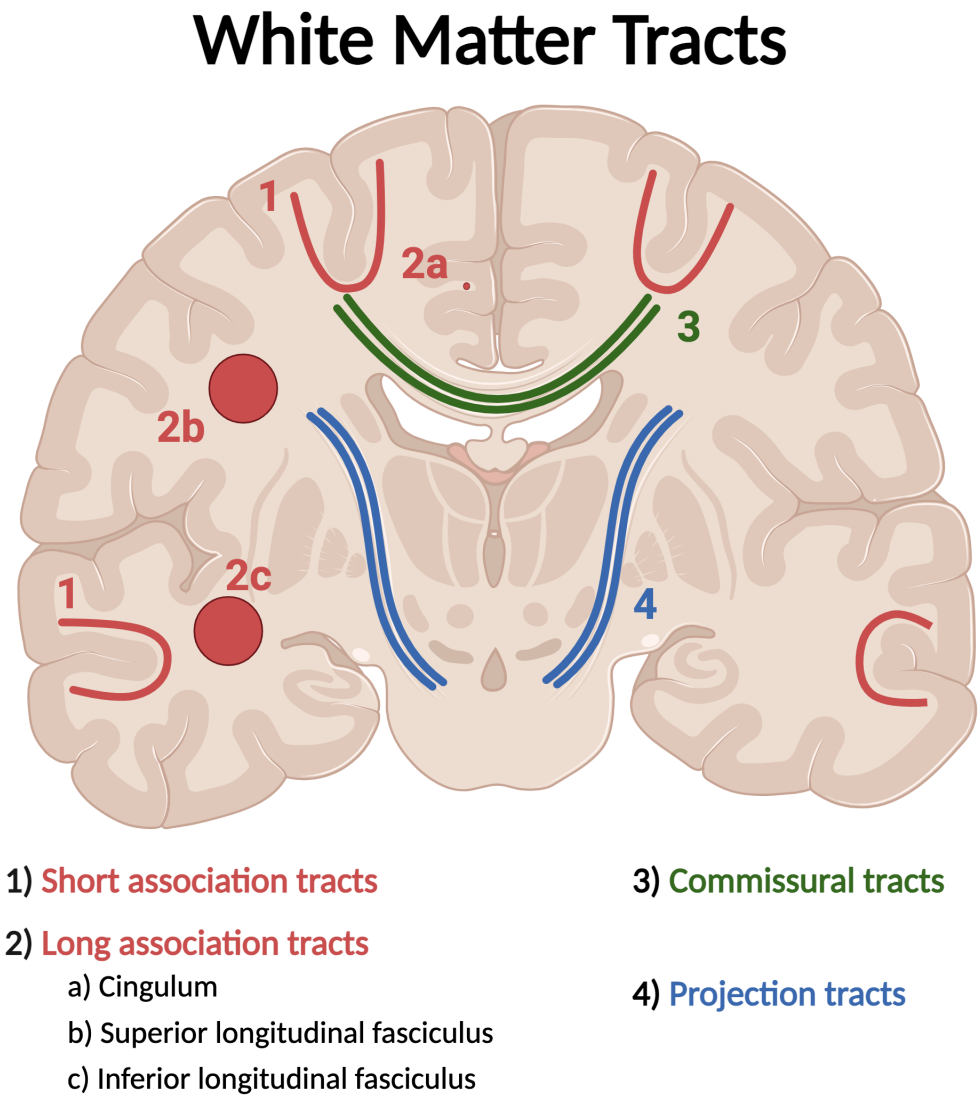

Figure 2.3: A sketch of different WM tracts. This figure was adapted and created in BioRender.com, with information from *A Functional Approach to Neuroanatomy*, edited by House and Pansky [20]

The section begins with an overview of the tissue preparation steps (Section 2.2.1). We then describe the immunohistochemistry (IHC) staining technique [6], used in Chapters 3 and 4. Lastly, we explore the categories of quantitative metrics that can be derived from histology (Section 2.2.3).

2.2.1 Tissue preparation

The tissue preparation stage ensures the longevity of the tissue's microstructure and prepares the tissue for sectioning and staining. In general, this is achieved through a series of key steps [6]:

- **Fixation**: After excision, postmortem tissue is fixed in formalin to prevent the autolysis and/or breakdown of cellular structures. The formalin forms covalent methylene bridges between protein molecules, termed "protein cross-linking". The protein cross-linking preserves the structural integrity of the cells. The time from the individual's death to brain fixation is termed the postmortem interval, while the duration of brain immersion in formalin is called the fixation time. As both variables may influence significantly tissue state, it is crucial to factor them as confounds in subsequent histological and/or MRI analyses.

- **Dehydration**: The next aim is to slice the fixed tissue without damaging it. To ensure that the tissue can hold up to the slicing process, it is best to embed the tissue in a stiff medium like paraffin wax. However, since water in tissue is not miscible with paraffin wax (i.e. liquids do not form a homogeneous mixture when added together), the tissue must be dehydrated. The tissue is dehydrated by undergoing a series of baths with increasing concentrations of alcohol.

- **Clearing**: While alcohol is required for dehydration, it also does not mix with paraffin wax. Hence, we remove it with the clearing step. Clearing is carried

out by dipping the dehydrated tissue samples in increasing concentrations of a clearing agent (e.g. xylene). The clearing agent is miscible with alcohol, thereby ensuring that the paraffin wax thoroughly infiltrates the tissue.

- **Embedding**: The tissue sample is then immersed in melted paraffin wax before being poured into a mold to cool. The mold ensures that the paraffin wax solidifies to form a stiff block that fully encases the tissue. This allows us to precisely cut thin sections from the tissue block without damaging it.

- **Sectioning**: The embedded tissue block is mounted onto a specialised precision instrument designed to cut thin (i.e. micrometre-scale) sections of the tissue. An example is the microtome, where a handwheel is rotated to move the mounted tissue block toward a blade for slicing. The thin tissue sections are then floated on a water bath to remove wrinkles before being mounted onto glass slides and stored.

- **Deparaffinisation and rehydration**: Before staining, we are required to return a tissue section to its original state so that the stain can penetrate it. This is achieved by deparaffinising and rehydrating the tissue section. Deparaffinisation removes the paraffin wax by immersing the tissue sections in a series of baths with a clearing agent that is miscible with paraffin wax. Rehydration, achieved by dipping the tissue sections in baths with decreasing concentrations of alcohol, ensures that the tissue section is finally ready for aqueous-based staining.

Once the tissue is prepared, the staining is carried out. Staining is the application of dyes or reactive chemicals to tissue sections to label and discern specific proteins or other structures. Different techniques, such as chemical staining or immunostaining, utilise different mechanisms to enhance or introduce contrast.

Chemical staining relies on the interaction between the applied chemical stain and the inherent properties of specific proteins, such as acidity. An example is the

Cresyl Violet method, which uses a basic dye to stain the acidic ribosomal RNA in Nissl bodies (rough endoplasmic reticulum) blue.

In immunostaining, antibodies are employed to target binding sites on a desired protein that we aim to visualise within tissue samples. The visualisation method may vary, encompassing techniques like immunofluorescence or immunohistochemistry. Below, we explain the chromogenic immunohistochemistry approach, which is used in Chapters 3 and 4 of this thesis.

2.2.2 Immunohistochemistry

The basic concept of chromogenic immunohistochemistry (IHC) is depicted in Figure 2.4. The first (primary) antibody binds with its target protein. This primary antibody is then targetted by another (secondary) antibody that carries a reporter enzyme. This enzyme provides a mechanism to locally catalyse a reaction with a chromogen that produces a coloured precipitate that specifically stains tissue in the region of the protein. The spatial pattern of this precipitate thus characterises the target protein's presence and spatial distribution in the tissue section. As we often want to know where the cell bodies are, a counterstain of a different colour is also used. Once the staining is done, the slide is digitised for data analysis.

A common chromogen is 3,3'-Diaminobenzidine (Figure 2.4, number two), or DAB, where the enzyme is horseradish peroxidase, and the resulting precipitate at the site of the target protein is brown. DAB is typically counterstained with hematoxylin, which stains cell nuclei blue, enhancing the contrast with the brown DAB precipitate for better visual interpretation of the target protein (i.e. in the context of the tissue section).

However, the presence of two stains makes the quantification of either stain density challenging. This is because stains themselves possess complex emitted spectral profiles (i.e. distribution of wavelengths) that do not align strictly with a single

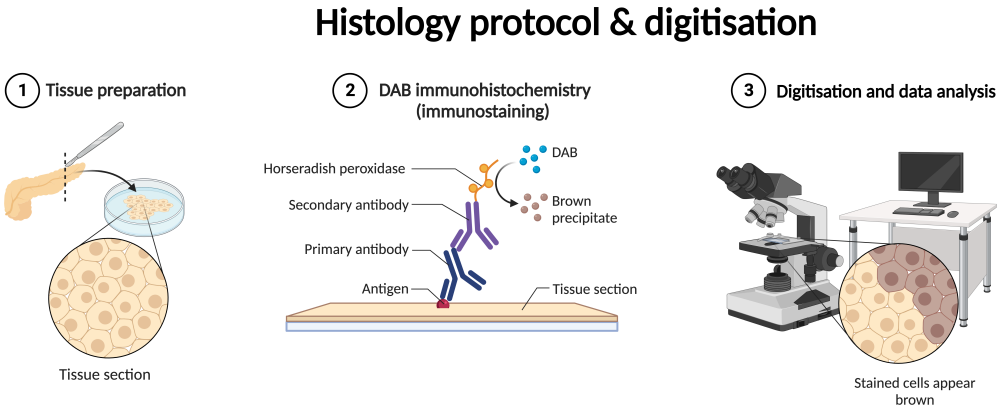

Figure 2.4: A broad sketch of a sample histology protocol that utilises immunostaining before the sections are digitised and analysed. The tissue preparation stages (c.f Section 2.2.1) include all the steps, from tissue fixation to sectioning. The sections are then immunostained (c.f. Section 2.2.2) by adding a series of antibodies and 3,3'-Diaminobenzidine (DAB) (i.e. the chromagen) to produce the characteristic brown precipitate at the location of the protein. Here, horseradish peroxidase is the enzyme. These stained sections are then digitised so that quantitative metrics can be extracted from them (c.f. Beer-Lambert's law and Section 2.2.3). This figure was created in BioRender.com.

colour channel [24]. One simple approach is to use the RGB channel most closely aligned to the stain-of-itself. For DAB, this is the red channel, though this yields intensity values that are not specific to DAB itself. To address this issue in quantification, Ruifrok and Johnston proposed colour deconvolution—a method that separates stains based on Beer-Lambert's law [25].

Beer-Lambert's law

In order to understand more sophisticated approaches to quantifying IHC stains, we need a simple mathematical framework for how the density of the stain leads to the attenuation of light. The Beer-Lambert's law relates the attenuation of light through a material ($\frac{I}{I_0}$), to the stain density (C) and attenuation coefficient (ϵ) of the medium:

$$\frac{I_\lambda}{I_{0,\lambda}} = 10^{-A_\lambda}. \tag{2.1}$$

Here, we assumed the maximum intensity of unattenuated light (I_0) to be 255. The absorbance A is defined as:

$$A_\lambda = \Sigma_{i=1}^{N} \epsilon_{i,\lambda} C_i. \tag{2.2}$$

N is the number of stains, $\epsilon_{i,\lambda}$ denotes the attenuation coefficient of i^{th} stain for light at wavelength λ, and C_i represents the stain density of i^{th} stain. For wavelengths typically corresponding to red, green, and blue colour channels of the digital sensor, the stain densities ($\mathbf{C}$) of DAB ("DAB"), hematoxylin ("hema"), and the leftover residual staining ("res") for a pixel with I_λ on the slide can be derived as:

$$\begin{bmatrix} C_{DAB} \\ C_{hema} \\ C_{res} \end{bmatrix} = \begin{bmatrix} \epsilon_{DAB,\ red} & \epsilon_{DAB,\ green} & \epsilon_{DAB,\ blue} \\ \epsilon_{hema,\ red} & \epsilon_{hema,\ green} & \epsilon_{hema,\ blue} \\ \epsilon_{res,\ red} & \epsilon_{res,\ green} & \epsilon_{res,\ blue} \end{bmatrix}^{-1} \begin{bmatrix} A_{red} \\ A_{green} \\ A_{blue} \end{bmatrix} = \mathbf{E}^{-1} \begin{bmatrix} A_{red} \\ A_{green} \\ A_{blue} \end{bmatrix}. \tag{2.3}$$

Estimation of the stain densities, $\mathbf{C}$, is a least-squares error minimisation problem. However, the rows of $\mathbf{E}$ (i.e. the stain-specific colour vectors) are not constrained to be orthogonal such that $C_{DAB/hema}$ can be negative, which is not physically valid. We address the inversion of this method with magnitude constraints on the staining densities in Chapter 3.

2.2.3 Metrics

When relating IHC to MRI, quantitative metrics need to be derived. Ideally, these metrics should adequately summarise microscopic properties at the MRI-scale resolution and account for significant variation in quantitative MRI parameters.

In this thesis, we consider two main categories of IHC metrics: density and dispersion metrics. We discuss these metrics because they relate to macroscopic tissue properties known to affect MRI parameters, such as the tissue's magnetic

properties (i.e. susceptibility) and structure. For instance, the density of specific microscopic proteins, such as proteolipid protein (PLP) in myelin [26] or iron-filled ferritin in oligodendrocytes [27] or both [28], may lead to differences in magnetic susceptibility, ultimately being reflected in MRI relaxometry and susceptibility measurements. The density and organisation of neuronal fibres, reflected in proteins for neurofilaments, similarly influence the tissue architecture probed with diffusion MRI [10]. In chromogenic IHC, these metrics are typically computed from the DAB stain channel, after using colour deconvolution.

Density

Metrics used to represent protein density are broadly categorised into either stain density or stain area fraction metrics [22]. One main approach is to use the stain density as a metric for protein amount. However, drawing conclusions based on these stain densities may be challenging, since they may not scale linearly with actual protein density for some stains [23], [29]. This is particularly the case for DAB. Unlike other materials that adhere to Beer-Lambert's law, DAB's brown reaction product scatters light instead of absorbing it [24], [30]. Hence, intensities from stain channels are best used as a proxy metric [21]. A workaround is to use the stain area fraction (SAF), which represents the proportion of specifically-stained pixels within a specified area. Typically, SAF is computed by manually setting a threshold in the stain channel to differentiate specific tissue structures from non-specific background staining. The pixels above the threshold are binarised, counted and normalised by a specified area to produce the SAF. Alternative methods utilise metrics derived from other channels, such as RGB and HSV [31], [32]. However, these are less tailored to the specific stain and, by extension, the protein-of-interest.

Dispersion

Orientation dispersion in histological tissue samples is typically quantified using structure tensor analysis [33]. In brief, the structure tensor approach computes local orientation information based on image gradients. By analysing variations in these local orientations across the sample, the primary structural orientation—a measure of how uniformly structures are oriented within a specific region—can be derived on a per-pixel basis. This is particularly interesting in WM to characterise axonal fibre populations, often using stains for myelin or neurofilaments. A distribution defined on a sphere (e.g. Bingham, Watson distribution) can then be fitted to the combined orientations within a voxel to calculate a voxelwise dispersion metric that is suitable for comparison with diffusion MRI.

2.3 Quantitative magnetic resonance imaging

Magnetic resonance imaging (MRI) was developed in the 1970s by Paul Lauterbur and Sir Peter Mansfield [7]. Since then, MRI has evolved into a cornerstone clinical tool, enabling the non-invasive visualisation of anatomical structures for diagnosing and monitoring diseases.

In this section, we will briefly cover how an ensemble of a tiny quantum mechanical property can be successfully harnessed to measure MRI signals that translate to images (Section 2.3.1). We then discuss why and how quantitative parameters are extracted from these MRI signals (i.e. qMRI), before overviewing two qMRI techniques: relaxometry (Section 2.3.2) and diffusion MRI (Section 2.3.3). It is worth noting that for the scope of this thesis, we focus on the analysis of pre-existing MRI data, and will not delve into the underlying theory of MRI data acquisition and image formation.

2.3.1 Spins to magnetisation

The magnetic resonance in MRI originates from a fundamental quantum mechanical property—the nuclear spin. Only nuclei with an odd number of protons and/or neutrons exhibit non-zero nuclear spin [34]. A nucleus with non-zero nuclear spin possesses a magnetic moment, which is a form of angular momentum. In this section, we focus on the hydrogen nucleus, or a proton, since it is the most common nucleus detected in MRI.

During polarisation, an ensemble of spins is placed in a static magnetic field $\mathbf{B_0}$. The spins have a preferred orientation, where their magnetic moments are aligned with the direction of $\mathbf{B_0}$. This alignment is the lowest energy configuration. As the spins are also perturbed by thermal energy, the magnetic moments generally point in random directions in space, with a slight tendency to point in the direction of $\mathbf{B_0}$ [35]. By taking a vector sum of the ensemble's magnetic moments, we have the macroscopic magnetisation $\mathbf{M}$ that is aligned with the $\mathbf{B_0}$ (i.e. in equilibrium) and precesses at the Larmor frequency ω_0 about $\mathbf{B_0}$, where:

$$\omega_0 = \gamma|\mathbf{B_0}|, \tag{2.4}$$

γ is the gyromagnetic ratio (42.58 MHz/T for a proton). Here, $\mathbf{B_0}$ provides the main axis of reference, called the longitudinal axis and typically denoted z, while the plane perpendicular to $\mathbf{B_0}$ is called the transverse plane and is denoted $x - y$.

In MRI, we aim to measure and characterise the interaction of $\mathbf{M}$ with different magnetic fields. This interaction can be described classically by the Bloch equation [36]:

$$\frac{d\mathbf{M}}{dt} = -\gamma\mathbf{M} \times \mathbf{B_0}. \tag{2.5}$$

$\frac{d\mathbf{M}}{dt}$ is the rate of change of $\mathbf{M}$ with respect to time t. If $\mathbf{M}$ is aligned with $\mathbf{B_0}$, then $\frac{d\mathbf{M}}{dt}$ is equal to zero, and we are unable to detect signal changes along the longitudinal axis. According to Faraday's law, only a change of the magnetic flux in the transverse plane (i.e. $\frac{d\mathbf{M}}{dt} \neq 0$) can induce a current in a receiver coil. Hence, a "stationary" $\mathbf{M}$ is not detectable [35]. To detect $\mathbf{M}$, we need to tilt $\mathbf{M}$ away from its alignment with $\mathbf{B_0}$. This is achieved through an excitation step.

During excitation, energy is added to $\mathbf{M}$ to momentarily perturb it from its equilibrium alignment with $\mathbf{B_0}$. This is done through resonance; a separate magnetic field $\mathbf{B_1}$ oscillating at the $\mathbf{M}$'s Larmor frequency (c.f. Equation 2.4) is used to impart energy. Clinical MRI scanners typically have $B_0 \sim [1, 7]T$, resulting in a ω_0 that lies within the radiofrequency spectrum (∼63 MHz to 300 MHz). Thus, a short, time-limited "radio-frequency (RF) excitation pulse" is used. Typically, a "90° pulse" is applied to tilt $\mathbf{M}$ towards the transverse plane (i.e $x-y$ plane). When $\mathbf{M}$ is in the transverse plane, the precession of $\mathbf{M}$ about $\mathbf{B_0}$—now reflected as a non-zero$\frac{d\mathbf{M}}{dt}$—induces a current in the transverse RF receiver coil due to Faraday's law. This current is measured as an MRI signal.

T_1, T_2, T_2^* relaxation

Immediately after the RF pulse is applied, the $\mathbf{M}$ begins to move back into alignment with $\mathbf{B_0}$ through a process known as relaxation. This is described as the exponential recovery of the longitudinal magnetisation, M_z, with characteristic time T_1. At the same time, magnetisation in the transverse plane (transverse magnetisation, M_{xy}) starts to lose phase coherence ("dephase") due to interactions with other local magnetic fields. Dephasing causes the MRI signal to decay in magnitude with a characteristic transverse relaxation time (T_2). Different tissue structures possess different relaxation rates. Thus, we can preferentially "weight" an MRI image to T_1 or T_2 to display a specific contrast. We first overview the mechanisms governing these relaxation times [37], before briefly describing how and why images are weighted.

Relaxation times are due to molecular motion. If a spin (i.e. in a molecule) moves around its lattice (i.e. surrounding environment) at its Larmor frequency, the spin experiences a magnetic field that oscillates at the same frequency. This leads to energy exchange between the spin and the surrounding lattice ("spin-lattice"). In reality, spins move randomly in an ensemble, but with some component of that motion at the Larmor frequency. We can characterise the range of frequencies in an ensemble of spins with a spectral density:

$$J(\omega) = \frac{2\tau_c}{1 + \omega^2\tau_c^2}, \tag{2.6}$$

where $J(\omega)$ is a measure of the amount of molecular motion at the frequency ω. The correlation time τ_c describes the spins' rate of tumbling in a lattice and is influenced by factors such as temperature, size of the molecules in motion, and lattice structure. As the ensemble of spins exchange energy with the lattice, the $\mathbf{M}$ starts to return to its equilibrium position in alignment with $\mathbf{B_0}$ (i.e. z axis). The recovery of this longitudinal magnetisation (M_z) is:

$$M_z = M_0(1 - e^{-\frac{t}{T_1}}), \tag{2.7}$$

where here we assume that the excitation step uses a 90° pulse. M_0 is the magnitude of the magnetisation at equilibrium. T_1 is the recovery time constant, where a short T_1 indicates the rapid recovery of M_z (i.e. $\mathbf{M}$ quickly returns to its equilibrium) due to high energy exchange between spins and lattice.

This energy exchange (and by extension, T_1) is dictated by the τ_c. For maximal energy exchange, there must be a maximum amount of molecular motion at the Larmor frequency ω_0 (i.e. max J(ω_0)), which is only achieved when $\tau_c = 1/\omega_0$. Short T_1 is found in tissue environments where spins are restricted (e.g. the myelin sheaths in WM), while longer T_1 is associated with environments where spins rapidly tumble around (e.g. cerebrospinal fluid, CSF) or tumble very slowly.

T_2 relaxation characterises how fast M_{xy} decays predominantly due to the loss of phase coherence, or when spins no longer precess at the same phase. In the context of molecular motion, T_2 relaxation is influenced by two mechanisms: 1) the random fluctuations in the spins' angular momentum brought about by oscillating magnetic fields, or 2) the precession of spins at different Larmor frequencies as they experience different magnetic field. We describe each briefly.

Following excitation (i.e. application of a 90° pulse), spins are now in the transverse plane. As previously described, these spins tumble around the lattice, experiencing oscillating magnetic fields. Since these oscillating magnetic fields have the same effect as pulses, they start to "tilt" spins out of the transverse plane and into the longitudinal axis, which we term random fluctuation in the spins' angular momentum. These "tilted" spins no longer contribute to the measurement of M_{xy}, which influences T_2 relaxation. In essence, this is exactly the same mechanism that causes T_1 relaxation, and is sometimes termed the "T_1 contribution to T_2".

The second mechanism is the loss of phase coherence due to spins in the same transverse plane experiencing different magnetic fields. This mechanism relates to the spectral density function at the zero frequency ($J(0)$), which describes the expected displacement spins travel in the lattice. As spins displace to other locations, they experience a different magnetic field. In the context of T_2, these variations in the magnetic field are produced by neighouring spins, since each spin is a magnetic dipole. These magnetic field variations cause spins to precess at a different Larmor frequency, resulting in the loss of phase coherence. This mechanism that causes T_2 relaxation is sometimes termed the "secular contribution to T_2".

Putting both mechanisms together, the decay of M_{xy} is characterised as:

$$M_{xy} = M_0 e^{-\frac{t}{T_2}}. \tag{2.8}$$

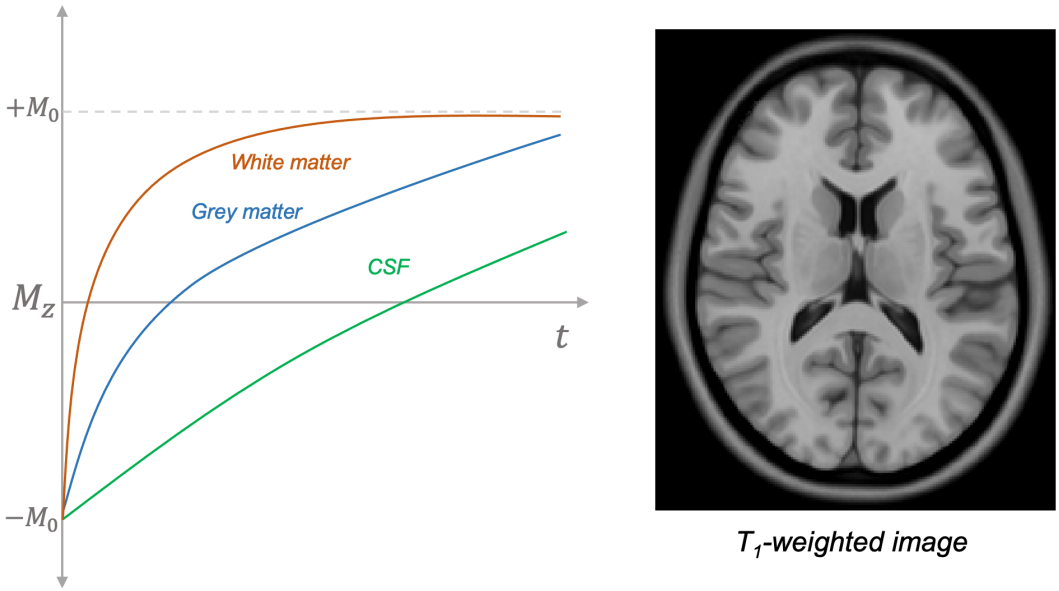

Figure 2.5: Following the inversion pulse, longitudinal magnetisation recovers at a relaxation time constant T_1. As WM (brown), GM (blue) and CSF (green) possess different T_1 values, this leads to clear tissue contrast (right) in the T_1-weighted image.

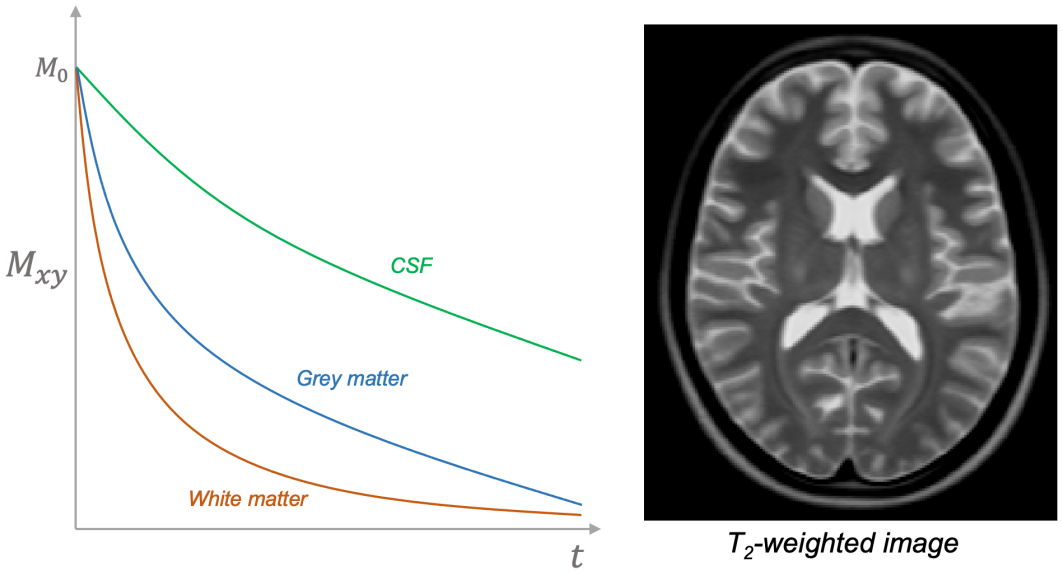

Figure 2.6: After the excitation pulse, the transverse magnetisation decays at a relaxation time constant T_2 due to loss of phase coherence. The tissue types have different T_2 values (left), thereby leading to distinct tissue contrast (right) in the T_2-weighted images.

Here, T_2 is the time constant characterising this signal decay. T_2 varies between tissue constituents and can lead to useful tissue-type contrast. Typically, tissue environments that allow the increased movement of spins or molecular rotation, such as CSF, have longer values, while structured tissue environments (e.g. myelin) exhibit shorter T_2.

The above describes $\mathbf{B_0}$ as being homogeneous over space. In practice, there are always variations in $\mathbf{B_0}$ due to imperfections in the MRI scanner and/or bulk magnetic susceptibility differences between different tissue compositions. In this case, the spins also experience different local magnetic fields due to these variations in $\mathbf{B_0}$ (termed "local field inhomogeneities") [38]. Here, we assume spins have their own local magnetic fields that remain the same throughout signal acquisition since they do not move far enough to experience another local field inhomogeneity. These local field inhomogeneities cause the spins in different locations to precess at marginally different frequencies, which in turn causes dephasing and signal decay. The signal decay time constant attributed to magnetic field inhomogeneities is T_2', where:

$$\frac{1}{T_2^*} = \frac{1}{T_2'} + \frac{1}{T_2}. \tag{2.9}$$

Here, T_2^* is the overall signal decay time constant that includes the decay due to magnetic field inhomogeneities (T_2'). T_2^* is related to M_{xy} using Equation 2.8, where T_2^* replaces T_2.

As T_1 and T_2 relaxation both relate to random molecular motion, they are intrinsic tissue properties and cannot be altered. However, T_2'-induced dephasing is reversible because spins are assumed not to have moved out of their own local magnetic fields. This reversal can be achieved by using a spin-echo MRI acquisition sequence, whereby an additional pulse is used to "refocus" the spins at $t = \tau$, after the initial RF excitation pulse. This pulse (termed the "180° refocussing pulse") "flips" the spins in the transverse plane, and inverts (i.e. negates) the phase accrued during the first τ

period (i.e. phase ϕ becomes $-\phi$). In the second τ period, spins will start to accrue the same amount of phase again (ϕ), resulting in a net zero phase difference (i.e. spins are in-phase) by $t = 2\tau$. The spins' rephasing leads to a signal measurement with increased magnitude. This is termed an "echo", where $t = 2\tau$ is the echo time (TE). Assuming a spin-echo sequence is used, the overall MRI signal S is:

$$S = M_0(1 - e^{-\frac{TR}{T_1}})e^{-\frac{TE}{T_2}}. \tag{2.10}$$

Here, TR is the repetition time, and it denotes the time in between RF excitation pulses. If an MRI sequence that does not reverse T_2'-induced dephasing (i.e. gradient-echo sequence) is used, T_2 is simply replaced with T_2^*. The spin-echo sequence is often used to acquire different types of MRI data, such as diffusion MRI data (PGSE sequence shown in Figure 2.8)

A particular contrast between tissue types can be generated by optimising the TE and TR to "weight" (i.e. sensitise) the signal to either M_0 (short TE and long TR), T_1 (short TE and TR) or T_2 (long TE and TR). Weighted images are used for visual assessment of pathology in clinical practice and for assessment of basic anatomy, such as the calculation of the volumes of specific structures. However, its inherently qualitative nature is prone to between-scanner and -session variations, making it challenging to reproduce. At the same time, we are unable to infer parameters that relate to specific tissue properties from weighted images. Quantitative MRI (qMRI) aims to derive absolute parameters that reflect tissue properties, facilitating comparisons across subjects, scanners, and time points. However, it is important to note that despite these efforts, there may still be notable non-biological variations within and between imaging sessions. By employing multiple sets of acquisition sequences (e.g. gradient-echo, spin-echo, inversion recovery) and parameters (e.g. TE, TR), one can acquire MRI data that maps a specific tissue property. This data is then pre-processed (e.g. motion and field map correction) before a signal model is

fitted to it to extract quantitative parameters. Here, we outline two qMRI techniques that we relate to microscopy in this thesis: relaxometry MRI and diffusion MRI.

2.3.2 Relaxometry MRI

Relaxometry MRI aims to quantify and map the relaxation rates—$R_1 = (1/T_1)$, $R_2 = (1/T_2)$, and $R_2^* = (1/T_2^*)$—of tissue. The acquisition sequence and signal model depend on the specific map.

For R_1-mapping, inversion-recovery (IR) sequences are typically used [39]. A standard IR sequence is a conventional spin-echo sequence preceded by a 180° pulse (termed the "180° inverting pulse"). The time interval between the 180° inverting pulse and the beginning of the spin-echo sequence is the inversion time (TI). This 180° inverting pulse flips $\mathbf{M}$ (labelled $+M_0$ in Figure 2.5) to point in the direction opposite to the direction of $\mathbf{B_0}$. During the inversion time, the inverted $\mathbf{M}$ (labelled $-M_0$ in Figure 2.5) undergoes T_1 relaxation to re-align with labelled $\mathbf{B_0}$. The spin-echo then begins at t=TI, where it functions to acquire the MRI signal along the transverse plane. Typically, multiple images are acquired by using different TI values and fixing both TE and TR. A signal model is then fitted to the acquired data to describe the recovery of the M_z to obtain T_1 maps, which we take the inverse of to get R_1 maps. The signal model for this standard IR sequence is identical to Equation 2.7, except with $2e^{-\frac{t}{T_1}}$ replacing $e^{-\frac{t}{T_1}}$.

R_2- and R_2^*-mapping data is acquired by varying TE and fixing TR. The presence (e.g. spin-echo [40]) or absence (e.g. gradient-echo [41]) of a refocussing pulse in the acquisition protocol determines if the data is R_2-weighted or R_2^*-weighted, respectively. In the standard gradient-echo sequence, a rephasing gradient is used to help rephase the spins. For both types of data, we fit the equation modelling M_{xy} (Equation 2.8) to compute either T_2 (R_2) or T_2^* (R_2^*) maps.

R_1, R_2, and R_2^* relate to tissue composition and/or structure. Specifically, they are predominantly influenced by myelin and iron content in the brain, as highlighted in numerous reviews [8], [22], [23], [42]. R_1 is sensitive to water, iron, and the macromolecules in myelin [43]–[45]. Thus, R_1 has been used to map cortical myelination [45]–[48], along with iron in cortical and subcortical regions [45]. R_2^* is sensitive to the magnetic susceptibility of tissue components and has been used to investigate paramagnetic iron [49] and diamagnetic myelin [50]. R_2 has also been associated with brain iron [49], [51], [52] and myelin [44], [53]–[55].

2.3.3 Diffusion MRI

Diffusion MRI (dMRI) maps the diffusion of water molecules through tissue, offering insights into its microstructural composition. We start this subsection by overviewing the principles of water diffusion, and why it can be used to probe structures at the micrometre-scale. This is followed by a discussion of how tissue microenvironments impact water diffusion and the measured dMRI signal. Finally, we discuss how we can leverage computational modelling of the dMRI signal to derive quantitative metrics that characterise microstructural tissue features. Most of the content we overview below is based on the book *Diffusion MRI: From Quantitative Measurement to In-vivo Neuroanatomy*, edited by Johansenberg and Behrens [56]

Diffusion in a homogeneous medium

Water molecules with thermal energy display Brownian motion (i.e. self-diffusion). The displacement of an ensemble of water molecules is described by a probability distribution. In the case where water freely diffuses in a homogeneous medium ("free water") without any barriers, the probability distribution $P(\mathbf{r}, \Delta)$ of a displacing water molecule is well described by a Gaussian:

$$P(\mathbf{r}, \Delta) \;=\; \frac{1}{\sqrt{2\pi\sigma^2}} \exp\left(-\frac{\mathbf{r}^2}{2\sigma^2}\right). \tag{2.11}$$

Here, $P(\mathbf{r}, \Delta)$ is termed the "diffusion propagator", $\mathbf{r}$ is the 3D displacement vector of the water molecule from the origin, and σ^2 is the variance of the diffusion propagator, which is equivalent to the mean squared displacement of water molecules. For N-dimensional space where N=3 [57], [58]:

$$\sigma^2 \;= < r^2 > = \; 2ND\Delta \;=\; 6D\Delta. \tag{2.12}$$

Δ is the duration in which the diffusion is observed (i.e. diffusion time). The main parameter-of-interest is the diffusion coefficient (or diffusivity) D, an intrinsic property that is influenced by the molecule size, the temperature, and the environment in which the molecule is diffusing in. For spheres diffusing in a homogeneous medium, D is defined with:

$$D \;=\; \frac{kT}{6\pi\eta R}, \tag{2.13}$$

where k is the Boltzmann constant, T is the temperature, η is the viscosity and R is the molecule's radius. With a D $\sim$ 3 $\mu m^2/ms$ at 37℃ (Equation 2.13) and a typical experimental diffusion time 50 ms, this results in a root mean squared displacement (Equation 2.12) or diffusion length of $\sim$30 μm. As both the diffusion length and the tissue microstructure are at the micrometre scale, this enables us to probe the tissue microstructure using dMRI.

Diffusion in the brain

In the brain, water molecules inhabit distinct microstructural compartments (i.e. inside axons, cell soma, or the extracellular space). As the water molecules diffuse,

they collide with cellular membranes that act to either slow diffusion (“hinder”) or trap water molecules (“restrict”) in a compartment, causing the measured average displacement of water molecules, and the apparent diffusion coefficient (ADC) (Figure 2.7B), to be lower than that of free water. The ADC describes the diffusion coefficient measured during a typical dMRI experiment. It may be influenced by the diffusion time Δ, and the extent to which the tissue microenvironment restricts or hinders the water molecules. Using Figure 2.7, we overview how free, hindered and restricted diffusion may lead to different root mean square (RMS) displacement (i.e. the square root of Equation 2.12) and apparent diffusivity values at different diffusion times.

Without any cellular membranes (Figure 2.7, top row, “Free diffusion”), the water molecules freely diffuse (“free water”), leading to a displacement plot that reflects random walk (Figure 2.7A, top row, displacement plot). This results in a RMS displacement that increases linearly with time and an apparent diffusivity that does not change with Δ (2.7B, top row). In the brain, diffusion in the CSF is characterised as being largely free diffusion.

In the presence of cellular membranes hindering water diffusion (Figure 2.7A, second row, "Hindered diffusion"), the molecules collide with the membranes. At very low Δ, the apparent diffusivity changes with time. However, as Δ increases, we measure a RMS displacement and ADC plot depicted in Figure 2.7B, second row. The slope representing RMS displacement over time and the ADC value remain constant, indicating Gaussian diffusion, though at a lower magnitude relative to free diffusion. If the diffusion of water is impeded differently in any direction, this leads to anisotropic diffusion. Given enough time, hindered water molecules can explore all available space not enclosed by the membranes. In the brain, hindered diffusion is typically used to describe the diffusion of water in the extra-axonal space, where the water molecules are impeded by the tortuous space between cells and diffuse through permeable cell membranes [56].

Finally, in the case where water is confined to a given compartment (Figure 2.7A, third row, "Restricted diffusion"), both the measured RMS displacement and ADC value will vary with the diffusion time. At very short Δ, the diffusion may appear Gaussian, since water molecules have not yet interacted with the cellular membrane. But as Δ increases, water molecules start to collide and interact with the impermeable membrane. This leads to a RMS displacement that changes over time, eventually reaching a maximum defined by the compartment size. Consequently, the ADC becomes time-dependent: measurements at different Δ lead to different ADC values, as seen in Figure 2.7B, third row. This time dependency is characteristic of non-Gaussian diffusion. In the brain, restricted diffusion is often used to describe the diffusion in myelinated axons. Due to the diffusion time scales commonly used in dMRI data acquisition, the myelin sheath is assumed to be impermeable. Hence, water molecules are confined within the axon.

This thesis considers dMRI data acquired in the long-Δ regime, where we have negligible sensitivity to smaller-scale tissue features with dimensions much smaller than diffusion length $L \sim \sqrt{6D\Delta}$ and each compartment is assumed to be a homogenised medium described by Gaussian, time-independent diffusion [59]. This allows us to model the tissue as a highly simplified substrate. For example, instead of axons being the complex structures we visualise within electron microscopy (e.g. with tortuous trajectories through space), diffusion within axons ("intra-axonal compartment") can now be well described by a stick with diffusion along the primary axon orientation (axial diffusivity) $D_a < D_{free}$, and negligible diffusivity across the axon. Outside the axons, the extra-axonal space is considered hindered diffusion and often modelled as a tensor. In this regime, the dMRI signal is sensitive to tissue parameters such as the volume fractions of each compartment, their diffusivities, the fibre orientation, and dispersion. It has limited sensitivity to features smaller than the diffusion length scale. Instead, these features are encoded in the diffusivities (e.g. increasingly tortuous axon trajectories may lead to lower axial diffusivities [59]).

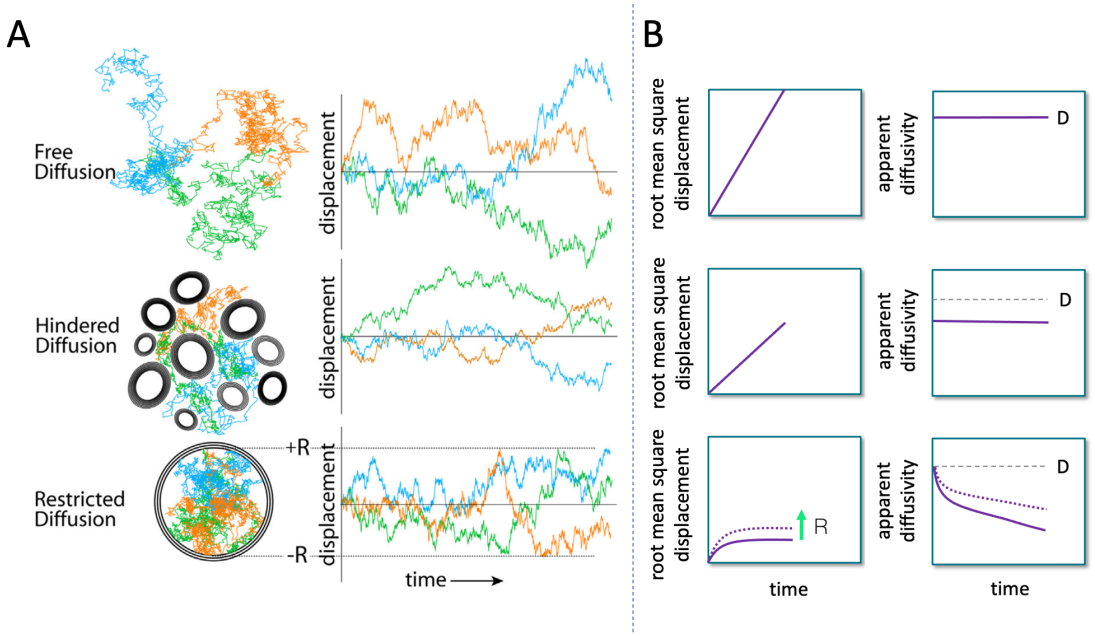

Figure 2.7: A schematic illustrating free, hindered, and restricted diffusion effects on root mean square (RMS) displacement and apparent diffusivity. (A) Water diffusion with and without membranes. Without membranes (top row), free diffusion reflects random walk. Hindered diffusion (middle row) shows a similar plot but with reduced maximum displacement. Within an impermeable cell membrane (bottom row), water diffusion is restricted within the compartment's radius. Reprinted from *Diffusion MRI: From Quantitative Measurement to In-vivo Neuroanatomy*, edited by Johansenberg and Behrens. (B) RMS displacement and average diffusivity plots. For free (top row) and hindered (middle row) diffusion, RMS displacement increases linearly over time, resulting in constant apparent diffusivities. Hindered diffusion has a reduced time-displacement slope and diffusivity (purple dotted line), relative to free diffusion (grey dashed line). Restricted diffusion plots vary based on diffusion time and compartment size (denoted by "R"). Printed with permission from Amy Howard.

Quantifying diffusion

To sensitise the MRI signal to the diffusion of water, a pulsed gradient spin-echo sequence (Figure 2.8) is traditionally used to encode spin displacement through a pair of RF pulses and a pair of identical diffusion-sensitising gradients. At $t = 0$, a 90° pulse (RF excitation pulse) is used to tilt the magnetisation $\mathbf{M_0}$ into the transverse plane. Next, a diffusion-sensitising gradient ($\mathbf{G}_+$) is applied to impart a phase modulation (θ_+) across the spins. The magnitude of the phase gain by each spin depends on the spin's spatial location along $\mathbf{G}_+$. This is followed by a 180° pulse (refocussing pulse), which is used to "flip" the spins when $t = \mathrm{TE}/2$

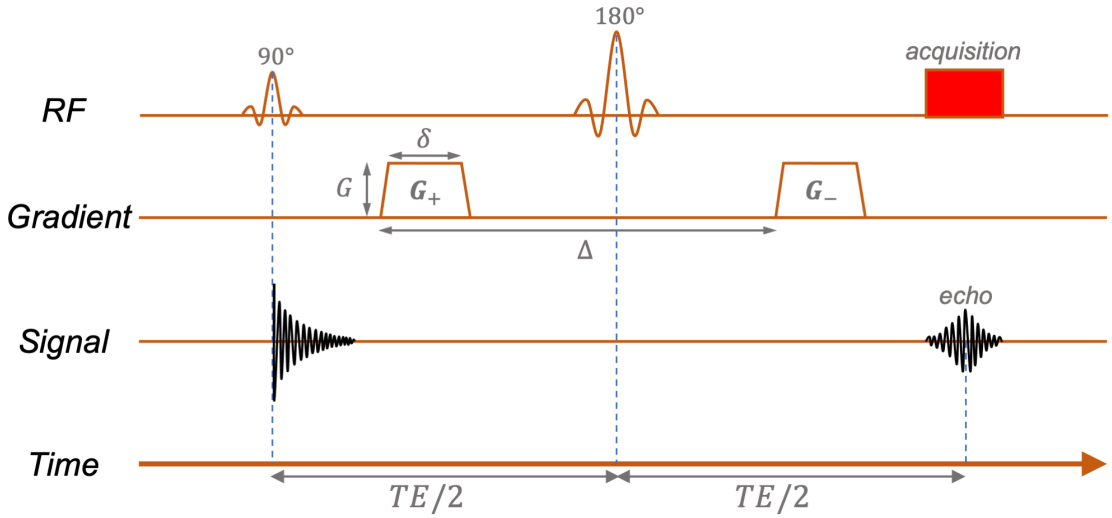

Figure 2.8: Schematic illustration of the pulsed gradient spin echo sequence. The diffusion-sensitising gradients ($\mathbf{G}_+$ and $\mathbf{G}_-$) have an amplitude G and duration δ. The time between the gradients (also termed "diffusion time") is Δ, while TE is the echo time.

(c.f. Section 2.3.1). A second diffusion-sensitising gradient ($\mathbf{G}_-$) is then applied, delivering an equal but opposite phase modulation (θ_-) to the spins. At $t = \text{TE}$, the dMRI signal is acquired, where each spin's net phase is $\Delta\theta = \theta_+ + \theta_-$.

The time interval separating both gradients is the diffusion time (Δ). If the spins do not move along the direction of the applied gradients ($\mathbf{g}$) during the diffusion time, the phase modulation from both gradients will perfectly cancel out, and each spin experiences no net phase difference ($\Delta\theta = 0$). Conversely, if the spins displace in the direction of these gradients, these spins are in different spatial positions for $\mathbf{G}_+$ and $\mathbf{G}_-$, and each spin accumulates unequal phase from each gradient ($\Delta\theta \neq 0$). Each spin's net phase is proportional to the spin's displacement in the direction of the gradients. A non-zero net phase contributes to phase incoherence across the voxel, which leads to signal loss or attenuation of the dMRI signal.

To quantify diffusion from the dMRI signal, a signal equation is fitted to the data. For a given gradient orientation, the dMRI signal can be described as:

$$S = M_0(1 - e^{\frac{TR}{T_1}})e^{\frac{TE}{T_2}}e^{-b(ADC)}, \tag{2.14}$$

where we assume the spins' phase distribution to be Gaussian. To isolate the effect of diffusion (i.e. ADC) from T_1 and T_2 relaxation, the signal is normalised by the non-diffusion weighed signal, $S_0(M_0, T_1, T_2)$ such that:

$$\frac{S}{S_0} = e^{-b(ADC)}. \tag{2.15}$$

The b-value captures the diffusion-weighting of the sequence i.e. how much contrast (signal loss) will occur for some given ADC. If rectangular gradients are used, the b-value is defined as:

$$b = \gamma^2 G^2 \delta^2 (\Delta - \frac{\delta}{3}), \tag{2.16}$$

where G is the gradient amplitude, δ is the gradient duration and Δ is the diffusion time. These are all scanner parameters, which we can tune to probe different properties of water diffusion in tissue. For instance, if we fixed the b-value and measured the ADC for different Δ, we would be able to characterise the time-dependence of the ADC. Alternatively, we can fix Δ and estimate the ADC across multiple gradient directions to map the diffusion propagator in 3D. Both approaches can be repeated for different b-values (e.g. by changing the gradient magnitude G), where different b-values provide sensitivity to different microstructural features. In Chapter 5 of this thesis, we analysed High Angular Resolution Diffusion Imaging (HARDI) data, where Δ was fixed to probe the long-Δ regime (where we assume time-independent diffusion) and a large number of gradient directions were acquired for multiple b-values.

Diffusion tensor imaging

With the dMRI data acquired, computational models are required to characterise features of the diffusion propagator or to relate the observed dMRI signal to features

of the tissue microstructure. An example of a phenomenological model is diffusion tensor imaging (DTI). DTI, as introduced by Basser et al. [60] is used to characterise the directionality and magnitude of water diffusion in a 3D MRI voxel. We can model water diffusion with an anisotropic rank-2 tensor $\mathbf{D}$:

$$A = e^{-b\mathbf{g}^T\mathbf{D}\mathbf{g}}, \tag{2.17}$$

where $A = \frac{S}{S_0}$ is the signal attenuation due to diffusion, and $\mathbf{g}$ is the gradient direction. $\mathbf{D}$ is symmetric about the diagonal and defined by six unknown diffusivity values. The model assumes Gaussian diffusion and is therefore suitable for single shell data with b$\sim$1 $ms/\mu m^2$.

Using eigenvalue decomposition, $\mathbf{D} = \mathbf{K}^T\mathbf{\Lambda}\mathbf{K}$, $\mathbf{D}$ can be described by three eigenvectors and three eigenvalues:

$$\mathbf{K} = \begin{bmatrix} \kappa_{1,x} & \kappa_{2,x} & \kappa_{3,x} \\ \kappa_{1,y} & \kappa_{2,y} & \kappa_{3,y} \\ \kappa_{1,z} & \kappa_{2,z} & \kappa_{3,z} \end{bmatrix}, \quad \mathbf{\Lambda} = \begin{bmatrix} \lambda_1 & 0 & 0 \\ 0 & \lambda_2 & 0 \\ 0 & 0 & \lambda_3 \end{bmatrix}, \tag{2.18}$$

where the eigenvalues $\lambda_1 > \lambda_2 > \lambda_3$ represent the diffusivity of water in the three principle directions ($\boldsymbol{\kappa_{1,2,3}}$). λ_1 is the axial diffusivity (AD), which is the diffusivity along the principal direction of the tensor. λ_2 and λ_3 are the diffusivities perpendicular to the principal direction of the tensor. The radial diffusivity (RD) is the mean of λ_2 and λ_3. These eigenvalues can be also used to compute other metrics, such as the mean diffusivity:

$$\hat{\lambda} = \ MD \ = \frac{\lambda_1 + \lambda_2 + \lambda_3}{3}, \tag{2.19}$$

and fractional anisotropy (FA):

$$FA = \sqrt{\frac{3}{2}} \frac{\sqrt{(\lambda_1 - \hat{\lambda})^2 + (\lambda_2 - \hat{\lambda})^2 + (\lambda_3 - \hat{\lambda})^2}}{\sqrt{\lambda_1^2 + \lambda_2^2 + \lambda_3^2}}. \tag{2.20}$$

FA is on a 0-1 scale, with higher FA representing greater tissue anisotropy.

DTI metrics provide sensitivity to tissue changes at the microstructural level. For example, high FA likely represents highly aligned fibre populations whilst reduced FA has been linked to processes that disrupt the architecture of fibre tracts, such as axonal degeneration [10]. Similarly, MD has been associated with cellular structure integrity; reduced MD may suggest hindrance in water diffusion from increased cell proliferation, while increased MD may indicate tissue damage due to edema [61].

DTI has several key limitations. First, as DTI only uses one tensor (i.e. one compartment with Gaussian diffusion) to model tissue, it is unable to accurately resolve crossing fibres. Multi-tensor approaches are used to address this issue [62]. Further, we can consider WM tissue as being comprised of multiple compartments with different diffusion characteristics. Modelling all of these compartments as a single tensor may be considered oversimplistic. One approach to address this limitation is the use of biophysical diffusion models. These models aim to extract more biologically-meaningful tissue parameters by modelling the effects of individual microstructural compartments on the dMRI signal.

Biophysical diffusion models

Biophysical diffusion models are forward models that aim to describe the dMRI signal as a sum of multiple compartments (e.g. intra-axonal, extra-axonal, cell bodies), each parameterised by biologically interpretable parameters ("biophysical parameters") such as axon orientation, volume fraction or diameter. Biophysical parameters are typically quantified by fitting the biophysical model to the dMRI signal.

The standard model In the relatively low b-value, long-Δ regime (e.g. that which is usually achieved on clinical scanners), the brain WM is typically described using the "standard model" [63]. In this regime, ADC is assumed to have negligible time-dependence (c.f. Section 2.3.3), and the dMRI signal is considered to be the sum of non-exchanging Gaussian compartments. The standard model describes an intra-axonal (denoted with the subscript "in") and an extra-axonal ("ex") compartment's contribution to the normalised dMRI signal. An isotropic compartment ("iso") may also be added to account for partial volume contamination due to CSF [64]:

$$\frac{S}{S_0} = f_{in}A_{in} + f_{ex}A_{ex} + f_{iso}A_{iso}. \tag{2.21}$$

$A_{in/ex/iso}$ denotes the signal attenuation associated with the intra-axonal/extra-axonal/isotropic compartments, while $f_{in/ex/iso}$ are their respective signal fractions. The signal fractions are assumed to sum to 1.

If we first consider the diffusion signal for a single fibre within the voxel (the response function, R), the intra-axonal compartment is modelled as "stick-like" with almost free diffusion along the axon, and negligible diffusion perpendicular to the axon:

$$R_{in} = e^{-bD_{\parallel,in}(\mathbf{g}\cdot\boldsymbol{\mu})^2}. \tag{2.22}$$

$D_{\parallel,in}$ is the intra-axonal axial diffusivity, i.e. the diffusivity of intra-axonal water along the orientation of the fibre, $\boldsymbol{\mu}$. $\mathbf{g}$ is the gradient direction.

The extra-axonal compartment refers to the space surrounding the axons. As the presence of axons hinders (and does not restrict) the movement of water molecules in this space, we model the diffusion within this compartment using an axially symmetric tensor, defined as:

$$R_{ex} = e^{-bD_{\parallel,ex}(\mathbf{g}\cdot\boldsymbol{\mu})^2}e^{-bD_{\perp,ex}(1-(\mathbf{g}\cdot\boldsymbol{\mu})^2)}, \tag{2.23}$$

where $D_{\parallel,ex}$ and $D_{\perp,ex}$ are the extra-axonal axial and radial diffusivity respectively.

Finally, the CSF is described by an isotropic compartment where:

$$R_{iso} = e^{-bD_{iso}}. \tag{2.24}$$

To account for the dispersion of a neuronal fibre bundle within the voxel, we spherically convolve the response functions with a neuronal fibre orientation distribution function (H):

$$A = \iint_{S^2} H(\mathbf{n}) R(\mathbf{g} - \mathbf{n})\, d\mathbf{n}, \tag{2.25}$$

where $H(\mathbf{n})d(\mathbf{n})$ gives the probability of finding a fibre along an orientation $\mathbf{n}$ sampled from a sphere S. A is the attenuation of the dMRI signal measured along gradient direction $\mathbf{g}$. Note that the convolution of the isotropic compartment has no effect ($A_{iso} = R_{iso}$) since R_{iso} is independent of gradient direction. A commonly used fibre orientation distribution function is the Watson distribution [64]:

$$H = \frac{1}{c} e^{\kappa(\boldsymbol{\mu}\cdot\mathbf{n})^2}, \tag{2.26}$$

where c is the normalisation constant and κ is the concentration coefficient. As κ is unbounded, this can lead to a problematic interpretation of dispersion. This is addressed by a change of variable from κ to the orientation dispersion index, ODI, where:

$$ODI = \frac{2}{\pi} \arctan\left(\frac{1}{\kappa}\right), \tag{2.27}$$

ODI ranges from 0 to 1, where lower ODI indicates less dispersion.

Model degeneracy Putting this together, the full model (Equation 2.21) has up to nine free biophysical parameters:f_{in}, $D_{\parallel,in}$, $D_{\parallel,ex}$, $D_{\perp,ex}$, f_{iso}, D_{iso}, $\mu(\theta,\phi)$,κ (or ODI). However, typically acquired dMRI data is fairly non-descriptive. When fitting our model to this data, we often have a flat parameter-fitting landscape [59], [65]. Hence, the inferred biophysical parameters are often degenerate, with multiple parameter sets fitting the signal equally well.

This issue of degeneracy is well-known, with multiple solutions proposed and/or used. One approach is to acquire more comprehensive data with an acquisition specifically designed to provide orthogonal information that stabilises the fitting. For example, using multiple diffusion encodings (a combination of linear, planar, and/or spherical) has been shown to robustly estimate additional parameters-of-interest [66]–[68].

For dMRI data that have been acquired using a more "typical" linear diffusion encoding protocol (e.g. HARDI), only relatively few (<5) biophysical parameters can be reliably fitted [69]. As such, a common approach is to make simplifying assumptions about the tissue microstructure in order to fit a restricted biophysical model to dMRI data reliably. Neurite orientation dispersion and density imaging (NODDI) is a constrained form of the standard model where ($D_{\parallel,in} = D_{\parallel,ex} = D_{\parallel}$, $D_{\perp,ex} = D_{\parallel}(1-f_{in})$) and fixing the diffusivities to in-vivo values ($D_{\parallel} = 1.7\ \mu m^2/ms$, $D_{iso} = 3.0\ \mu m^2/ms$). By adopting these assumptions, NODDI only requires the estimation of five free parameters (instead of the original nine), facilitating more robust parameter estimation. If these assumptions are inaccurate or a bad representation of the tissue, the resulting parameter estimates may be biased [69]–[72]. This is particularly challenging in postmortem studies. In Chapter 5, we introduce an alternative method that circumvents this solution degeneracy without resorting to simplifying assumptions in the model.

Extensions to the standard model When parameter degeneracy is not a concern, the standard model can be extended to account for additional aspects of the tissue microstructure. For example, the signal contribution for cell bodies or

soma can be accounted for by adding an intra-soma ("is") compartment ($f_{is}A_{is}$) to Equation 2.21, where f_{is} is the intra-soma signal fraction and A_{is} the attenuation [73], [74]. If we model cell bodies as impermeable spheres, A_{is} can be computed using the Gaussian phase distribution approximation [75]–[77], where:

$$A_{is} \approx \exp\left\{-\frac{2(\gamma g)^2}{D_{is}} \sum_{m=1}^{\infty} \frac{\alpha_m^{-4}}{\alpha_m^2 R_s^2 - 2} \times \left[2\delta - \frac{2 + e^{-\alpha_m^2 D_{is}(\Delta-\delta)} - 2e^{-\alpha_m^2 D_{is}\delta} - 2e^{-\alpha_m^2 D_{is}\Delta} + e^{-\alpha_m^2 D_{is}(\Delta+\delta)}}{\alpha_m^2 D_{is}}\right]\right\}. \tag{2.28}$$

D_{is} is the bulk diffusivity of water in the cell soma, and R_s is radius of the cell soma. R_s can either be described as a distribution or a single value. α_m is the m^{th} root of the equation $(\alpha R_s)^{-1} J_{3/2}(\alpha R_s)$, with $J_n(x)$ being the Bessel function of the first kind.

Alternatively, the standard model can be extended to include a dot ("d") compartment to represent stationary water (e.g. water trapped in very small isotropic spaces to the point where they appear stationary or with negligible diffusion) by adding a signal constant (A_d) to Equation 2.21.

The dot compartment's microstructural origin is still contentious. In in-vivo studies, no significant dot compartment in WM has been observed [78], [79]. However, previous studies have suggested that the addition of a dot compartment may better explain ex-vivo dMRI data [80], [81]. In ex-vivo dMRI data, it has been found to be associated with tissue fixation [76], [80], [81] and scanning temperature [82]. It has been hypothesised to represent water trapped in glial cell bodies [76], changes in the chemical environment during fixation [80], and more recently, vacuoles in the myelin sheath [82].

3

An automated pipeline for extracting quantitative stain area fraction from histology

Contents

Foreword

The acquisition of MRI and microscopy in the same post-mortem tissue sample enables direct correlation between MRI and microscopy-derived parameters. How-

ever, there still lacks a standardised automated pipeline to process histology data, with most studies relying on manual intervention. Here, we introduce an automated pipeline to extract a quantitative microscopy metric for staining density (stain area fraction, SAF) from multiple immunohistochemical (IHC) stains. The pipeline was designed to directly address IHC artefacts related to tissue staining and slide digitisation. The pipeline is comprised of four key steps: 1) slide-specific colour information was derived using a clustering approach to improve the accuracy of stain separation, 2) stain separation was performed using a computationally efficient method that produces physically meaningful staining densities, 3) segmentation thresholds were derived using an automated, data-driven method, and 4) SAF maps were computed at the whole-slide level. We demonstrated how each step of the pipeline improves the analysis process compared to traditional manual approaches. Lastly, we evaluated the reliability of the pipeline by applying it to an IHC dataset designed to test reproducibility.

Publications relating to this work

Journal articles:

Kor DZL, Jbabdi S, Huszar IN, Mollink J, Tendler BC, Foxley S, Wang C, Connor S, Smart A, Ansorge O, Pallebage-Gamarallage M, Miller KL*, Howard AFD* "An automated pipeline for extracting histological stain area fraction for voxelwise quantitative MRI-histology comparisons", NeuroImage. 2022;264:119726. doi:10.1016/j.neuroimage.2022.119726

Conference proceedings:

Kor DZL, Mollink J, Huszar IN, Howard AFD, Foxley S, Pallebage-Gamarallage M, Smart A, Ansorge O, Jbabdi S, Miller KL "Development of an automated processing pipeline for brain MRI-histology correlations", Proceedings of the Annual Meeting of the OHBM, online, 2020.

Kor DZL, Jbabdi S, Mollink J, Huszar IN, Pallebage-Gamarallage M, Smart A, Connor S, Ansorge O, Howard AFD*, Miller KL* "An automated pipeline for extracting semi-quantitative estimates from immunohistochemistry images", Proceedings of the Post Graduate Virtual Meeting of the British, Irish, Iberian Chapter of the ISMRM, online, 2021.

Kor DZL, Jbabdi S, Huszar IN, Mollink J, Connor S, Smart A, Ansorge O, Pallebage-Gamarallage M, Miller KL*, Howard AFD* "Automatic extraction of reproducible semi-quantitative histological metrics for MRI-histology correlations", Proceedings of the 29th Annual Meeting of the ISMRM, online, 2021.

Howard AFD, Huszar IN, Zhu S, **Kor DZL**, Roumazeilles L, Jbabdi S*, Miller KL* "Towards whole-brain, quantitative characterisation of microscopy-derived microstructure in the BigMac dataset" Proceedings of the 31st Annual Meeting of the ISMRM, Toronto, 2023.

Tisca C, Tachrount M, Smart A, Lange F, Howard AFD, Wang C, Qiu L, Tendler BC, Bratley C, **Kor DZL**, Huszar IN, Ballarobre-Barreiro J, Fava M, Mayr M, Lerch J, Martins-Bach A, Miller KL "Linking MRI to histology in the mouse brain: A framework for data acquisition and pre-processing" Proceedings of the Annual Meeting of the OHBM, Montreal, 2023.

Howard AFD, Huszar IN, Zhu S, **Kor DZL**, Roumazeilles L, Jbabdi S*, Miller KL* "Whole-brain characterisation of microscopy-derived microstructure in the BigMac dataset" Proceedings of the Annual Meeting of the OHBM, Montreal, 2023.

3.1 Introduction

Magnetic resonance imaging (MRI) is a powerful tool that can be used to evaluate neurodegenerative disorders in-vivo. MRI techniques have produced quantitative parameters sensitive to macroscopic neuropathological changes [83]–[85]. However, MRI parameters are non-specific and sensitive to multiple factors related to tissue microstructure. Coupled with millimetre resolution, this leads to difficulty in determining the microstructural underpinnings of a given MRI change (e.g. in disease).

Immunohistochemistry (IHC) is a microscopy staining technique that can be used to address this difficulty. IHC uses primary antibodies to stain target antigens (proteins related to microstructural features-of-interest) with high specificity. Antigens are then commonly visualised using the chromogen 33-diaminobenzidine (DAB) to stain the marked proteins brown. To add contextual information and localise stained tissue features, haematoxylin is often used as a counterstain to mark cell nuclei purple. The acquisition of IHC can aid neuropathological diagnosis [18], [86]–[93], with antibodies targeting either common tissue features (e.g. myelin or neurofilaments) or markers specific to pathology (e.g. activated microglia, a marker of inflammation [94], [95], or aggregated pTDP-43 in ALS [96]. Further, the acquisition of IHC and MRI in the same post-mortem tissue sample enables a direct correlation of MRI- and microscopy-derived metrics. This methodology is used to validate MRI parameters and improve our microstructural interpretation of MRI. Here, postmortem MRI functions as a crucial intermediary between IHC and in-vivo imaging. Postmortem MRI shares a common tissue state with IHC, while possessing the same signal-forming mechanisms as in-vivo MRI [97].

While many studies relate IHC to MRI parameters [22], [32], [98]–[104], there is still a lack of automated pipelines for extracting quantitative metrics from IHC slides of neuronal tissue [22]. Most MRI-IHC analyses rely on heavy manual intervention [23], [42], [105], [106], with some using subjective metrics, such as staining intensity scores resembling low, moderate or strong [106], [107]. Others directly use the DAB

channel's stain density to approximate the amount of targeted protein within the tissue [29], [106], [108], [109]. However, this interpretation is limited as the densities do not scale linearly with protein density [23], [24], [29].

To circumvent this, other pipelines extract the stain area fraction (SAF) i.e. the number of DAB-stained pixels within a given area. In most pipelines, SAF is quantified by manually setting a threshold for the DAB channel to segment microstructural tissue compartments from non-specific background staining in regions-of-interest (ROIs) [22], [23], [42], [105].

The manual derivation of SAF has two main issues. First, the manually-set threshold is dependent on the operator's expertise and a single threshold is often applied to all slides in a dataset or a batch of slides which have been processed together [96]. Although this is time efficient and avoids intra-observer variability, it comes at the expense of optimising thresholds for individual slides, resulting in decreased robustness to microscopy artefacts, such as slide-to-slide and within-slide staining intensity variation. Slide-to-slide staining intensity variation is introduced due to unintentional variations in tissue sample preparation and staining, which produce artificial (non-biological) differences in stain intensity and colour information. Within-slide staining artefacts include a gradual staining gradient, with stronger staining at one end of the slide progressing to weaker staining at the other, and striping artefacts from slide digitisation. Staining gradients arise due to how the slide is positioned during staining, inconsistent fixation of the tissue sample, and/or uneven application of the reagent [6]. Striping artefacts describes sharp bands of intensity variation across whole slide images, which arise from when stitching together multiple strips of slide during digitization [110]. Though these artefacts could be eliminated at source (e.g. through optimised staining protocols, or an improved slide scanner), they are frequently observed in practice [6], [110]–[113]. Further, the impact of these artefacts on the SAF may not always be obvious at the point of slide preparation. Once these impacts are observed, restaining may be infeasible given the considerable time and manpower already invested, or if

the tissue from the area of interest is no longer available. When unaccounted for, these artefacts may impact the extracted IHC metrics. Second, these manual workflows are time-intensive. This restricts research studies to smaller sample sizes (i.e. less slides and/or subjects), and limits IHC analyses to hand-drawn ROIs, as opposed to analysing voxels from the whole slide.

Here, we propose an automated SAF pipeline to address these challenges. The automated IHC processing pipeline is able to extract SAF maps from high-resolution IHC-stained slides for myelin, neurofilaments and microglia. The key steps are: 1) A data-driven k-means clustering method to derive slide-specific colour information to address between-slide intensity variation 2) a computationally efficient method for stain separation, 3) a simple adaptive thresholding method aimed at robustly segmenting positively stained tissue from background whilst accounting for within-slide staining variations, and 4) the computation of SAF maps at variable resolution scales that can then be directly compared with MRI parameters. Finally, the pipeline was evaluated on an IHC dataset designed to test the pipeline's reproducibility, where we demonstrate how each step improves on approaches common in manual analyses.

3.2 Data acquisition

IHC data was acquired to evaluate our pipeline's performance in terms of reproducibility and robustness to key microscopy artefacts. The aim was to acquire data that can distinguish true biological variation from variance related to artefacts and analysis. Consequently, data was collected from adjacent tissue slides that were separated by the slide section thickness (6 μm), which we assume have similar microstructure and that the true biological between-slide variance is low. This a priori assumption was deemed reasonable as we aimed to summarise microstructure at MRI resolution (0.5–1 mm), which is considerably larger than the slides' separation. Slides were acquired from tissue samples spanning 15 post-mortem brains of patients diagnosed with amyotrophic lateral sclerosis (ALS) and

healthy controls (CTL) (12 x ALS, 3 x CTL, same samples as in [96]. For each of the 15 brains, 12–15 adjacent slides were obtained from the primary motor cortex (face region). These slides were separated into groups of 4–5 slides. Each group of tissue slides was stained using primary antibodies against PLP (myelin), SMI312 (neurofilaments), and CD68 (activated microglia, macrophages), using an identical protocol described by Pallebage-Gamarallage et al. All antibodies were visualised with DAB and sections were counterstained with hematoxylin. Non-specific staining of endogenous peroxidase—an enzyme present in many cells—was minimised through a peroxidise-blocking step [114], [115]. Residual non-specific staining was generally faint except for occasional darker stained vasculature that was sparsely distributed across the slides. Slides were digitised with the Aperio ScanScope®AT Turbo (Leica Biosystems) at x20 object magnification (0.5 μm/pixel).

Prior to analysis, each slide was manually quality-checked where we excluded slides that would fail analysis due to excessive illumination, tears due to poor tissue sectioning or significant amounts of inconsistent staining. In these cases, the data would yield nonsensical SAF maps, regardless of an optimal processing pipeline. Inconsistent staining refers to atypical staining patterns that are non-biological in origin e.g. extremely strong staining gradients, inverted white/grey matter contrasts (opposite to what we neuroanatomically expect) and patchy or unstained tissue. Slides with considerable staining gradients and/or striping artefacts were included. After the quality check, we removed 49% of the CD68 and 24% of the SMI312 slides. No PLP slides were excluded. CD68 slides were mostly removed due to staining artefacts. This is likely due to some difficulty with this batch's staining.

3.3 Stain area fraction pipeline

The pipeline maps RGB intensity values of high-resolution IHC slides (0.5 μm/pixel) to SAF using four steps: colour matrix derivation (c.f. Section 3.3.1), pseudo-non-negative least squares stain separation (c.f. Section 3.3.2), automatic thresholding

for stain segmentation (c.f. Section 3.3.3), and computing the stain area fraction map (c.f. Section 3.3.4). In practice, we found a considerable impact of staining gradients and/or striping artefacts in some slides. This motivated the development of two "configurations" of the pipeline: the default (Figure 3.1) and artefact (Figure 3.2) configuration. Note that the steps in these pipeline were developed empirically due to the lack of prior work or a standardised processing pipeline. The default configuration was designed to emulate an expert histologist when deriving SAF (but with data-driven, slide-specific stain separation and automated thresholding) for IHC slides with no prominent staining gradient and/or striping artefacts. This improves upon a more manual approach, where the manual selection of slide-specific thresholds would be extremely time-consuming. When artefacts are present, we propose the artefact configuration, which automatically adjusts the local thresholds within-slide to account for the impact of staining gradients and/or striping.

Both configurations are automated and differ based on whether local or whole-slide methods are used for Steps 1 (Section 3.3.1) and 3 (Section 3.3.3). The default pipeline requires minimal adjustment and is generalisable to more IHC datasets. The artefact pipeline, while more robust to the presence of some artefact, requires more fine-tuning of pipeline parameters. We now describe each step of the pipeline, how it was evaluated, and the evaluation results.

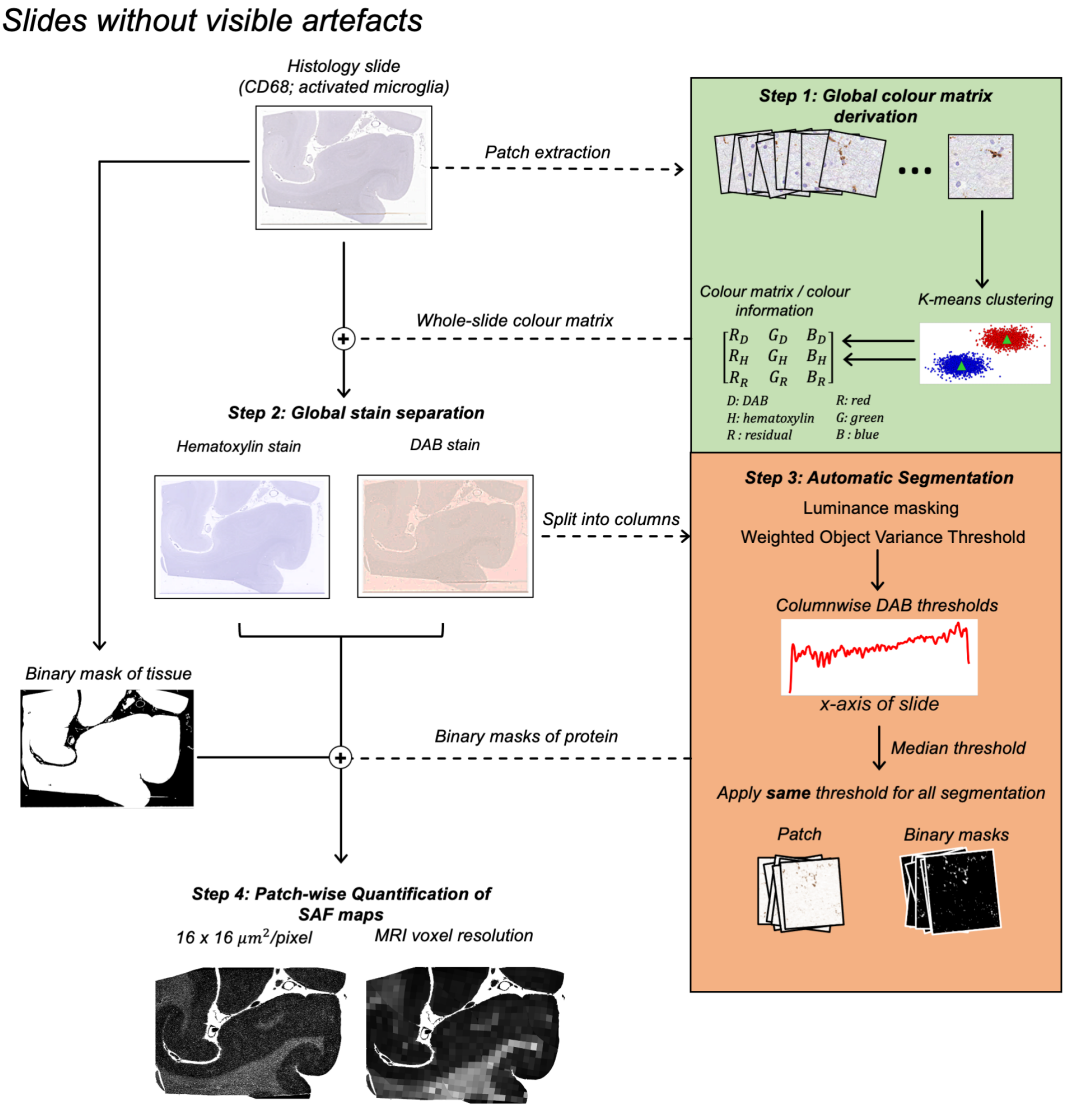

Figure 3.1: The automated SAF pipeline (default configuration) for stains with little or no intensity gradient and/or visible striping artefacts (example: visual cortex). This usually includes stains specifying structures that sparsely populate the brain tissue, such as microglia (Iba1, CD68) and neurofilament (SMI312) in some cases. For each slide, the pipeline 1) derives a single, global colour matrix to separate DAB from hematoxylin, 2) performs stain separation using the pseudo-NNLS method to isolate physically relevant density values of the DAB channel, 3) automatically segments the DAB channel's density with a single median threshold, and 4) calculates a SAF map at variable resolution.

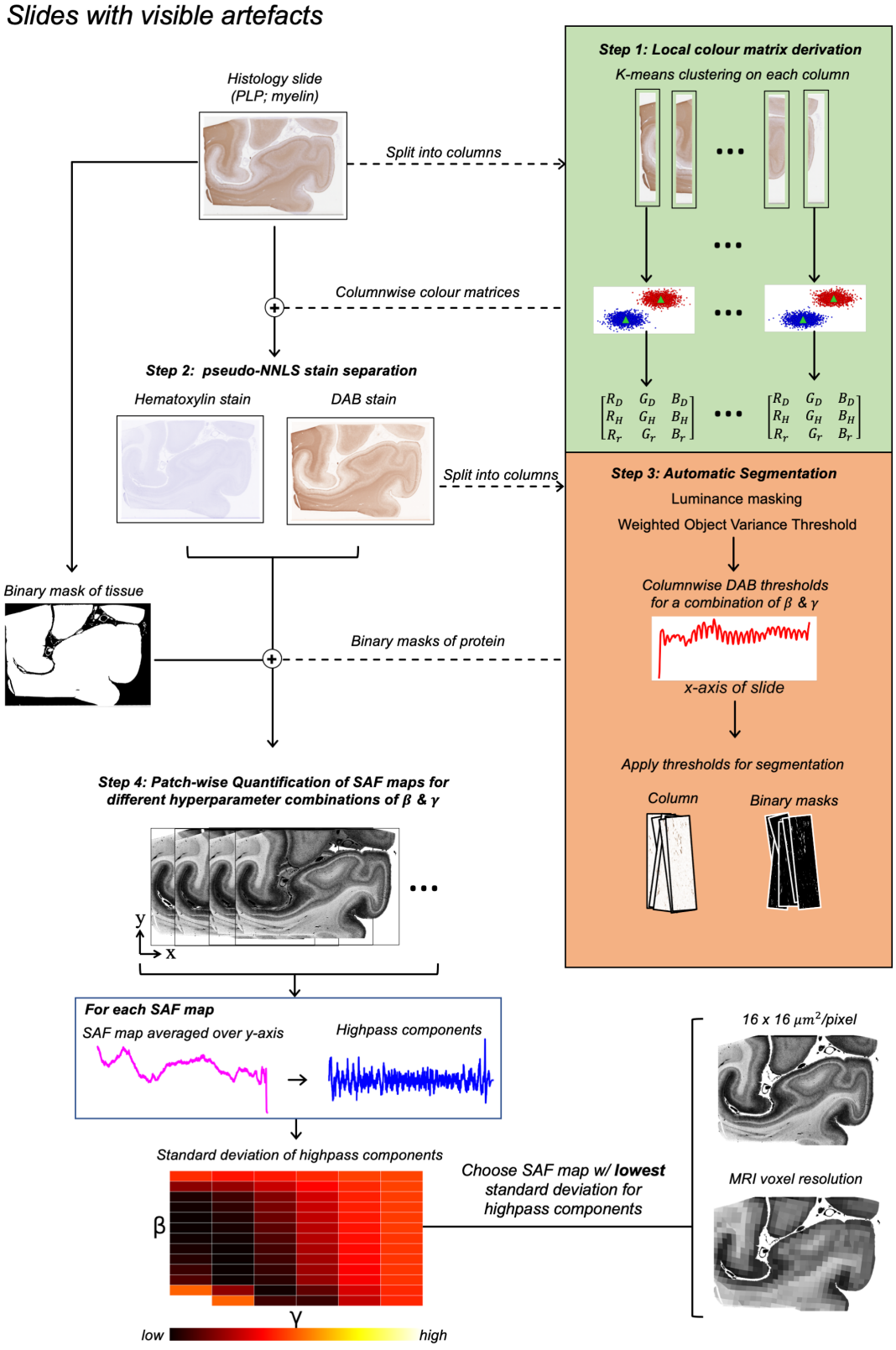
Slides with visible artefacts
Step 1: Local colour matrix derivation
K-means clustering on each column
Histology slide
(PLP; myelin)
Split into columns
Columnwise colour matrices
Step 2: pseudo-NNLS stain separation
Hematoxylin stain
DAB stain
Split into columns
Binary mask of tissue
Binary masks of protein
Step 3: Automatic Segmentation
Luminance masking
Weighted Object Variance Threshold
Columnwise DAB thresholds
for a combination of β & γ
x-axis of slide
Apply thresholds for segmentation
Column
Binary masks
Step 4: Patch-wise Quantification of SAF maps for
different hyperparameter combinations of β & γ
y
x
For each SAF map
SAF map averaged over y-axis
Highpass components
Standard deviation of highpass components
β
γ
low
high
Choose SAF map w/ lowest
standard deviation for
highpass components
16 x 16 μm²/pixel
MRI voxel resolution

Figure 3.2

Figure 3.2: The automated SAF pipeline (artefact configuration) for stains confounded by staining gradient and/or visible striping artefacts (visual cortex). For each slide, the pipeline 1) derives multiple, columnar colour matrices from the data, 2) performs stain separation using the pseudo-NNLS method for each column, 3) automatically segments each column's DAB channel and 4) forms an SAF map. Steps 3 and 4 are repeated for a range of hyperparameters β and γ, which are optimised via grid-search to account for within-slide artefacts (Section 3.3.3). β modulates how much correction is needed to offset the impact of the striping artefact, while γ is a smoothing kernel required to prevent abrupt column-to-column correction. For each SAF map, we averaged the map over its height (y-axis) and chose the SAF map with the lowest standard deviation (i.e. least impacted by these artefacts).

3.3.1 Colour matrix derivation

Theory

Colourimetric analysis was performed using colour deconvolution, a stain separation method using Beer-Lambert's law [25]. In Beer-Lambert's law (c.f. Section 2.2.2), the light absorbance ($\mathbf{A}$) across the three RGB channels is linearly related to the stain density ($\mathbf{C}$) via the attenuation coefficients ($\boldsymbol{\epsilon}$). Hence, the stain (i.e. DAB, hematoxylin) and the leftover staining ("residual") densities in a slide can be computed with a matrix inversion (c.f. Equation 2.3):

$$\begin{bmatrix} C_{DAB} \\ C_{hema} \\ C_{res} \end{bmatrix} = \begin{bmatrix} \epsilon_{DAB,\ red} & \epsilon_{DAB,\ green} & \epsilon_{DAB,\ blue} \\ \epsilon_{hema,\ red} & \epsilon_{hema,\ green} & \epsilon_{hema,\ blue} \\ \epsilon_{res,\ red} & \epsilon_{res,\ green} & \epsilon_{res,\ blue} \end{bmatrix}^{-1} \begin{bmatrix} A_{red} \\ A_{green} \\ A_{blue} \end{bmatrix} = \mathbf{E}^{-1} \begin{bmatrix} A_{red} \\ A_{green} \\ A_{blue} \end{bmatrix} \tag{3.1}$$

where $\mathbf{E}$, termed the colour matrix, is a 3×3 matrix with each element giving the attenuation coefficient ($\epsilon_{i,\lambda}$) for each stain/residual (i) and colour (λ) pair. $\mathbf{E}$ can be defined from literature or empirically measured from single-stained slides [25], [116]. Using an $\mathbf{E}$ that is non-specific to each slide leads to poor stain separation and consequently, inconsistent interpretation of staining density across slides [111], [113], [117]. We address this problem by employing a k-means clustering approach

to derive colour information on a slide-by-slide or local basis directly from the IHC data. This approach is tailored according to the different configurations.

Method

Default configuration To derive a single slide-specific **E**, we used the k-means clustering strategy inspired by [118]. For each slide, the method applied the following steps:

1. Randomly sample patches ($0.064 \times 0.064\ mm^2$; $n = 1000$) from the tissue.

2. Convert the RGB intensities to absorbances (c.f. Equation 2.1):

$$A_\lambda = -log_{10}(\frac{I_\lambda}{I_{0,\lambda}}), \tag{3.2}$$

   where λ is either red, green or blue. $\frac{I_\lambda}{I_{0,\lambda}}$ is the attenuation of light passing through the slide.

3. Convert the absorbances to the hue-saturation-density (HSD) space spanned by c_x and c_y. This is because there is a clearer separation of the DAB and hematoxylin clusters in the HSD space:

$$c_x = \frac{A_r}{A_m} - 1, \tag{3.3}$$

   and:

$$c_y = \frac{A_g - A_b}{A_m\sqrt{3}}, \tag{3.4}$$

   where $A_{r,g,b}$ are the absorbances for red, green and blue, respectively. A_m is the mean absorbance.

4. Perform a k-means clustering (k = 2) on each patch to produce 2 cluster centroids. These centroids are the colour vectors of hematoxylin and DAB for that patch.

5. Measure the Euclidean distance between cluster centroids for each patch. Discard patches with Euclidean distances in the $< 95^{th}$ percentile of all measured Euclidean distances.

6. Perform another k-means clustering (k = 2) on the colour vectors of the remaining patches. The output centroids correspond to the DAB and hematoxylin colour vectors derived from the slide ("slide-specific")

7. Convert the colour vectors from HSV space back to absorbance space.

The final output corresponds to the slide-specific DAB and hematoxylin colour vectors of **E**. The residual was computed as the cross-product of the DAB and hematoxylin colour vectors, as is typically done in [119]. Stain separation was performed using this single **E** across the whole slide.

Artefact configuration In slides with a staining gradient, a locally changing **E** was required to account for colour differences from one end of the slide to the other. Consequently, we applied k-means to derive **E** along the gradient direction. In principle, **E** can be derived in windows of pixels of any arbitrary shape (i.e. square patch) that are large enough to provide a sufficient number of pixels of each class (background versus stain-of-interest) for data-driven analysis. In our datasets, the staining gradient was present along the horizontal axis of the slide. Hence, we applied a single k-means on a column-wise basis (32-pixel width; height matching the slide) to define $\mathbf{E_{column}}$ that varies along the gradient direction. Note that this is identical to how we applied the first k-means on a single patch (i.e. Steps 2 to 4, Section 3.3.1) in the default configuration. We empirically determined the width of the column, beginning with a 4-pixel width and progressively increasing it. The goal was to ensure that there were a sufficient number of pixels in the distribution to effectively apply the segmentation algorithm (refer to Section 3.3.3) and obtain a meaningful output. Stain separation was performed locally using $\mathbf{E_{column}}$.

Evaluation

Our proposed method was compared to two conventional approaches: 1) a colour matrix taken from literature ("literature") and 2) a colour matrix that was manually derived ("manual") by an expert histologist (MPG) using our dataset and a standard colour deconvolution protocol (Aperio version 9.1) [96]. In both cases, a single colour matrix was used for all slides in the dataset.

The colour matrices (automated/literature/manual) were used for stain segmentation (c.f. Section 3.3.3) and the output was evaluated visually based on how different targeted structures (PLP, CD68 or SMI312) were separated from hematoxylin-stained tissue and non-tissue background. We performed our comparison on different WM/GM ROIs sampled from PLP, CD68 and SMI312 slides.

Further, we plotted the DAB and hemotoxylin colour vectors (rows of $\mathbf{E}$) automatically derived from each slide ("slide-specific DAB/hema") alongside the median colour vectors across slides ("study-specific DAB/hema") and the colour vectors taken from the literature ("literature DAB/hema") to visualise how the colour vectors vary across slides and studies, respectively. Here, we assumed the literature colour vectors as a proxy for colour vectors derived from another study (conducted in [25]) to facilitate between-studies comparison.

Results

In Figure 3.3, we show that the DAB staining density derived using the "automated" colour matrix had fewer hematoxylin-stained nuclei compared to the other methods. This indicates that the automated method derives colour matrices that are most specific to the DAB and hematoxylin stains. Although automatically-derived colour matrices show improved stain separation, thresholding is still necessary to remove non-targeted structures (e.g. faintly stained background tissue) that are not fully excluded.

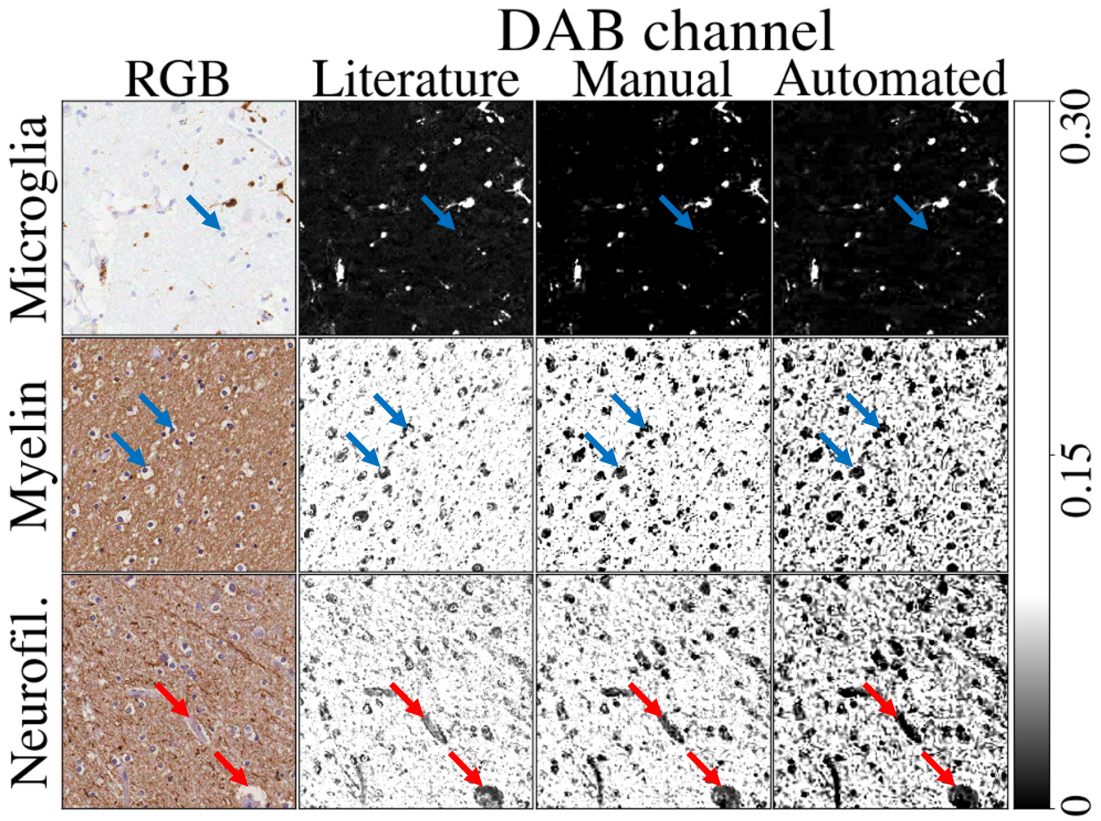

Figure 3.3: RGB patches (column 1) of different stains, along with their corresponding DAB stain density maps that have been computed using the literature (column 2), manually-derived (column 3), and automatically-derived (column 4) colour matrices. Using the literature colour matrix results in poorer stain separation, with structures stained by hematoxylin, such as nuclei and/or blood vessels (blue and red arrows respectively), appearing in the DAB channel.

Figure 3.4 shows how the hematoxylin colour vector from literature is considerably different to that derived from the data, where the between-study variation in colour vectors is larger than within-study variation. In comparison, the literature DAB colour vector is closer to the study-specific DAB colour vector, and within the range of within-study variation. As both the hematoxylin and DAB colour vectors contribute to stain separation, the large difference in hematoxylin literature versus study-specific colour vectors may explain why the literature colour matrix leads to less desirable stain density maps in Figure 3.3.

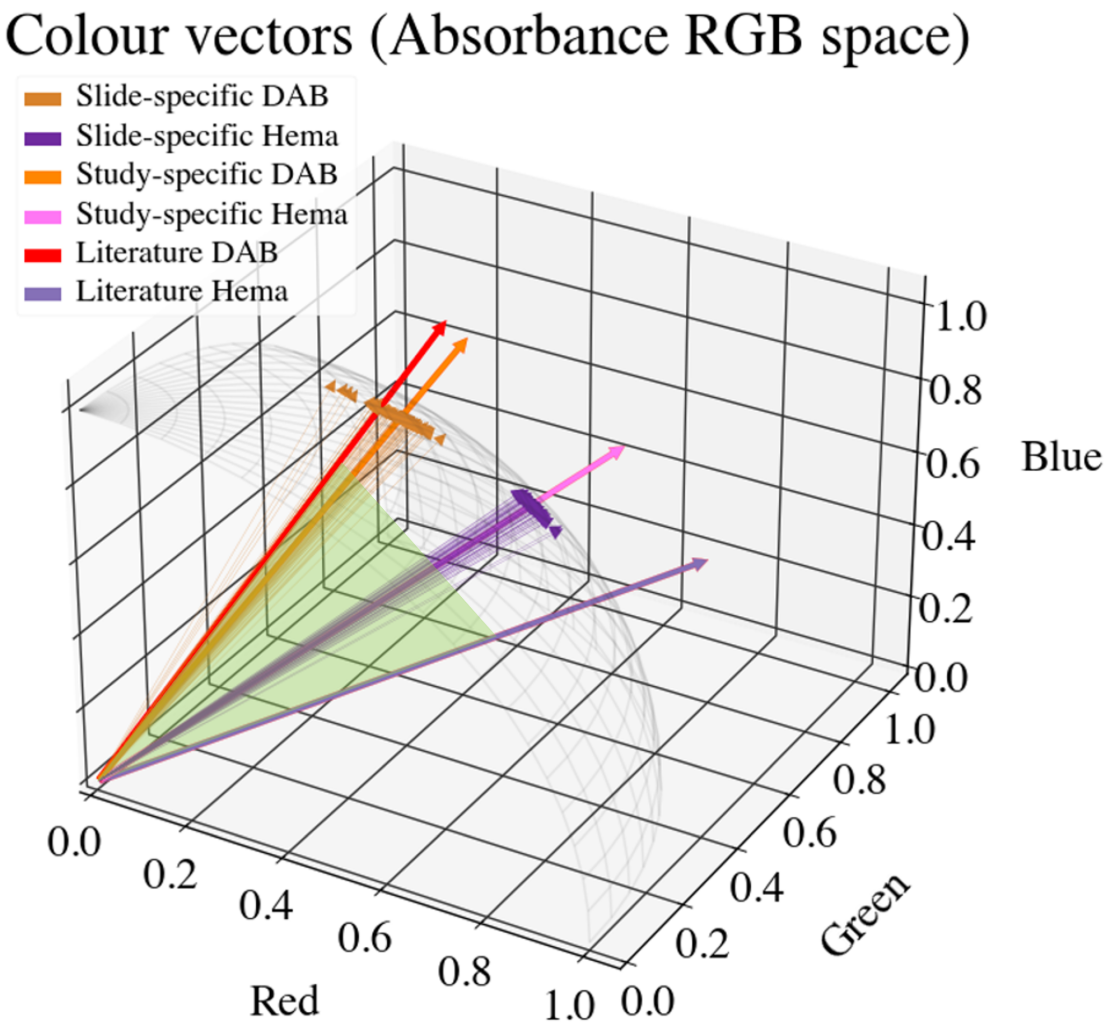

Figure 3.4: DAB and hematoxylin colour vectors in the absorbance RGB space. Note that this is only for visualisation purposes, and that we assumed the literature colour vectors as a proxy for colour vectors derived from another study (i.e. for between-study comparison). We show each slide's colour vectors derived using the proposed data-driven method ("slide-specific DAB/hema"). To illustrate how colour vectors may differ within-study and between-studies, we plotted the "study-specific DAB/hema" colour vectors (i.e. the median colour vectors across all slides within-study) and the literature colour vectors ("literature DAB/hema"), respectively. The plane (green shaded region) bounded by a pair of DAB and hematoxylin colour vector is the example plane we refer to in Figure 3.5

3.3.2 Pseudo-non-negative least squares stain separation

Motivation

Having derived a colour matrix **E**, the estimation of the stain density, **C**, is a least-squares error minimization problem that is typically solved by multiplying the absorbance, **A**, with the inverse of **E**. This is known as a matrix inversion. However, as the rows of **E** (i.e. the stain-specific colour vectors) are not constrained to be orthogonal, some colour vectors can result in values of $C_{DAB/hema}$ that are negative (Figure 3.5, regimes +-). While this matrix inversion is mathematically valid, it leads to a problematic interpretation of CDAB/hema in terms of physical stain concentrations (i.e. $C_{DAB/hema} < 0$ implies that a stain emits, rather than absorbs, light which is unphysical).

The matrix inversion approach is often used in typical workflows using software such as ImageJ or QuPath [116], [119], [120]. This approach is sufficient for the visualisation of key ROIs when performing qualitative analysis (i.e. identifying structures for clinical diagnosis), but prevents physical interpretation of negative staining densities. Alternatively, a well-recognised non-negative technique—non-negative least-squares (NNLS)—has been employed in patch-by-patch microscopy analyses [121]–[123]. However, NNLS is computationally expensive, making it impractical for whole slide stain separation. Hence, we propose a simple method, termed pseudo-NNLS (pNNLS), that is similar to NNLS but more computationally efficient.

Method

pNNLS was designed to emulate the non-negative least squares (NNLS) algorithm. pNNLS first estimates the stain density vector **C** via a standard matrix inversion. In the non-physical case where one stain density (DAB/hematoxylin) is negative, the negative $C_{DAB/hema}$ was set to zero. We then maximised the remaining (hematoxylin/DAB) stain density (and minimised residuals of the overall fit to

the data) by calculating $C_{hema/DAB}$ as the projection of $\mathbf{A}$ onto the colour vector $\epsilon_{\mathbf{DAB/hema}}$ of the remaining stain. This procedure is shown in Figure 3.5a. Note that since all $A_{red,green,blue}$ values are strictly positive, the case of having negative densities for both stains simultaneously is not possible.

Evaluation

The pNNLS method was evaluated against NNLS and a simple matrix inversion using simulated data, where we varied the angle between the DAB and hematoxylin colour vectors (the "colour angle") or the absorbance.

In Figure 3.5, we can see how a smaller colour angle (green) would result in more $\mathbf{A}$ values in the +- regime, and consequently produce more negative stain densities in a matrix inversion. To investigate the colour matrix's impact on the pNNLS solution, a single RGB pixel (R = 255, G = 255, B = 0) known to produce a positive DAB stain density was stain-separated using simulated stain colour vectors with colour angles spanning 0°-90°.

The position of $\mathbf{A}$ relative to the nearest colour vector (red angle in Figure 3.5b) also influences the computed staining densities. If $\mathbf{A}$ is in regime +-/-+, one of the staining densities is negative. In NNLS and pNNLS, the negative stain density is set to 0. The positive staining densities from matrix inversion, and also potentially pNNLS, will then differ from the NNLS solution. We investigated how the relative position of $\mathbf{A}$ impacts the estimated staining densities by fixing the stain vectors and simulating multiple instances of $\mathbf{A}$ for RGB = [0,255].

We assumed positive stain densities derived from NNLS as the ideal solution and evaluated the accuracy of pNNLS and matrix inversion by measuring fractional difference (the percentage change relative to NNLS) of both methods' positive stain densities given different colour matrices $\mathbf{E}$ or absorbances $\mathbf{A}$.

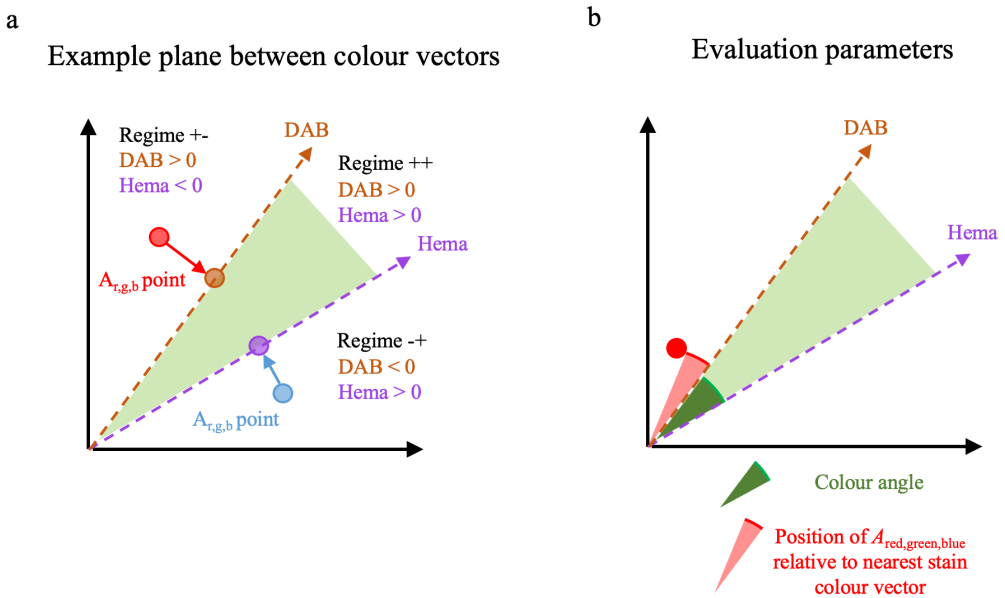

Figure 3.5: A visual overview of the pseudo-non-negative least squares method (pNNLS), and the parameters used to evaluate this method. (a) An example plane bounded by a pair DAB and hematoxylin vectors, as previously shown in Figure 3.4. In this plane, an absorbance **A** data point may inhabit three "regimes": +-/++/–. In regime +-, stain separation via matrix inversion produces a positive DAB and negative hematoxylin. pNNLS improves on this by 1) setting the negative hematoxylin stain density to zero and 2) recalculating DAB density (brown dot) by projecting **A** (red dot) onto the DAB colour vector. This ensures that the measured absorbance **A** is maximally described by the DAB stain. Conversely, in regime -+, the hematoxylin density is positive, and DAB's density is set to zero. The hematoxylin density (purple dot) is determined by projecting **A** (blue dot) onto the hematoxylin colour vector. For the ++ regime, both stain densities from matrix inversion are positive, and no correction is needed. (b) We hypothesised pNNLS to produce similar stain densities to NNLS. We evaluated their similarity by varying two parameters that may influence their output. The parameters are: 1) the colour angle (dark green angle), and 2) the position (red angle) of **A** relative to the nearest stain colour vector.

Results

Figure 3.6 shows that the positive DAB stain densities produced by pNNLS were effectively equivalent to NNLS's densities (green dots tracing zero line), irrespective of the colour angle. Conversely, the DAB stain densities produced via matrix inversion differed greatly from NNLS, with increased fractional differences given smaller colour angles (Figure 3.6; blue dots).

When investigating how the position of **A** relative to the nearest colour vector affects

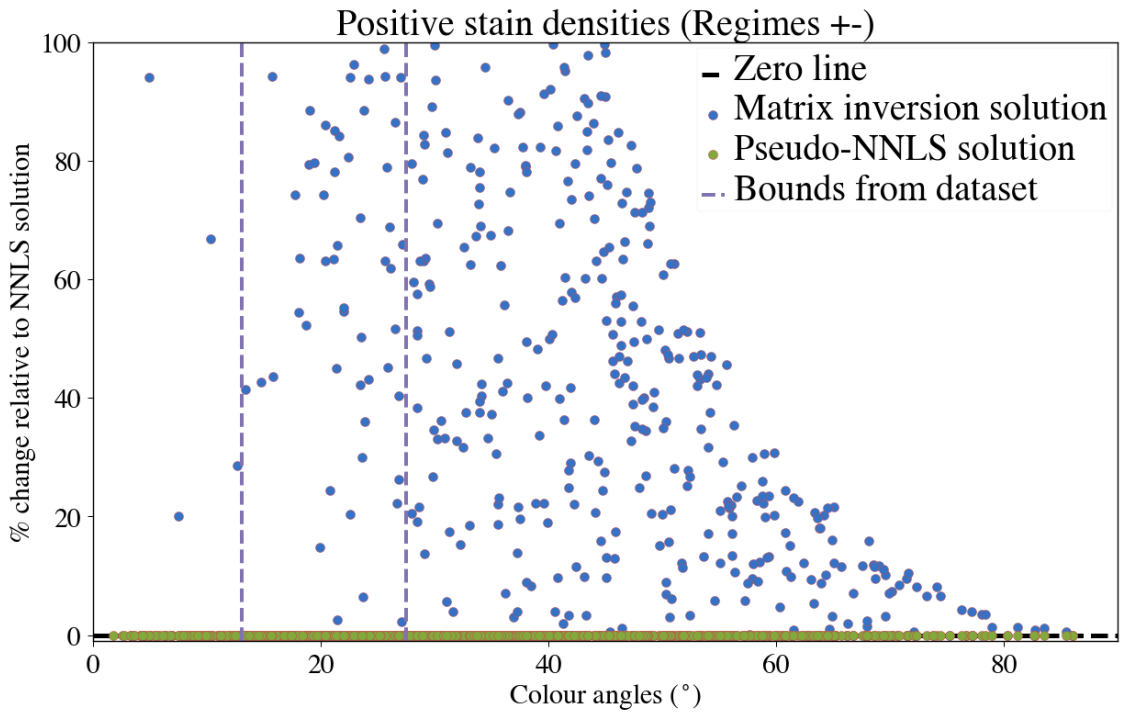

Figure 3.6: Fractional difference (% change relative to NNLS solution) of pNNLS and matrix inversion to NNLS, over all possible colour angles (0°-90°). In the colour angle regime extracted from the dataset (purple dashed), matrix inversion predictions (blue) differ considerably from the NNLS solution, while pNNLS (green) predicts an effectively equivalent solution.

the estimated stained densities, for **A** found in regime ++, the derived positive stain densities were largely identical in all methods (not shown). In regimes +-/-+, the positive stain densities produced from a standard matrix inversion differed significantly from NNLS with increasing relative angles from the nearest colour vector (Figure 3.7; blue dots). However, positive stain densities generated via the pNNLS were found to be almost equivalent to stain densities produced with the NNLS (Figure 3.7; green dots tracing zero line).

3.3.3 Automatic thresholding for stain segmentation

Method

To segment the DAB-stained protein-of-interest from non-specific DAB in the background, manual analyses require an expert to manually set a threshold. We

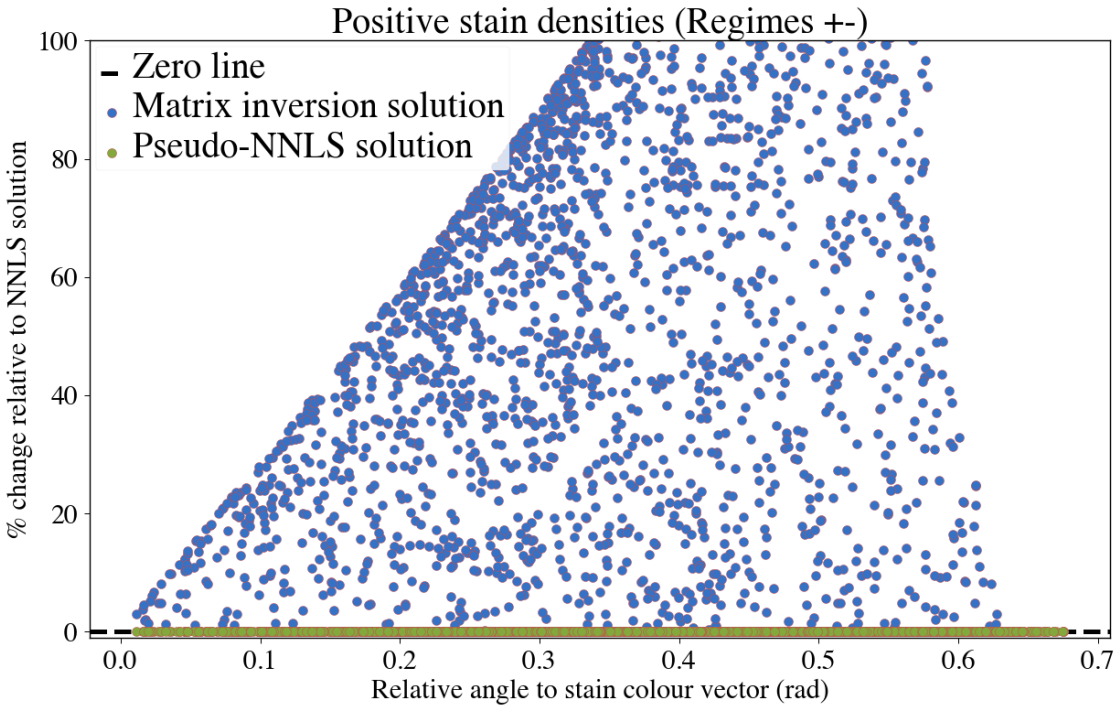

Figure 3.7: The fractional difference was evaluated for **A** with different positions relative to the nearest stain colour vector. Numerous **A** were produced from simulated RGB values ([0,255]). With increasing relative angles to the nearest stain colour vector, the positive stain density estimates from matrix inversion differ from the NNLS solution (blue dots), while pNNLS (green dots) accurately approximates an NNLS solution.

improved on this by deriving a data-driven threshold. An image segmentation approach is Otsu's method [124], which computes a threshold that maximises the image histogram's inter-class variance. Our algorithm is based on the related weighted object variance algorithm, weighted-Otsu or weighted object variance (WOV) [125], which includes a tunable parameter (δ) to better separate classes of unequal count and variance. Here, we computed a threshold t by maximizing:

$$t \;=\; argmax_{\,t} \left[P_0\,(t)\;\mu_0(t)^2 \;+\; P_1(t)^{1+\delta}\;\mu_1(t)^2\right]. \tag{3.5}$$

Here, $P_j(t)$ and $\mu_j(t)$ are the cumulative probabilities and means of the uneven classes $j = 0$ (protein-of-interest) and $j = 1$ (DAB-stained background). δ ranges from -1 to 1 and weights the object variance to shift t closer to the mean of the smaller ($\delta > 0$) or larger ($\delta < 0$) class 0. $\delta < 0$ was used for densely stained

PLP or SMI312 and $\delta > 0$ for sparsely stained slides (CD68, Iba1). If $\delta = 0$, this is equivalent to Otsu's method. To achieve local thresholding, the algorithm was performed on contiguous columns rather than the entire image. Our slides possessed left-to-right gradients in stain density, with vertical bands of intensity (striping). Thresholds t_i were thus calculated on a column-wise basis (32-pixel width; height matching the slide), with i representing the column index. Before calculating the threshold, the DAB channel was masked to remove the non-tissue pixels in the column (luminance < 0.75) to better balance the two classes in the DAB channel histogram. This prevented a large number of non-tissue pixels from skewing the histogram and biasing the threshold.

Default configuration A single threshold was sufficient to segment the entire slide without visible striping artefacts. The fixed threshold was calculated as the median of all local thresholds computed column-wise. Consequently, our data-driven pipeline replaces expert determination of the threshold, t, with the determination of the hyperparameter, δ. Ideally, this hyperparameter is set once by an expert for a stain. Our pipeline will then enable automated, adaptive thresholding on new slides. In this work, we sampled 8–10 patches ($0.5 \times 0.5\ mm^2$) spanning different brain regions, tissue types and subjects to choose a δ (per stain) that produced optimal segmentation. Segmentations were vetted with an expert histologist (MPG).

Artefact configuration In slides with striping artefacts, a single whole-slide threshold is insufficient for optimal segmentation. Our artefact configuration uses column-wise thresholds that adapt to these artefacts in a data-driven way. Columns affected by striping are characterised by DAB histograms with decreased median absolute deviation (MAD) compared to columns less affected by striping artefacts. This was found by empirically comparing histograms from striping and non-striping regions and associating it with an observed slight blurring of the image along the stitching boundary of the slide scanner. Consequently, we used

the MAD from each column (indexed with i) to weight the δ to account for how much striping artefact is present:

$$\delta_i = \alpha\ (1\ +\ \Delta_i)^{\beta}, \tag{3.6}$$

where:

$$\Delta_i\ =\ \frac{MAD_i\ -\ \sigma(MAD_i)}{\sigma(MAD_i)}. \tag{3.7}$$

δ_i is the overall exponent used in the WOV equation (Equation 3.5); α is a stain-specific value chosen manually which depends on the relative positive stain and background staining (equivalent to δ in the default pipeline); β was chosen via grid search and depends on the amount of striping artefact i.e. it modulates how much δ differs from α due to striping; σ is the kernel size of a 1D Gaussian filter applied to MAD_i (σ=16); Δ_i represents the i^{th} column's change in structure (MAD) relative to neighbouring columns. After calculating the column-wise thresholds using Equations 3.5-3.7, we performed a final smoothing operation:

$$t_{final}\ =\ \gamma(t_i), \tag{3.8}$$

where γ is a 1D Gaussian filter that is optimised via grid search that prevents the thresholds (t_i) from varying abruptly column-to-column.

Figures 3.8 and 3.9 demonstrate how the hyperparameters α, β and γ affect the resultant SAF map. α is chosen manually, β and γ were optimised for each slide via grid search to minimise the standard deviation of highpass components (defined below) in the resulting SAF. In our dataset, we observed striping artefacts and/or staining gradients in the PLP slides only. Hence, we applied the artefact

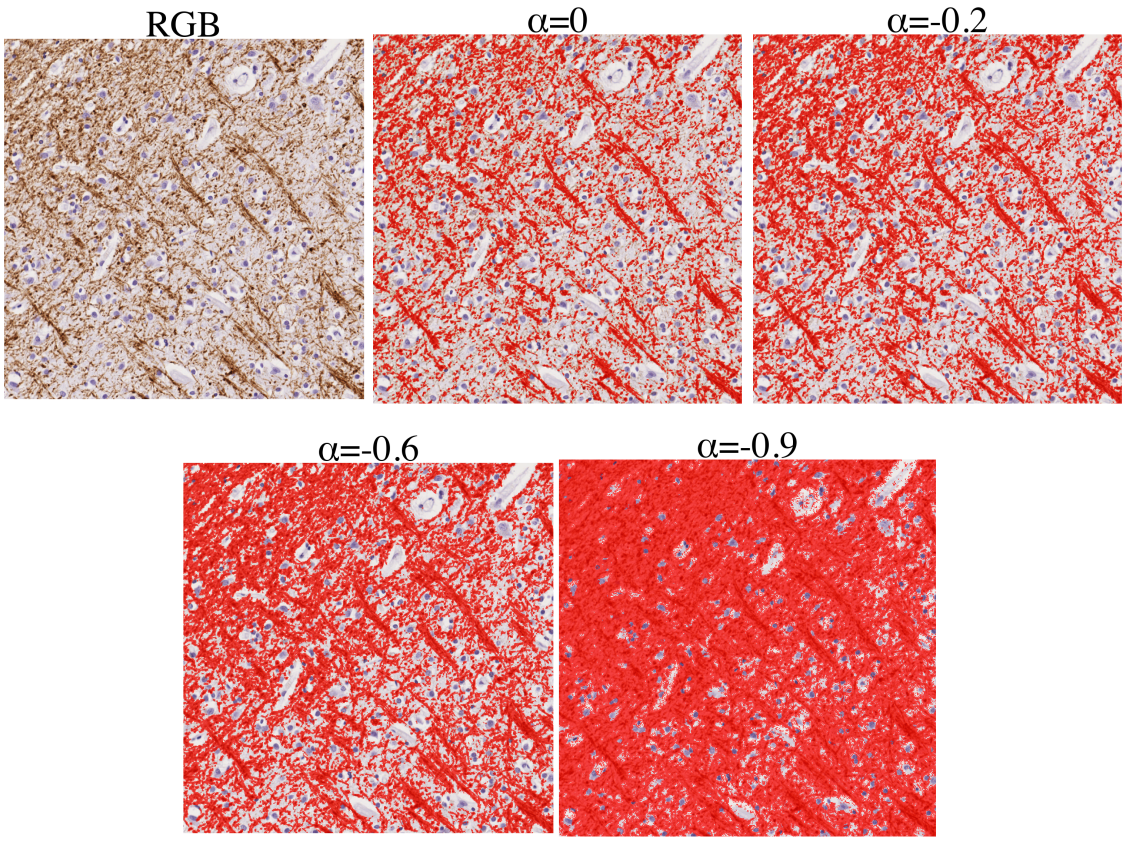

Figure 3.8: Optimising hyperparameter α to produce an accurate segmentation of the target protein. We show this in an example myelin-stained (PLP) patch. The hyperparameter α affects the segmentation of the protein-of-interest. Here, varying α from 0 to -0.9 slowly increases the number of pixels we identify as protein-of-interest. Based on expert input, we identified $\alpha = -0.6$ as optimal for accurately segmenting myelin. Once α is set for a single stain, we apply it to all slides of that stain.

configuration on our PLP slides ($\alpha = -0.60$) and the default configuration on our CD68 ($\delta = 0.05$), Iba1 ($\delta = 0.05$) and SMI312 ($\delta = -0.30$) slides.

Evaluation

The resultant segmentation of this method was vetted by an expert histologist (MPG). All slides of similar stains across the dataset were segmented using the same hyperparameters. Outputs were checked using random patches (8-10 patches per stain) sampled from different brain regions, tissue types, and subjects.

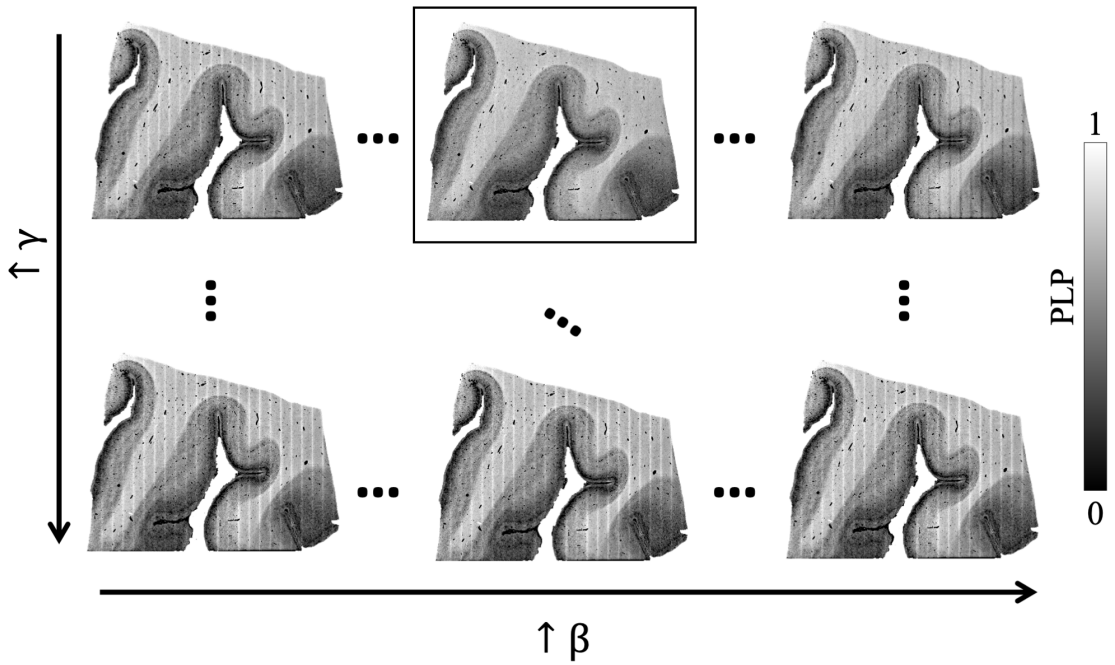

Figure 3.9: Optimising hyperparameters β and γ to produce a resultant stain area fraction map. These hyperparameters directly address the striping artefacts, and are optimised for for each slide using grid search. In this example myelin-stained (PLP) slide, we see substantial striping in the SAF map (top left; $\beta = 0$; $\gamma = 0$), An increase in β is needed to produce segmentation threshold that compensate for changes due to striping present (black square; $\beta = 1.5$, $\gamma = 1$), though a β which is too high may also result in an overcompensation (top right; $\beta = 4$, $\gamma = 1$). Finally, hyperparameter γ is a smoothing kernel applied to the segmentation thresholds, to prevent the thresholding from varying abruptly from column-to-column. If sharper striping is observed, a smaller γ is used. Conversely, over-smoothing these segmentation thresholds (high γ) may also effectively negate adjustments to the thresholds made by β (last row).

Results

Figure 3.10 shows example segmentations where we are able to successfully segment darkly stained DAB from faintly stained background tissue or the hematoxylin counterstain. In general, results with similar segmentation accuracy to Figure 3.10 were observed for all randomly sampled patches.

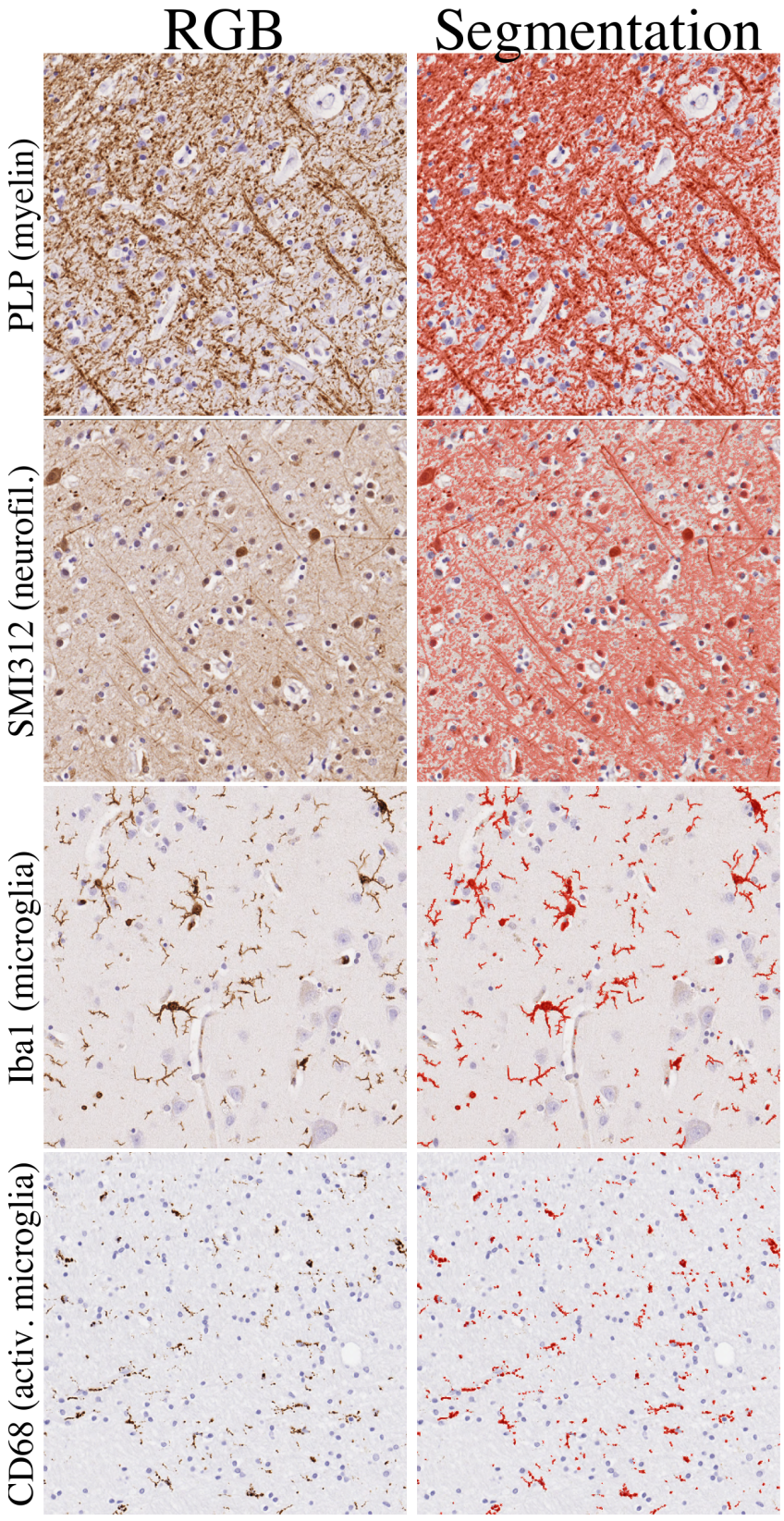

Figure 3.10: Example segmentations (right column; red overlay) produced from the automated SAF pipeline with optimised hyperparameters. The PLP (myelin) and SMI312 (neurofilament) patches were extracted from the WM and GM boundary in the visual cortex, the Iba1 (microglia) patch was sampled from hippocampal GM, and the CD68 (activated microglia) was taken from hippocampal WM.

3.3.4 Stain area fraction map

Method

Following segmentation, we computed SAF maps at various resolutions. First, we extracted a tissue mask by applying Otsu's method [124] on the hematoxylin channel followed by several morphological operations. SAF was defined as the ratio of pixels with positive DAB to those in the tissue mask within a patch. We evaluated the robustness of our pipeline by generating SAF maps at high resolution (16×16 μm^2/patch), which facilitates better identification of high-frequency variations in SAF, and at MRI resolution (0.5×0.5 mm^2/patch), to evaluate the reproducibility of SAF at the resolution used for MRI-SAF analyses.

Evaluation

The overall pipeline was evaluated based on two criteria: robustness to artefacts and reproducibility of SAF. We compared pipeline-derived SAF maps with expert-derived (MPG) SAF maps [96] that used a manually-derived study-specific colour matrix and a stain-specific segmentation threshold. For each stain, the manual threshold was calibrated using at least 10 randomly selected, structurally distinct regions.

Robustness to within-slide artefacts To test the pipeline's robustness to within-slide artefacts, we calculated the average column-wise SAF. This horizontal SAF profile was filtered using three bandpass filters (modelled from a Butterworth filter [126], [127] applied twice) that are sensitive to different artefacts' effects: staining gradients (lowpass; < 3 Hz), striping artefact (bandpass; 3-12 Hz) and bandpass plus all other high-frequency noise (highpass; > 3 Hz). The frequency bands were qualitatively chosen based on the spatial variability of the artefacts, which may differ between datasets. Within each frequency band, we computed the relative

percent change in standard deviation between the manually- and automatically-derived SAF map (diffstd) to quantify the reduction in impact from artefacts:

$$diffstd = \frac{std_{manual} - std_{automated}}{std_{manual}} \cdot 100, \tag{3.9}$$

diffstd was observed to be sensitive to artefacts that increase the variance of SAF across the slide: striping artefacts increase diffstd in the high-frequency band, and staining gradients increase diffstd in the low-frequency band.

Reproducibility of stain area fraction map Reproducibility was tested by registering all within-subject slides to the subject's first slide via TIRL [128]. We compute an SAF percent difference map for each co-registered pair of slides ($SAF_{1,2}$) and take the median value across pixels:

$$diffsaf = median\left[\frac{SAF_1 - SAF_2}{(SAF_1 + SAF_2)/2} \cdot 100\right]. \tag{3.10}$$

Results

Robustness to within-slide artefacts The evaluation dataset slides were processed with either the default (CD68, Iba1) or artefact (PLP, SMI312) pipeline. Figure 3.11 compares SAF maps from both our automated and manual pipeline. Both configurations of the automated pipeline reduce the impact of striping artefacts. In the default configuration, this can be attributed to the use of a slide-specific colour matrix, which results in better stain separation compared to the non-specific colour matrices used in manual analyses. The artefact configuration also reduced staining gradient artefacts. In slides with less noticeable artefacts (Iba1), the manual and automated pipelines produce similar results.

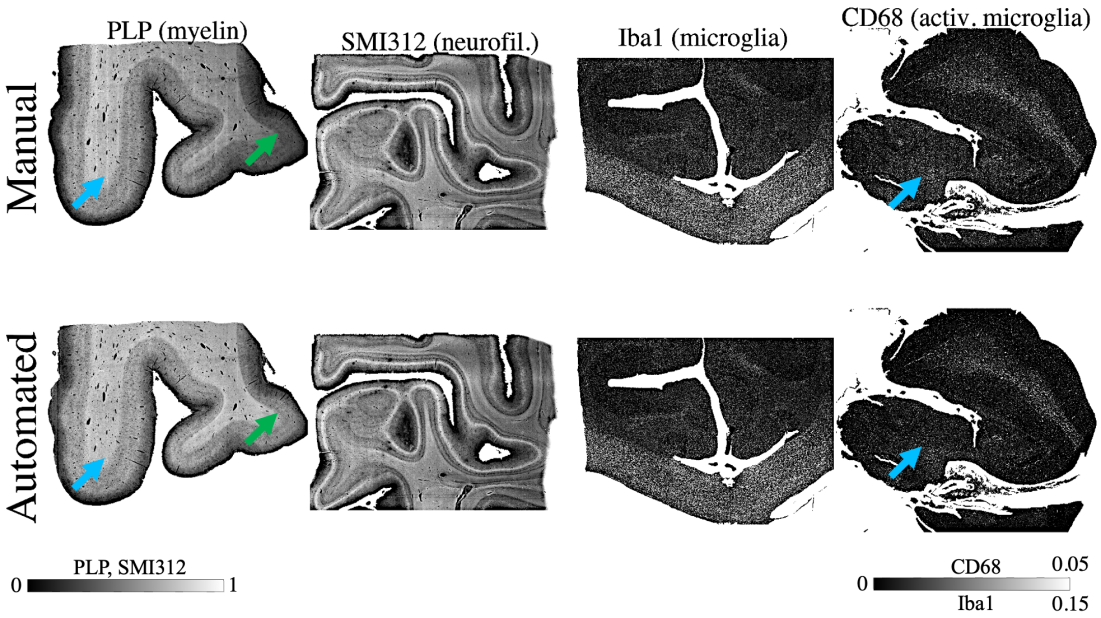

Figure 3.11: Within-slide artefacts are reduced using the automated pipeline (bottom row). These include noticeable striping artefacts (blue arrows) and staining gradients (green arrows) originally seen in manually-derived SAF maps (top row).

In almost all PLP and SMI312 slides (Figure 3.12), the diffstd for each frequency band (Equation 3.9) was positive, suggesting a reduction in artefacts for the automated pipeline. The positive lowpass diffstd implies reduced staining gradients, and the reduced bandpass and highpasss diffstd values suggest reduced striping artefacts. Further, there was a high similarity in highpass and bandpass diffstd. This implies the striping artefact's major contribution to overall noise in these slides, and how its impact is especially mitigated with the automated pipeline. The results for CD68 are less conclusive. The automated pipeline reduces the impact of the striping artefact (bandpass diffstd is mostly positive) but performs worse than the manual pipeline for the highpass and lowpass filters.

Reproducibility of stain area fraction map Reproducibility of SAF maps (Figure 3.13) was quantified with diffsaf (Equation 3.10) between within-subject adjacent slides. Manual and automated pipelines were found to have similar reproducibility with a median diffsaf of around 5% (PLP), 9% (SMI312) and 20% (CD68). In, Figures 3.12 and 3.13, CD68 has fewer datapoints than other stains

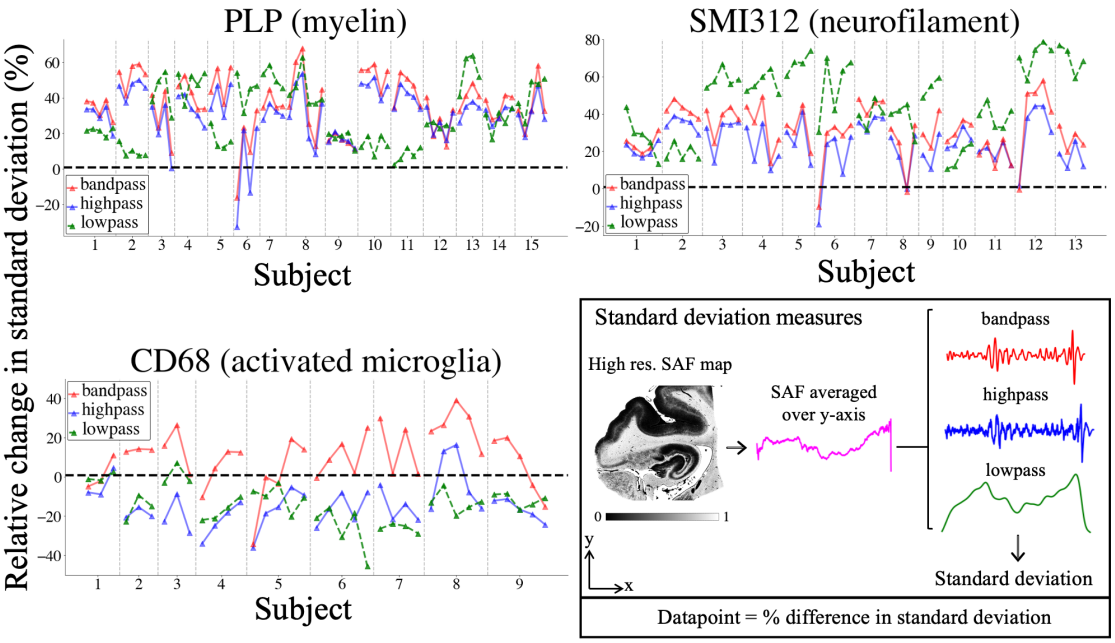

Figure 3.12: Quantitatively comparing the impact of within-slide artefacts in the manual and automated processing pipelines, as measured using the relative change in standard deviation ($100 \times (std_{manual} - std_{automated})/std_{manual}$). Standard deviation measures (box) are derived by 1) averaging the high-resolution (16 μm/pixel) SAF map along the y-axis, 2) filtering it to produce 3 components (bandpass, highpass and lowpass), and 3) computing the components' standard deviation. The lowpass filter isolates the staining gradient artefact, whilst the striping artefact only is captured with the bandpass filter. The highpass filter combines the same striping artefact with all high-frequency noise. Each IHC slide is represented as a single data point, and slides from the same subject are grouped together and connected by lines. A positive (negative) value indicates that the automatically-derived SAF map is less (more) affected by the associated artefact than the manually-derived SAF map.

since fewer slides were used when evaluating CD68 (9/15 subjects; 37/73 slides) than in SMI312 (13/15 subjects; 55/72 slides) and PLP (15/15 subjects; 73/73 slides) after manual quality control (c.f. Section 3.2).

3.4 Discussion

To facilitate high-throughput MRI-microscopy analyses, we proposed an automated pipeline to extract stain area fraction (SAF) from immunohistochemical (IHC)

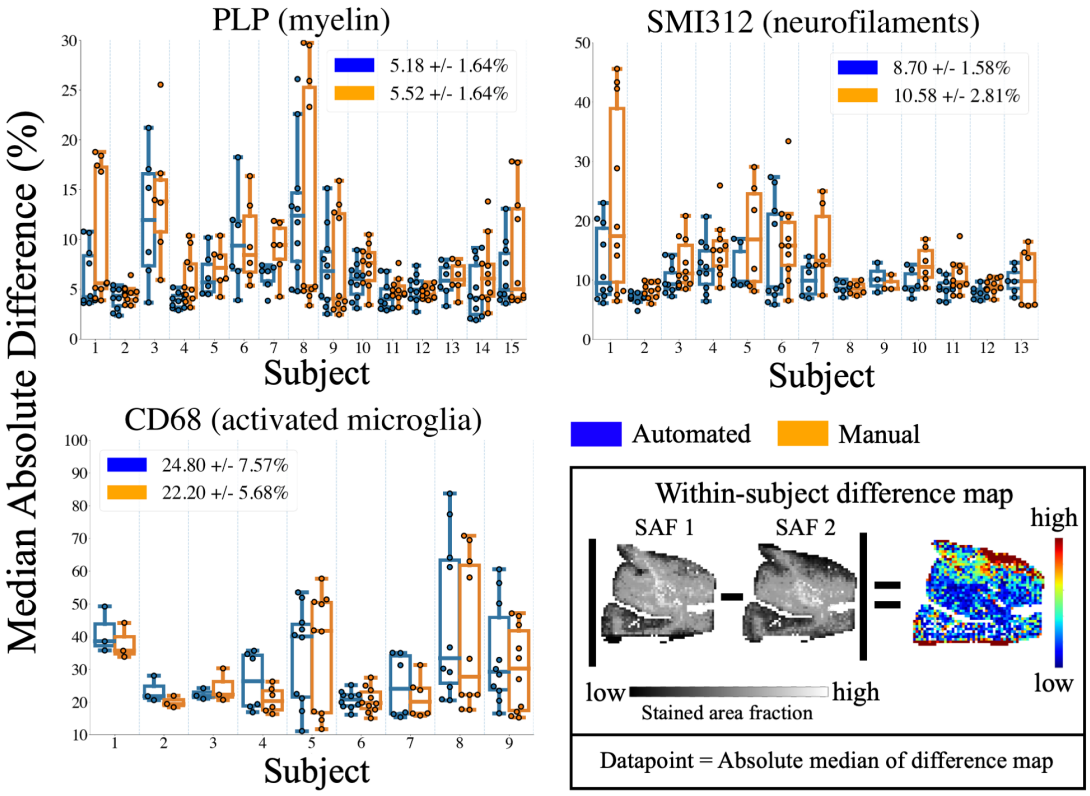

Figure 3.13: The reproducibility of SAF values across adjacent tissue sections, as measured by the median absolute difference. The median absolute difference (box) was computed by 1) taking the absolute difference of a pair of SAF maps produced from IHC slides extracted from the same region and subject, 2) normalising this difference map by the mean of both SAF maps, and 3) taking the median to represent one datapoint. We used this measure to compare the reproducibility of both manually- (orange) and automatically-derived (blue) SAF maps for PLP, SMI312 and CD68. The median and median absolute variance of data points are also shown for each method (legends). Note the change in the scale-bars, where the difference values for CD68 were generally larger when compared to PLP and SMI312.

stains. Crucially, this pipeline was designed to be robust to staining artefacts found in our IHC data. This allows us to extract robust, quantitative IHC metrics at the voxel level and thus facilitates more meaningful MRI-microscopy comparisons (c.f. Chapter 4). This was achieved using data-driven methods, including a clustering approach to derive colour information from the slide, a computationally efficient method for stain separation, and an automated method for segmenting protein structures specifically stained in the DAB channel. Finally, our pipeline was evaluated in terms of reliability and robustness to key IHC artefacts using a dedicated

IHC dataset. The pipeline successfully addressed staining gradients and striping artefacts, while obtaining similar reproducibility to manually-derived SAF maps.

The pipeline's default configuration was designed to automate most of what an expert histologist undertakes to derive SAF, where our automated and data-driven approach enables high-throughput analyses across multiple slides and subjects. Our method further improves on the manual approach by achieving slide-specific stain separation and segmentation. We recommend first using the pipeline's default configuration as it requires minimal fine-tuning and can easily be applied "out-of-the-box" to different IHC datasets. If significant impact from staining gradients or striping artefacts is observed in the output SAF maps, we suggest employing the pipeline's artefact configuration in subsequent analyses.

Our approach has three advantages over previous studies. First, while most MRI-SAF studies use manually-derived SAF, our pipeline deploys data-driven algorithms [118], [125]. This enables the pipeline to be applied rapidly to larger datasets without expert intervention. Second, our pipeline can handle key artefacts (i.e. non-biological sources of variation) that impact SAF maps. This is an improvement over previous automated pipelines [129]–[131]. Third, the pipeline is generalisable to multiple IHC stains, allowing for analysis spanning multiple microstructural sources. This may enable standardised analyses for the voxelwise comparison of multiple microstructural features to MRI [22].

Our results demonstrate how slide-specific colour matrices are beneficial during stain separation as they provide a more accurate representation of colour information in the presence of possible between-slide or between-study variations. This resulted in less hematoxylin stain leaking into the DAB channel for stain separation with data-derived colour matrices. During stain separation itself, most pipelines also do not deal with non-physical negative stain densities produced from a standard matrix inversion. This may be problematic for more quantitative analysis. To address this, we implemented a pNNLS method that accurately approximates an

NNLS solution in an efficient manner, where NNLS would otherwise be infeasible on whole-slide images. Through simulations, we confirmed that the stain densities derived from both pNNLS and NNLS are effectively identical. Overall, our results suggest that we can use pNNLS as a computationally efficient method to compute non-negative stain densities.

We demonstrated the pipeline's robustness to common IHC artefacts, while maintaining similar reproducibility to manually-derived SAF values (Figure 3.13). This was especially evident in PLP and SMI312 slides, which displayed noticeable within-slide artefacts. Conversely, CD68 appeared less reproducible for both manual and automated processing. CD68 stains sparse, small, activated microglia (soma diameter$\sim$ 10 μm [132]). Here, the diffstd metric may be unsuitable as the assumption of low biological variability across slides may not be met. Inspection of the CD68 segmentation revealed that the automated pipeline correctly segmented more activated microglia relative to the manual method. The inclusion of more sparsely distributed microglia may add biological variability to the SAF, resulting in higher low- and highpass diffstd. Staining gradients were not visibly present in CD68 slides, though some striping was visible on the manually-derived SAF maps. The automated pipeline reduced this striping, as reflected in the improved bandpass diffstd.

There are limitations to this SAF pipeline. First, our SAF pipeline does not address smaller-scale within-slide artefacts, such as artefactual staining of vasculature and tissue folding artefacts that arise due to improper tissue preparation (c.f. Section 2.2.1). These artefacts might bias estimated SAF. Since our analysis occurs at the whole-slide level, manually excluding all smaller-scale artefacts would be very time-intensive. Following a qualitative check of the slides, we observed the staining of vasculature and folding artefacts to be relatively sparse, with a tendency to appear on the tissue edges. We do not anticipate the effect size of these artefacts to be significant. Second, we manually performed the quality check on the dataset to remove any slides that would fail analysis due to excessive illumination, poor

tissue sectioning or inconsistent staining. Although quality checks are typically done manually, future studies will benefit from using a more automated approach (e.g. HistoQC [133]). Finally, the SAF pipeline still requires the user to manually set a segmentation hyperparameter per protein for each batch of slides. Though other pipelines may similarly require an input parameter (e.g. a segmentation threshold) to be manually set per batch, they do not directly address within-slide and between-slide variations. Addressing these variations would require the setting of a slide-specific segmentation threshold or multiple within-slide thresholds—a process that requires significantly more time and effort relative to what we have proposed. Nevertheless, future work may benefit from fully automated approaches [134].

3.5 Conclusion

We have developed an automated pipeline that extracts SAF maps from IHC slides. By design, the pipeline is generalisable to multiple IHC stains and has proven robust to artefacts from tissue staining and/or slide digitisation. This was achieved whilst maintaining reproducibility comparable to that derived by experts, suggesting its usability or large-scale analysis of IHC data. By utilising this pipeline to analyse IHC data that has been co-registered with MRI data obtained from the same brain, we can now explore voxelwise comparisons between MRI- and IHC-derived parameters (c.f. Chapter 4).

3.6 Data availability

The code for this work is publicly available at `https://git.fmrib.ox.ac.uk/spet4877/ihcpy`.

3.7 Acknowledgements and contributions

I would like to express my sincere gratitude to Menuka Pallebage-Gamarallage and Adele Smart for acquiring and evaluating the microscopy data and analysis results. I am also grateful to Istvan N. Huszar for designing the acquisition of the microscopy data and co-registering the microscopy data for slide-to-slide comparison. I am grateful to the donors and benefactors of the Oxford Brain Bank who kindly provided all human tissues for this study. I conceived the study design, developed the histology processing pipeline, conducted data simulations and analyses, and drafted the paper.

4

Disentangling the contributions of myelin, neurofilament & microglia to MR contrast: a voxelwise MRI-IHC comparison

Contents

Foreword

Understanding the relationship between MRI parameters and the underlying biology has long been a challenge in neuroscience research. To bridge this gap, we utilised high-quality MRI-IHC co-registrations and performed whole-slide voxelwise comparisons (simple correlations, partial correlations and multiple regression analyses) between multimodal MRI- and IHC-derived parameters. Our partial correlation results suggest that some simple MRI-SAF correlations should be interpreted with caution, due to the co-localisation of other tissue features (e.g. myelin and neurofilaments). Further, we find activated microglia—a generic biomarker of inflammation—to consistently be the strongest predictor of high DTI FA and low RD, which may suggest sensitivity of diffusion MRI to aspects of neuroinflammation related to microglial activation, even after accounting for other microstructural changes (i.e. demyelination, axonal loss and general microglia infiltration). Together, these results show the utility of our methods in carefully curating IHC data and performing multimodal analyses to better understand microstructural relationships with MRI.

Publications relating to this work

Journal articles:

Kor DZL, Jbabdi S, Huszar IN, Mollink J, Tendler BC, Foxley S, Wang C, Connor S, Smart A, Ansorge O, Pallebage-Gamarallage M, Miller KL*, Howard AFD* "An automated pipeline for extracting histological stain area fraction for voxelwise quantitative MRI-histology comparisons", NeuroImage. 2022;264:119726. doi:10.1016/j.neuroimage.2022.119726

Huszar IN, Pallebage-Gamarallage M, Bangerter-Christensen S, Brooks H, Fitzgibbon S, Foxley S, Hiemstra M, Howard AFD, Jbabdi S, **Kor DZL**, Leonte A, Mollink J, Smart A, Tendler BCT, Turner MR, Ansorge O, Miller KL*, Jenkinson M* "Tensor image registration library: Deformable registration of stand-alone histology images to whole-brain postmortem MRI data", Neuroimage. 2023;265:119792. doi:10.1016/j.neuroimage.2022.119792

Conference proceedings:

Kor DZL, Jbabdi S, Huszar IN, Mollink J, Tendler BC, Foxley S, Wang C, Connor S, Smart A, Ansorge O, Pallebage-Gamarallage M, Miller KL*, Howard AFD* "Extracting histology stain area fraction for quantitative comparisons with multimodal MRI ", Proceedings of the Post Graduate the British and Irish Chapter of the ISMRM Hybrid Symposium, London, 2022.

Kor DZL, Jbabdi S, Huszar IN, Mollink J, Tendler BC, Foxley S, Wang C, Connor S, Smart A, Ansorge O, Pallebage-Gamarallage M, Miller KL*, Howard AFD* "Disentangling the contributions of myelin, neurofilament & microglia to MR contrast: an automated pipeline for voxelwise MR-histology analysis", Proceedings of the 30th Annual Meeting of the ISMRM, London, 2022.

4.1 Introduction

This chapter directly continues from Chapter 3, where we introduced and evaluated an automated pipeline to extract SAF maps from microscopy slides stained for multiple proteins-of-interest. In this chapter, we demonstrate how the SAF pipeline can be deployed as part of a larger MRI-microscopy workflow to perform large-scale MRI-microscopy comparisons and elucidate relationships between MRI signals and the underlying tissue features. Here, we applied the pipeline to a second dataset containing co-registered IHC and MRI to correlate SAF related to myelin, neurofilaments and microglia on a voxelwise basis with diffusion-weighted MRI (fractional anisotropy: FA; mean, radial, axial diffusivity: MD, RD, AD) and relaxometry (R_2^*, R_1) maps. To account for covariance between stains, we use partial correlation to identify the unique variance in MRI parameters explained by each targeted protein. Finally, we perform multiple regression with all stains to derive a predictive model of each MR parameter, which may be driven by multiple microstructural sources.

4.2 Data acquisition

We utilised data acquired for a previously published study [96] that contains microscopy and co-registered MRI data of tissue samples from 15 postmortem brains of patients diagnosed with ALS and healthy controls (CTL) (12 x ALS, 3 x CTL). These tissue samples span multiple brain regions with varying levels of disease pathology. Whole brain postmortem MRI data were acquired, after which tissue samples were extracted for the curation of microscopy data.

4.2.1 MRI data

The postmortem MRI acquisition and pre-processing have been previously described [96], [103], [135]. Whole brains were imaged in a 7T human scanner (Siemens Healthcare, Erlangen, Germany) using a 1Tx/32Rx head coil. R_2^* maps were estimated from susceptibility-weighted data acquired with a 3D multi-echo gradient echo sequence (parameters: TEs = 2, 8.6, 15.2, 21.8, 28.4, 35 ms with monopolar readout and non-selective RF pulse, TR = 38 ms, flip angle = 15°, bandwidth = 650 Hz/pixel, and in-plane resolution = 0.5 × 0.5 mm^2 [103]). R_1 maps were estimated from T_1-weighted data collected with a multi-TI turbo spin-echo sequence (Subject 1,2: TE = 14.2 ms, TR = 1000 ms, TIs = 30, 60, 120, 240, 480, 935 ms, flip angles = 180°, bandwidth = 130 Hz/pixel, and in-plane resolution=1.0 × 1.0 mm^2 [96]). Other brains were imaged with slightly different parameters (Supplementary Materials in [136]). Diffusion tensor maps of FA, MD, AD and RD were estimated from a diffusion-weighted steady-state free precession sequence, as detailed in [135] (parameters: TE = 21.0 ms, TR = 28.0 ms, flip angles = 24°, 94°, bandwidth = 393 Hz/pixel, q value=300 cm^{-1}, number of directions/flip angle = 120, and resolution = 0.85 mm isotropic). Note that our diffusion tensor maps were derived differently to what is typically done [60].

4.2.2 Microscopy data

After postmortem MRI, tissue samples were extracted and stained, as previously described in [96] and Section 3.2. In brief, the 6 μm thick sections were sampled from the visual cortex (both hemispheres), anterior cingulate (cingulum bundle, corpus callosum) and hippocampus and stained using primary antibodies against PLP (myelin), SMI312 (neurofilaments), Iba1 (microglia), and CD68 (activated microglia, macrophages). These antibodies have applications in pathological and healthy tissue ([86], [87] for PLP, [88]–[90] for SMI312, [18], [91]–[93] for CD68 and Iba1]) and are relevant to ALS neuropathology, which is characterised by neuronal loss and

microglial activation in motor neuron areas [96]. Antibodies were visualised with DAB and sections were counterstained with hematoxylin. A peroxidase blocking step was used to remove non-specific background staining due endogenous peroxidases. Slides were also digitised at x20 object magnification (0.5 μm/pixel).

We applied our SAF pipeline (c.f. Chapter 3) on to this microscopy dataset to generate SAF maps. We considered data from the visual cortex (both hemispheres), anterior cingulate (cingulum bundle, corpus callosum), and hippocampus. Although the motor cortex is of interest when investigating ALS neuropathology, samples from the motor cortex were not analysed due to the unavailability of co-registered MRI and IHC data when conducting the study. All slides passed the manual quality check criterion, as previously described in Section 3.2.

4.2.3 Co-registration of MRI and histology

MRI and histology data were previously co-registered using FSL's Tensor Image Registration Library (TIRL), which is a general-purpose image registration framework designed for MRI-microscopy co-registration [128]. We used TIRL to 1) register PLP with structural MRI (2D-3D) and 2) co-register other stains to PLP (2D-2D). PLP was chosen as the reference microscopy data due to its strong white/grey matter (WM/GM) contrast. All MRI parameters maps were first aligned to the structural MRI using FLIRT [137]. The generated warps were combined using TIRL to map these MR parameters to the IHC SAF maps for voxelwise correlations. To investigate relationships in WM voxels, WM masks were derived from maps of the third eigenvalue of the diffusion tensor using FSL-FAST [138]. WM masks were similarly resampled into the 2D PLP space.

4.3 Method

We describe an end-to-end workflow for MRI-SAF comparisons (Figure 4.1). At the centre of this workflow is our automated SAF pipeline (Section 4.3.1), as previously introduced and evaluated in Chapter 3. The pipeline was applied to the multiple-region dataset, which includes IHC and co-registered MRI, facilitating voxelwise MRI-SAF comparisons. We describe how we evaluated the quality of the co-registration (Section 4.3.2) and performed voxelwise MRI-SAF analyses (Sections 4.3.3, 4.3.4) to disentangle the contributions of multiple microstructural features stained with IHC to each MR parameter.

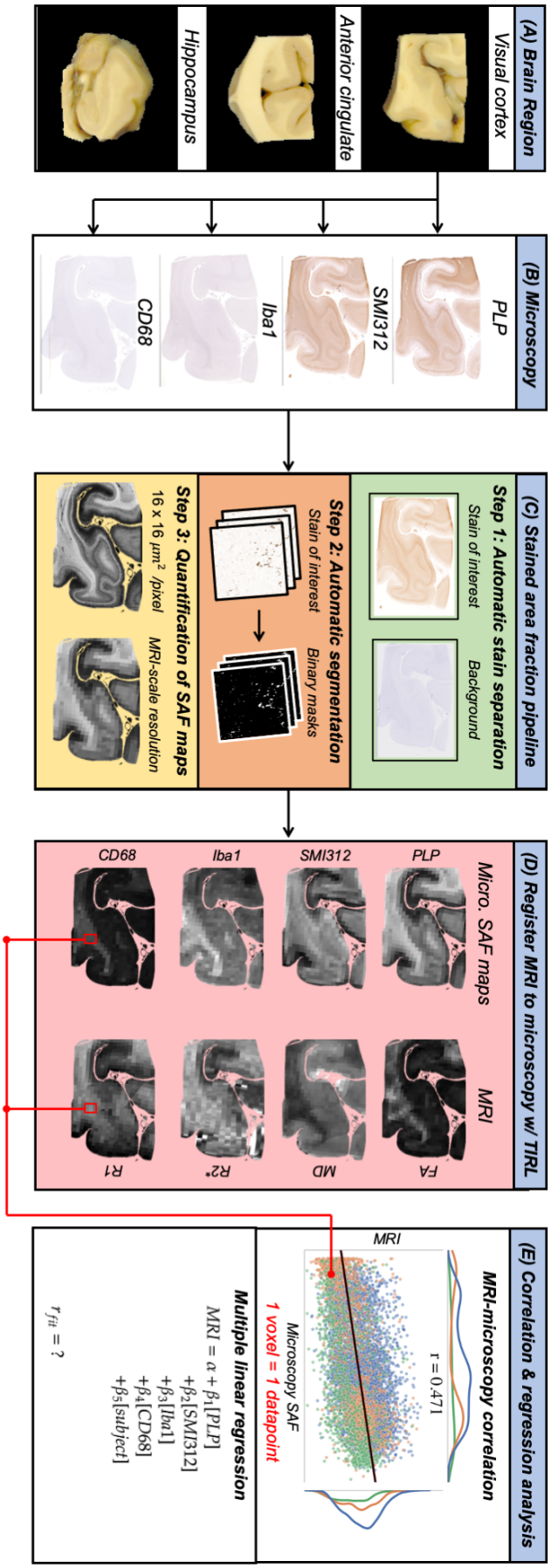
(A) Brain Region
Visual cortex
Anterior cingulate
Hippocampus
(B) Microscopy
PLP
SMI312
Iba1
CD68
(C) Stained area fraction pipeline
Step 1: Automatic stain separation
Stain of interest
Background
Step 2: Automatic segmentation
Stain of interest
Binary masks
Step 3: Quantification of SAF maps
16 x 16 μm² /pixel
MRI-scale resolution
(D) Register MRI to microscopy w/ TIRL
Micro. SAF maps
PLP
SMI312
Iba1
CD68
MRI
FA
MD
R2*
R1
(E) Correlation & regression analysis
MRI-microscopy correlation
MRI
Microscopy SAF
1 voxel = 1 datapoint
r = 0.471
Multiple linear regression
MRI = α + β1[PLP]
+β2[SMI312]
+β3[Iba1]
+β4[CD68]
+β5[subject]
r_fit = ?

Figure 4.1

Figure 4.1: An overview of the MRI-microscopy workflow. A: Brain regions were sectioned for immunohistochemistry (IHC). B: Slides are stained for myelin (PLP), neurofilament (SMI312), activated microglia (CD68) and all microglia (Iba1). C: IHC slides are processed to output stain area fraction (SAF) maps (described in Section 3.2). D: SAF and MRI maps are then co-registered voxelwise via TIRL [128]. E: Voxels are pooled to perform pairwise correlations and multiple regression between MRI and SAF. Each datapoint in the scatter plot represents a single voxel; the colours represent data from different brain regions (green for visual cortex, orange for anterior cingulate and corpus callosum, blue for hippocampus).

4.3.1 SAF pipeline

The SAF pipeline maps RGB intensity values of high-resolution IHC slides ($0.5\mu m$/pixel) to SAF using steps previously described (c.f. Chapter 3). The pipeline is automated and data-driven, enabling rapid analysis of many IHC slides which we demonstrate by applying the pipeline to our dataset spanning different human brains, brain regions and stains (32 slides in total). In this dataset, stitching artefacts and/or staining gradients were present in the PLP slides only. Therefore, the pipeline's artefact configuration (c.f. Chapter 3, Figure 3.2) was used for the PLP slides ($\alpha = -0.60$), while the pipeline's default configuration (c.f. Chapter 3, Figure 3.1) was applied on the CD68 ($\delta = 0.05$), Iba1 ($\delta = 0.05$) and SMI312 ($\delta = -0.30$) slides.

4.3.2 Co-registration of MRI and microscopy

The quality of the registration was evaluated according to the alignment of contours representing tissue boundaries and WM/GM contrast. Contours were derived from the PLP SAF maps.

4.3.3 Voxelwise MRI-SAF analyses

MR parameter maps (3D) were resampled into PLP (2D) space for correlation with SAF. Here, we assumed that the 2D projection of each MR voxel was representative

of the whole 3D MR voxel, which may be sensible in homogeneous voxels with a single tissue type. In more heterogeneous voxels (e.g. at the WM-GM boundary), this assumption may not always hold. As the MR voxels do not align with the 0.5 mm histology grid, the total number of specifically-stained (i.e. segmented) pixels were pooled and re-normalised for each MR voxel, minimising interpolation effects. Pixels in the SAF maps with values $< 5^{th}$ percentile were identified as non-tissue pixels and discarded. Other outliers were identified using a Huber influence function (tuning coefficient= 2.5), excluding data points with weights < 0.75 [139]. We pooled voxelwise data across regions and brains for several linear model analyses between MRI and SAF:

- **Simple correlation:** We correlated each pair of MR (FA, MD, RD, AD, R_2^*, R_1) and SAF (PLP, SMI312, Iba1, CD68) parameters.

- **Partial correlation:** We estimated the unique variance of each MR parameter that is explained by a given stain's SAF, accounting for other stains. Subject ID was used as a covariate to account for between-subject confounds.

- **Multiple linear regression:** We model each MR parameter as a linear combination of all stains (explanatory variables) and the subject ID (confounding variable). We computed each variable's relative importance measure [140], i.e. the averaged relative contribution of each variable in explaining the variance of the MR parameter after it is added to the model.

As a proof-of-concept, we performed voxelwise analyses on 2 subjects from the multiple-region dataset (1 x CTL, subject 1, 16 slides; 1 x ALS, subject 2, 16 slides). Analyses were done using WM+GM voxels or WM voxels only, where the latter demonstrates sensitivity to subtle microstructural changes rather than gross WM/GM tissue differences.

4.3.4 Application to multiple subjects for MRI

This pipeline can be rapidly applied across many subjects. We demonstrate this by applying the workflow to 41 PLP slides from 10 additional subjects. We correlated MRI with PLP only, as co-registration between other stains and MRI data was a work-in-progress. We compared the 10 subjects' output with the 2 subjects previously analysed. Subject ID was modelled as a covariate.

4.4 Results

4.4.1 Co-registration of MRI and histology

Figures 4.2 and 4.3 show good alignment of the tissue mask (green contour) and WM/GM interface (red contour) for subjects 1 and 2. Of the remaining subjects, 10 had good-quality registrations (Figure 4.4) and 3 were excluded from subsequent analysis due to substantial misalignment (Figure 4.13). Additional quantitative evaluation of the dataset registration can be found in [128].

4.4.2 Voxelwise MRI-SAF analyses

A total of 32 IHC slides from different regions in subjects 1 (Figure 4.2) and 2 (Figure 4.3) were mapped onto MRI data. For each MR parameter, up to 3% of voxels were classified as outliers and removed.

Simple correlation

Simple correlation was used to relate each MRI-SAF pair (Figure 4.5). While correlations with Iba1 appear low ($|r| = 0.035 - 0.28$), CD68 correlated well with FA ($r = 0.56$) and MD ($r = -0.39$). The scatterplots also suggest nonlinear trends for FA with PLP and SMI312. Similar analysis of WM only is shown in

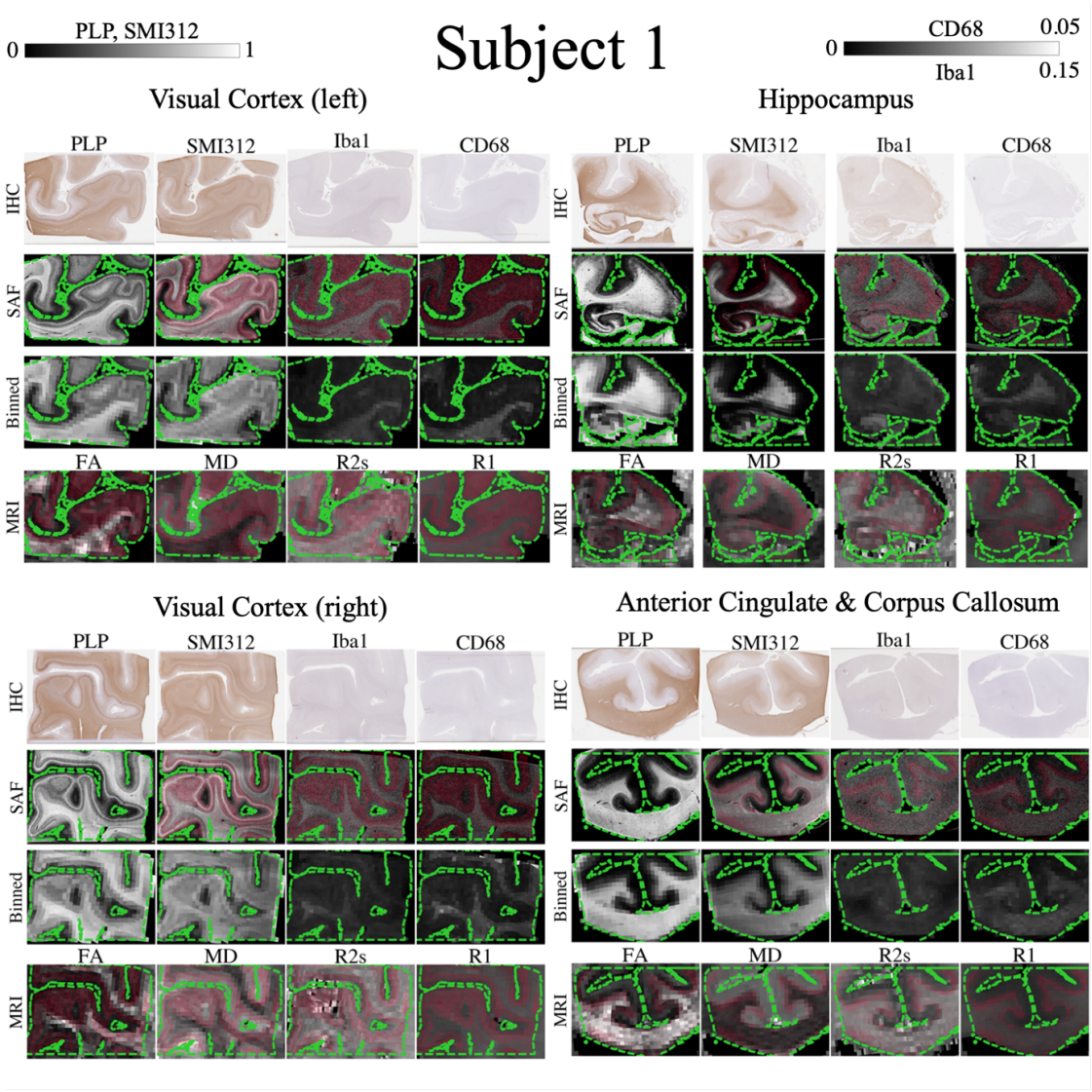

Figure 4.2: Registration evaluation for all brain regions in subject 1. In each brain region, contours of the tissue mask (green dashed) are overlaid on the co-registered SAF maps at high resolution (first row, 1 pixel here represents SAF calculated in a $16 \times 16 \mu m^2$ patch), SAF maps matching MRI resolution (second row) and MR parameter maps (third row). The white and grey matter interface is shown in red. The tissue boundaries are closely aligned and the high registration accuracy enables us to perform meaningful voxelwise MRI-IHC correlations.

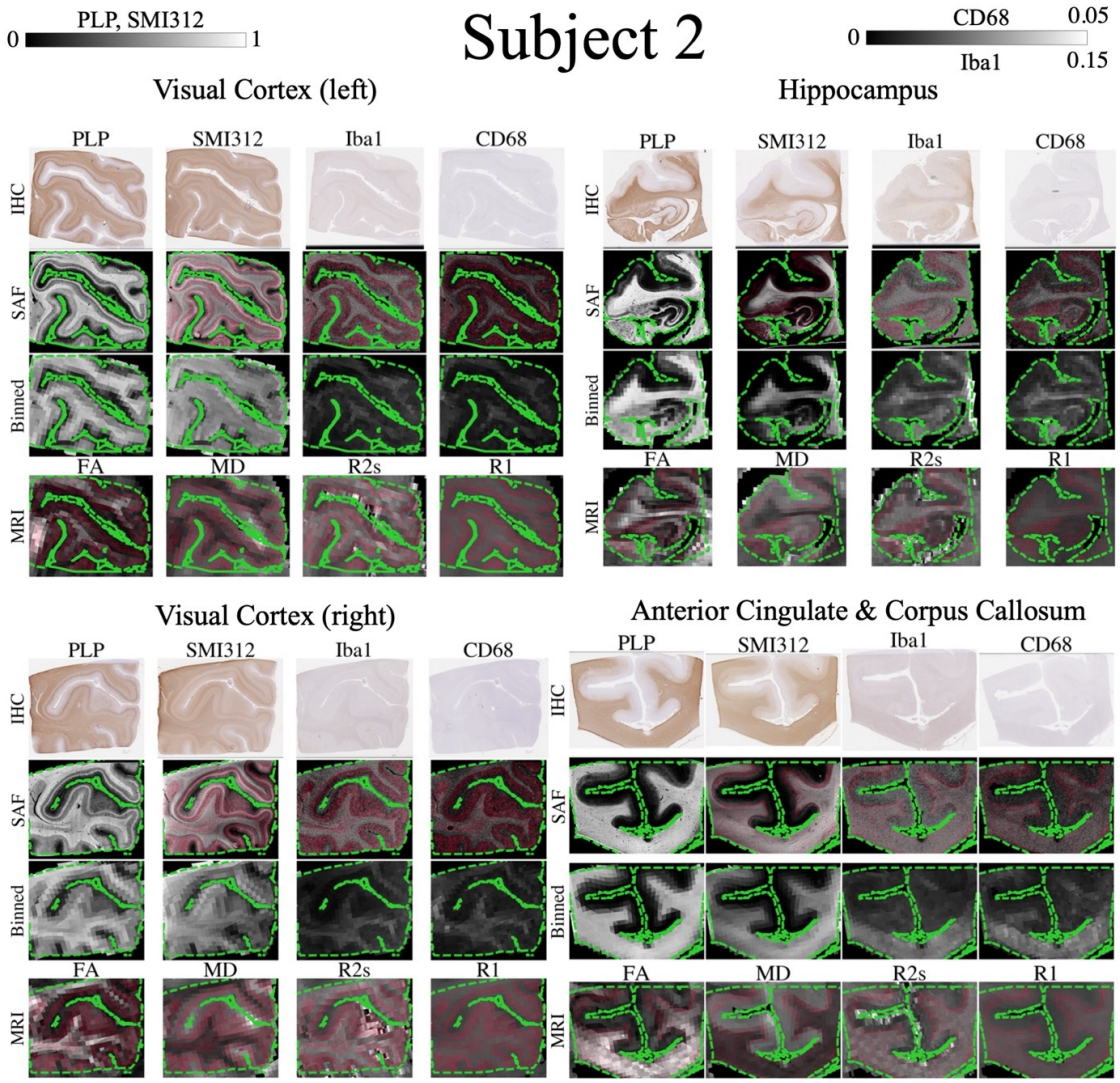

Figure 4.3: Registration evaluation for all brain regions in subject 2. Results are displayed as described in Figure 4.2. Again, we see the close alignment of tissue borders and contours representing WM/GM contrast.

Figure 4.6, where FA shows a strong correlation with CD68 ($r = 0.33$) and R_2^* with Iba1 ($r = -0.30$). Scatterplots with AD and RD are shown in Appendix Figure 4.10. In WM+GM, AD and RD correlated negatively with all stains. When analysing the WM only, notable results include the correlation of AD with Iba1 ($r = 0.27$) and RD with CD68 ($r = -0.21$).

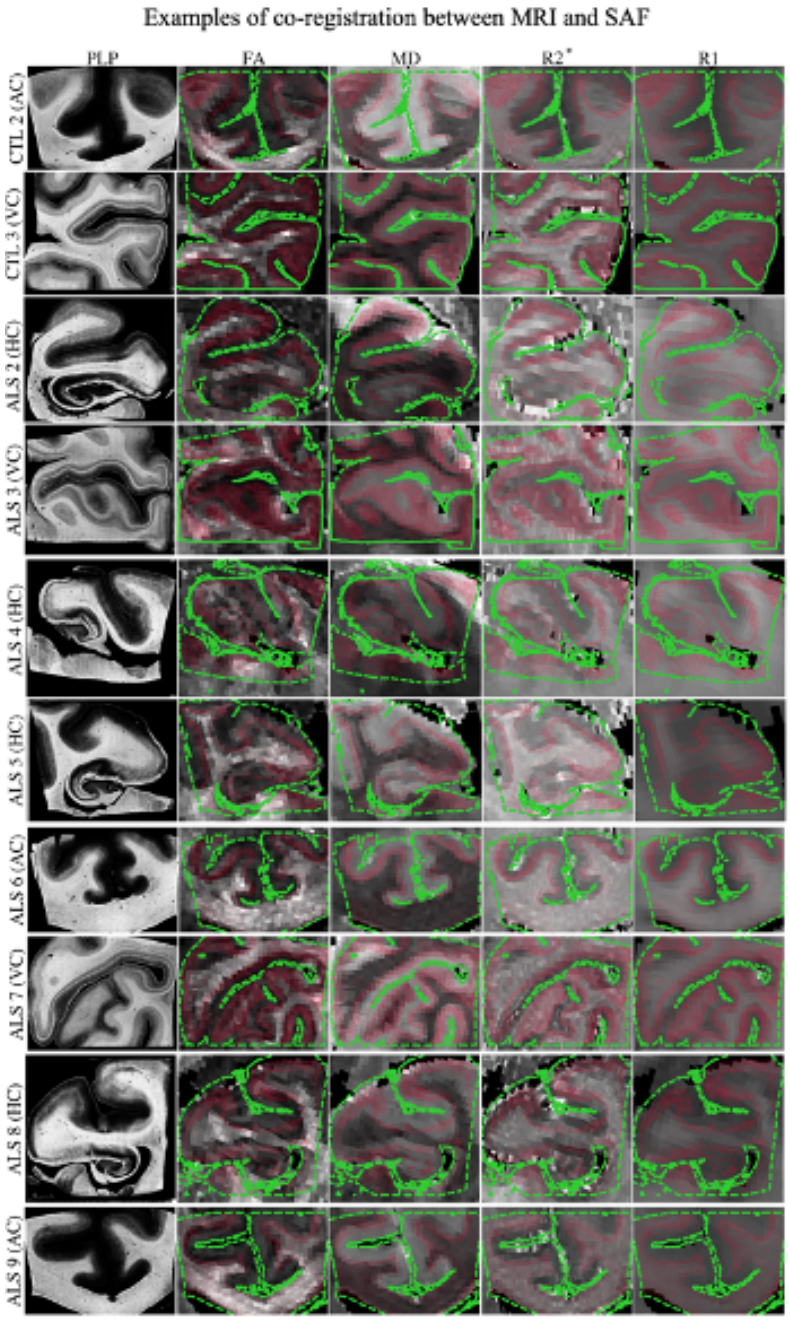

Figure 4.4: Registration evaluation for example brain regions extracted from 10 additional subjects (2 CTL, 10 ALS) (rows). In each brain region, the contours of the tissue mask (green dashed) are overlaid on the co-registered MR parameter maps (second to fifth columns). The white and grey matter interface is shown in red. The tissue boundaries are closely aligned and the high registration accuracy enables us to perform meaningful voxelwise MRI-IHC correlations.

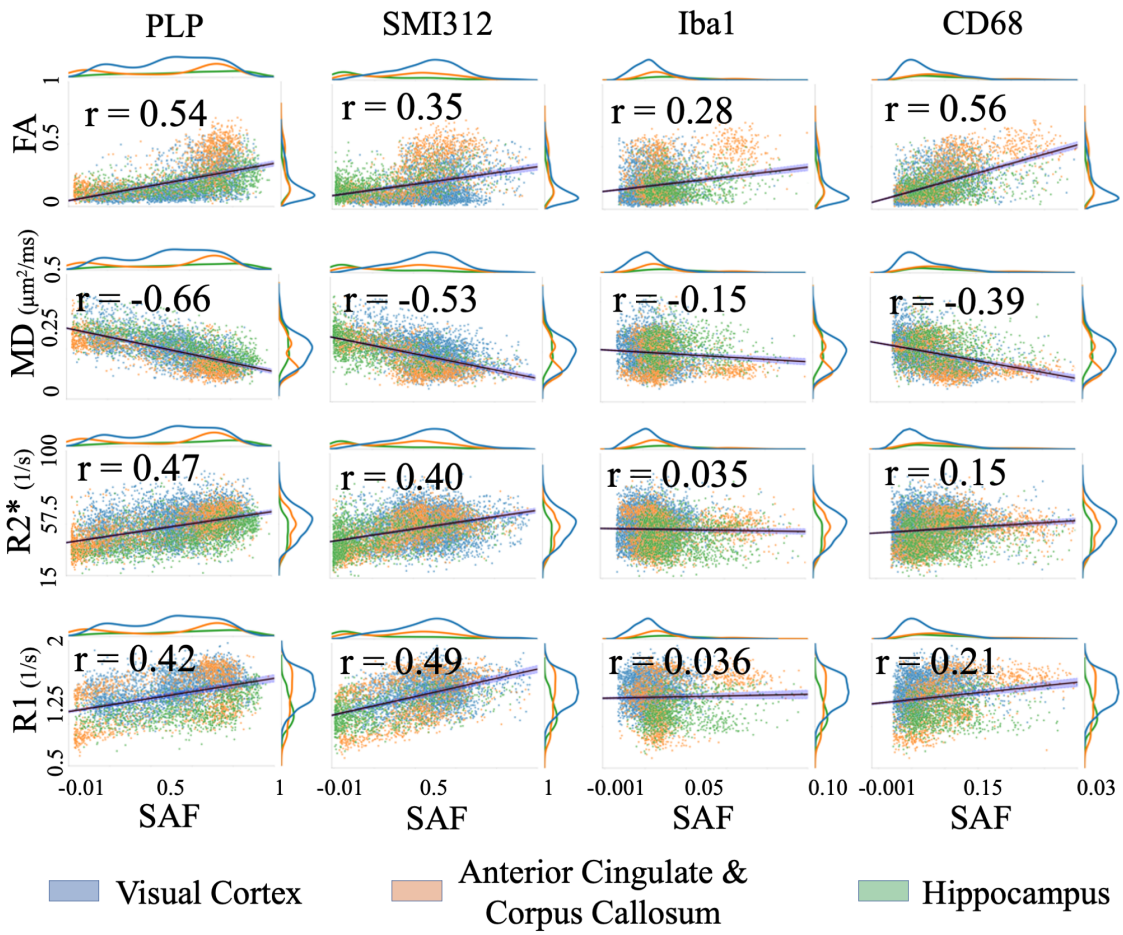

Figure 4.5: Correlating MR parameters (DTI FA, MD, R_2^* and R_1) with IHC SAF (WM+GM). The line of best fit (black line) and corresponding Pearson correlation coefficients, r, are overlaid. Confidence intervals (99%) are shown in blue shade. The visual cortex (blue), anterior cingulate (orange) and hippocampus (green) provide good dynamic range for the MR parameters and SAFs.

Partial correlation

For each stain, correlations were calculated after regressing out one other stain or all other stains as covariates. We show correlation coefficients when including all voxels (WM+GM) (Figure 4.7A), or WM only (Figure 4.7B). Similar data for AD and RD are shown in Appendix Figure 4.11.

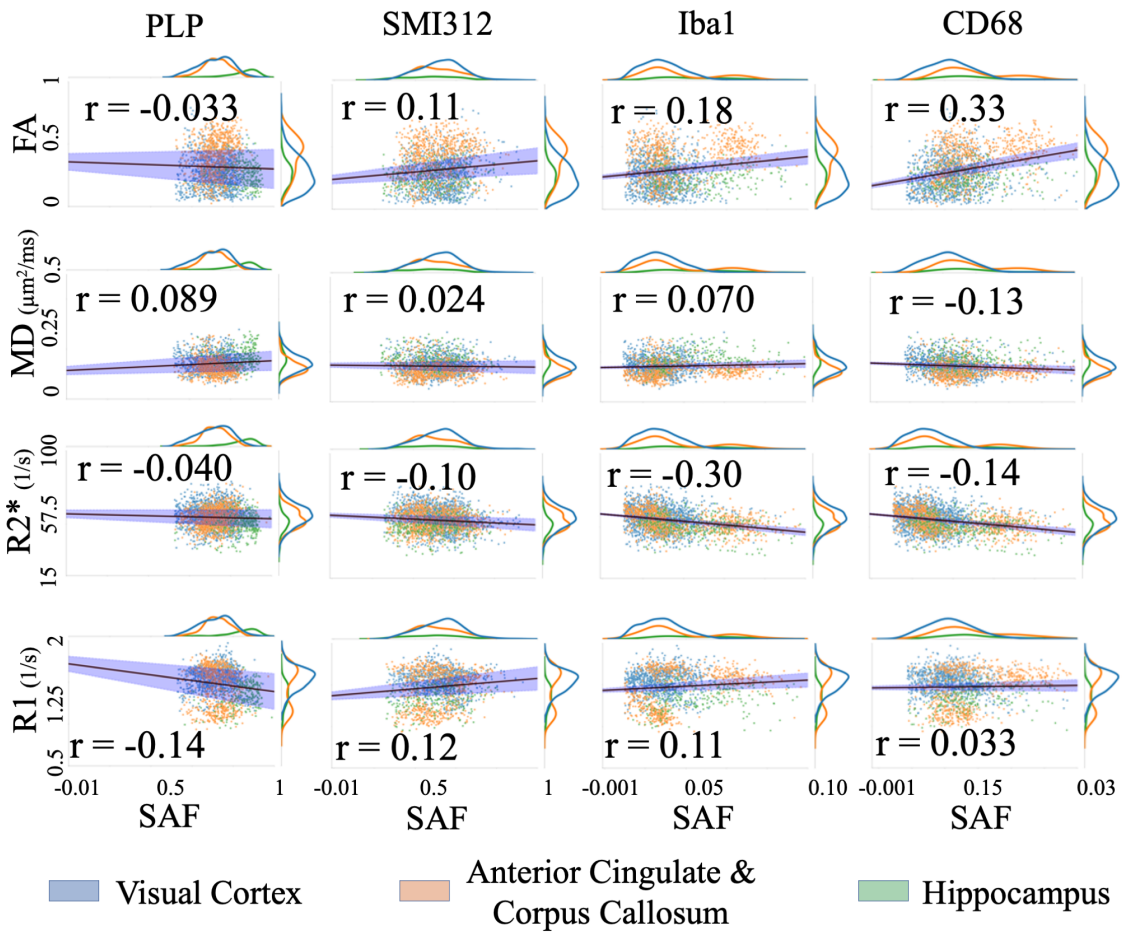

Figure 4.6: Correlating MR parameters (DTI FA, MD, R_2^*, and R_1) with IHC SAF in WM only. The line of best fit (black line) and corresponding Pearson correlation coefficients, r, are overlaid, along with the confidence intervals (blue shade). PLP (myelin); SMI312 (neurofilaments); Iba1 (microglia); CD68 (activated microglia).

WM and GM When accounting for all other stains (Figures 4.7A and 4.11A, bottom rows), FA is best explained by CD68 ($r = 0.38$), MD/AD/RD/R_2^* by PLP ($r = -0.42/r = -0.65/r = -0.68/r = 0.30$) and R_1 by SMI312 ($r = 0.36$). We observed two main results: the shared explained variance between PLP (myelin) and SMI312 (neurofilaments), and between Iba1 (all microglia) and CD68 (activated microglia).

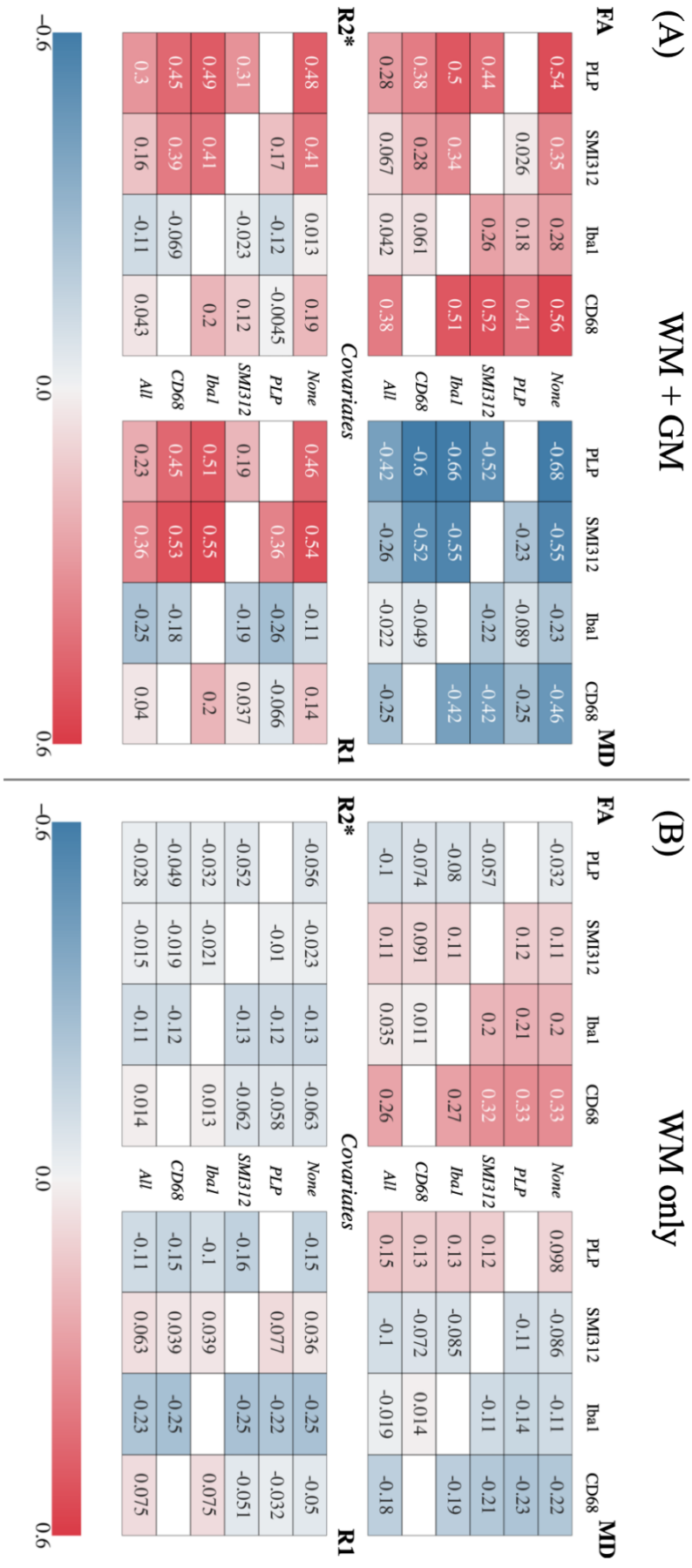
(A)
WM + GM
FA
PLP SMI312 Iba1 CD68
0.54 0.35 0.28 0.56
0.026 0.18 0.41
0.44 0.26 0.52
0.5 0.34 0.51
0.38 0.28 0.061
0.28 0.067 0.042 0.38
R2*
PLP SMI312 Iba1 CD68
0.48 0.41 0.013 0.19
0.17 -0.12 -0.0045
0.31 -0.023 0.12
0.49 0.41 0.2
0.45 0.39 -0.069
0.3 0.16 -0.11 0.043
MD
PLP SMI312 Iba1 CD68
-0.68 -0.55 -0.23 -0.46
-0.23 -0.089 -0.25
-0.52 -0.22 -0.42
-0.66 -0.55 -0.42
-0.6 -0.52 -0.049
-0.42 -0.26 -0.022 -0.25
R1
PLP SMI312 Iba1 CD68
0.46 0.54 -0.11 0.14
0.36 -0.26 -0.066
0.19 -0.19 0.037
0.51 0.55 0.2
0.45 0.53 -0.18
0.23 0.36 -0.25 0.04
Covariates
None
PLP
SMI312
Iba1
CD68
All
(B)
WM only
FA
PLP SMI312 Iba1 CD68
-0.032 0.11 0.2 0.33
0.12 0.21 0.33
-0.057 0.2 0.32
-0.08 0.11 0.27
-0.074 0.091 0.011
-0.1 0.11 0.035 0.26
R2*
PLP SMI312 Iba1 CD68
-0.056 -0.023 -0.13 -0.063
-0.01 -0.12 -0.058
-0.052 -0.13 -0.062
-0.032 -0.021 0.013
-0.049 -0.019 -0.12
-0.028 -0.015 -0.11 0.014
MD
PLP SMI312 Iba1 CD68
0.098 -0.086 -0.11 -0.22
-0.11 -0.14 -0.23
0.12 -0.11 -0.21
0.13 -0.085 -0.19
0.13 -0.072 0.014
0.15 -0.1 -0.019 -0.18
R1
PLP SMI312 Iba1 CD68
-0.15 0.036 -0.25 -0.05
0.077 -0.22 -0.032
-0.16 -0.25 -0.051
-0.1 0.039 0.075
-0.15 0.039 -0.25
-0.11 0.063 -0.23 0.075
Covariates
None
PLP
SMI312
Iba1
CD68
All
−0.6
0.0
0.6

Figure 4.7

Figure 4.7: Partial correlation analysis between MR parameters (FA, MD, R_2^* and R_1) and IHC stains for (A) both WM+GM voxels and (B) for WM only. In each quadrant for either (A) or (B), the top row ("None") gives the correlation coefficients when accounting for subject ID only. The middle rows give the partial correlation coefficient controlling for one of the other stains and subject ID (italicised labels in the second to fifth rows). The bottom row ("All") gives the partial correlation coefficient controlling for all stains and subject ID. Note that correlations between FA/MD with CD68 remain relatively high, even after accounting for all other stains. PLP (myelin); SMI312 (neurofilaments); Iba1 (microglia); CD68 (activated microglia).

First, the correlation coefficient between FA and SMI312 is greatly reduced after accounting for PLP ($r = 0.35$ to 0.026), whilst the correlation coefficient between FA and PLP is marginally reduced after accounting for SMI312 ($r = 0.54$ to 0.44). Similar effects are observed between MD and PLP/SMI312, and between R_2^* and PLP/SMI312. The opposite effect is seen in R_1: the correlation coefficient between R_1 and PLP decreases significantly when covarying for SMI312 ($r = 0.46$ to 0.19), but the correlation coefficient between R_1 and SMI312 is marginally reduced when accounting for PLP ($r = 0.54$ to 0.36). Second, we saw that the high correlations of FA/RD with CD68 marginally decrease after accounting for Iba1 ($r_{FA} = 0.56$ to 0.5; $r_{RD} = -0.50$ to -0.45). Conversely, the apparent correlations with Iba1 are minimal after accounting for CD68 ($r_{FA} = 0.28$ to 0.061; $r_{RD} = -0.24$ to -0.029). We note similar trends for correlations of MD with CD68/Iba1.

WM only Figures 4.7B and 4.11B show the same analysis for voxels found in the WM only. When accounting for all other stains, FA/MD/RD is best explained by CD68 ($r = 0.26/r = -0.18/r = -0.22$), AD by PLP ($r = 0.10$), R_2^*/R_1 by Iba1 ($r = -0.11/r = -0.23$). When compared to our previous results for WM+GM voxels, the correlation coefficient between most MR parameters and PLP/SMI312 is greatly reduced and/or close to zero. This behaviour is not seen for CD68 and Iba1. In WM, CD68 explains the most unique variance in FA and RD. Notably, these correlations remain relatively unchanged when accounting for other stains ($r_{FA} = 0.33$ to 0.26; $r_{RD} = -0.29$ to -0.22). Similar behaviour is observed when relating CD68 with MD, and Iba1 with R_1/R_2^*.

Multiple linear regression

We show the regression and fitted correlation coefficients (i.e. square root of the coefficient of determination) when including voxels from WM and GM, or WM only (Figures 4.8A, 4.12A). Using multiple stains better explains the variance in MR parameters than individual stains. We also show the relative importance of each predictor (Figures 4.8B, 4.12B). The subject predictor had the highest relative importance in predicting R_1 in all voxels, and MD/R_2^*/R_1 in WM voxels only. This implies that between-subject confounds substantially influence MRI parameters. In postmortem data, these confounds may be different postmortem intervals and fixation times between subjects.

4.4.3 Application to multiple subjects for MRI-PLP

Similar regression coefficients were seen for the larger group (n = 10, Figure 4.9 right) compared to the original analysis (n = 2, Figure 4.9 left), with the estimated effect (β) being highly consistent for FA, MD, and R_2^*, but less consistent for R_1. The lower β for R_1 may be due to the large variation in R_1 values.

4.5 Discussion

We have described a workflow that facilitates efficient MRI-microscopy analyses across multiple subjects, brain regions and stains. Here, we combine our high-throughput, quantitative SAF pipeline with high-quality MRI-microscopy co-registration, to relate slides stained for myelin (PLP), neurofilaments (SMI312), microglia (Iba1) and activated microglia (CD68) to MR multiple parameters (FA, MD, RD, AD, R_2^*, R_1).

Our approach facilitates voxelwise MRI-SAF analyses that inspire more confidence than ROI-based analyses, which are biased by the choice of ROI and/or dilute

All voxels/WM only

(A) Multiple regression offset and slopes

	Offset	PLP	SMI312	Iba1	CD68	Subject	r_{fit}
FA	-0.00142*/ 0.255	0.173/ -0.173	0.0429/ 0.144	0.252/ 0.410*	10.5/ 8.81	-0.0112/ -0.0247	0.645/ 0.353
MD [µm²/ms]	0.286/ 0.118	-0.112/ 0.0610	-0.070/ -0.0323	-0.0629*/ -0.0531*	-2.55/ -1.40	0.0366/ 0.0310	0.745/ 0.429
R2* [1/s]	39.2/ 61.2	16.5/ -2.22*	9.04/ -0.889*	-61.2/ -55.2	80.7/ 19.6*	-3.73/ -5.54	0.536/ 0.455
R1 [1/s]	1.04/ 1.52	0.220/ -0.217	0.382/ 0.0878	-2.48/ -2.71	1.34/ 1.89	0.234/ 0.268	0.710/ 0.637

*not significant (p>0.05)

(B) Relative Importance [%]

	PLP	SMI312	Iba1	CD68	Subject
FA	36.0/4.32	11.9/8.75	7.04/15.1	44.5/69.2	0.55/2.66
MD	45.0/6.43	25.7/2.40	1.69/4.99	14.5/16.2	13.1/70.0
R2*	51.3/0.47	30.1/1.97	2.90/22.6	3.86/3.62	11.8/71.3
R1	18.7/4.54	30.6/2.39	3.15/5.88	2.93/0.443	44.6/86.8

Figure 4.8: Multiple linear regression predicting MR parameters using multiple IHC stains. Values are computed from WM+GM, or from WM only (format of results: "all voxels/WM only"). A "subject" variable was also included to account for confounds such as postmortem interval and age effects. As the predictors are unitless, all offsets and regression slopes are given in units of MR parameters. A: The regression coefficients and correlation coefficients r_{fit}. B: The relative importance of each stain describes the amount of variance it can explain in an MR parameter, averaged over all permutations of multiple regressions that include the specific stain. Values are normalised across stains to get a unit percentage.

localised effects-of-interest. Further, most studies perform simple correlations with only a single or a few histological markers [102], [106], [141]. We extend this analysis to partial correlation and multiple linear regression relating multimodal MRI to multiple IHC stains. This presents two key benefits. First, partial correlations can demonstrate sensitivity to specific microstructural changes such as microglial activation (changes in CD68 but not Iba1), demyelination (changes in PLP but not SMI312) and axonal loss (simultaneous changes in SMI312 and PLP). This may aid with disease diagnosis and/or staging. Here, our pipeline is applied to a dataset

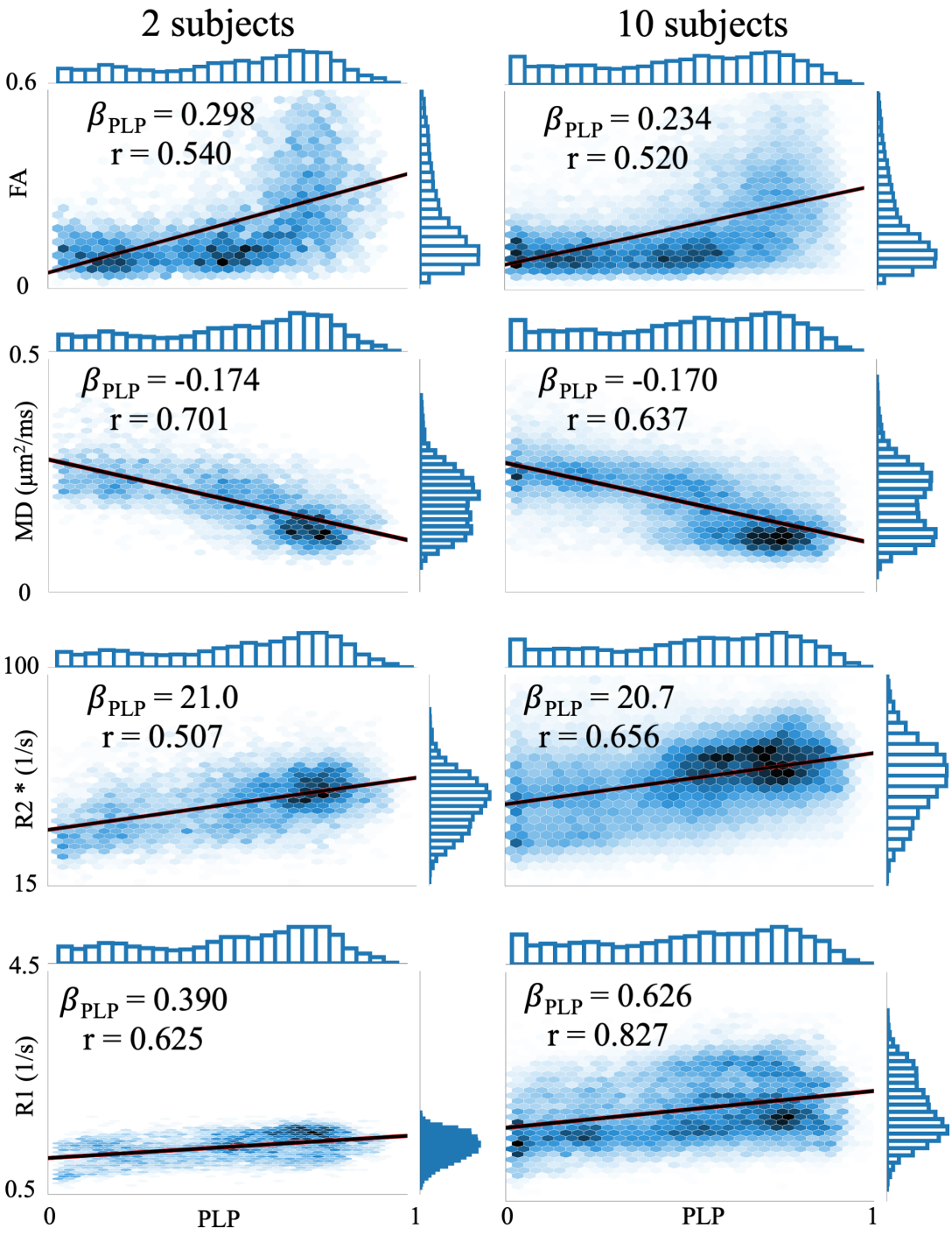

Figure 4.9: Density plots showing the relationship of different MR parameters (rows) with PLP (myelin) for both white and gray matter voxels. We compare the MRI-PLP regression coefficient (β_{PLP}) derived from analysis across many subjects (CTL 2-3 & ALS 2-9; right column) with analysis across 2 subjects (CTL 1 & ALS 1; left column). The effect size, β_{PLP}, is highly consistent between the two datasets for FA, MD, and R_2^*, but less so for R_1.

that was specifically acquired for future investigation into ALS neuropathology, as motivated in our previous publication that presented the study design [96]. Currently, we refrain from making any strong conclusions with respect to ALS pathology since our MRI-SAF results are from only two subjects, where co-registration for other subjects was still a work-in-progress. However, future work will draw on MRI-SAF results from the entire multi-subject dataset to provide an in-depth evaluation of the cellular bases of MRI in the context of ALS neuropathology. Second, both the partial correlation and multiple linear regression analyses can account for confound variables, which may otherwise influence our results. Subject-specific confounds contributed to significant variation in R_1/MD/R_2^* (relative importance in Figure 5.4). This may be due to different postmortem intervals (3 versus 2 days) and/or fixation times (45 versus 139 days), both of which are known to influence MR parameters (R_1, R_2^*: [142]–[144]; MD: [143], [144]). Notably, FA-microstructure mappings were independent of subject confounds, given that postmortem tissue exhibits similar patterns of FA when pooling voxels from WM+GM [145]–[147]. A more in-depth analysis of these confounds (e.g. whether postmortem interval or fixation time is the primary driver of between-subject variance) is left for future work within the larger multiple-subject dataset.

4.5.1 Voxelwise MRI-SAF analyses

Our correlation results agree with previous studies for myelin [22], [105], [106], [109] and neurofilaments [129]. Activated microglia correlates positively with FA and negatively with MD/RD, similar to that reported in the human spinal cord [129].

Myelin and neurofilaments

Our partial correlations for PLP (myelin) and SMI312 (neurofilaments) demonstrate pitfalls in performing pairwise MRI-IHC correlations without controlling for other tissue features. Our simple correlations from WM+GM voxels reveal an

apparent relationship between neurofilaments and FA, MD, R_2^*; however, our partial correlation results that account for myelin find no such relationship. Thus, one may erroneously conclude from simple correlations that anisotropy is affected by myelin and neurofilament (axons, dendrites) load, whereas our partial correlations show that anisotropy is primarily related to myelin density, with no unique variance attributed to dendritic load. As we do not account for microstructure orientation dispersion—where the orientational coherence of axons and dendrites may drive variations in diffusion anisotropy [10]—we cannot determine whether the FA-PLP correlation reflects a direct relationship with myelin density or an indirect relationship with microstructure dispersion. These results imply that the portion of microstructure dispersion that affects FA is unrelated to dendritic load; if it were, we expect a high correlation between FA and dendritic load, with microstructure dispersion being the main confound in driving this relationship. This is something we hope to investigate further in the future. MD and R_2^* are similarly affected by myelin load, though some specificity to unmyelinated axons and/or dendrites remains.

Conversely, SMI312 explains unique variance in R_1, even after accounting for PLP. This implies that R_1 is sensitive to neurites in general, rather than myelin alone. This is noteworthy, given the studies correlating myelin with R_1 [31], [45], [148] without considering the impact of unmyelinated axons and/or dendrites.

Finally, in WM only, all PLP/SMI312 associations are reduced, suggesting WM/GM contrast as the primary driver. Taken together, our results may explain the wide range of MRI-myelin correlation coefficients reported in two reviews (Figures 4, 5 in [22]; Figure 4 in [105]).

Microglia

Our results suggest a relationship between CD68 (activated microglia, a biomarker for neuroinflammation [94], [95]) and FA/MD/RD, after accounting for all other stains (e.g. demyelination, axonal loss or general microglia infiltration). This

relationship is present when considering all voxels (WM+GM) and WM only, demonstrating MR sensitivity to subtle microstructural changes rather than gross WM/GM differences. This result may be linked to microstructural changes in response to neuroinflammation that are unaccounted for in our histology metrics, or non-trivial changes in "activated" versus "non-activated" microglia morphology. For example, activated microglia often have more retracted, thicker processes and different soma sizes and shapes compared to their non-activated counterparts [149]. This may contribute to increased restriction and/or hinderance of diffusion in the extra-axonal space, leading to an observed reduction in MD and RD, and a resultant increase in diffusion anisotropy (FA).

The inverse relationship between MD/RD and microglial activation agrees with results previously reported in several animal studies [11]. Guglielmetti et al. used the cuprizone model to measure the temporal evolution of DTI metrics following acute inflammatory demyelination and subsequent remyelination. Interestingly, they also reported a decrease in MD and RD within the first 3 weeks of cuprizone intoxication, implying increased membrane barriers in the extra-cellular space due to infiltration and proliferation of activated microglia [150]. In a traumatic brain injury animal model, Zhuo et al. reported an immediate increase in diffusion restriction following injury, and linked it to elevated reactive astrogliosis [151]. Overall, our results align with the growing body of literature from animal studies indicating diffusion MRI's sensitivity to the initial cellular processes characteristic of neuroinflammation, such as microglial activation and astrogliosis.

While human studies typically report decreased FA in diseases associated with neuroinflammation [152], [153], they do not measure microglial activation and generally attribute the changes in FA to WM damage. This is mainly due to the competing mechanisms between demyelination and/or axonal loss (i.e. increased MD, RD) and glial activation and/or proliferation (i.e. decreased MD, RD), and the inability to measure inflammatory processes at precise time points. Future research into measuring microglial activation using MRI will benefit from the development of

advanced biophysical models [64], [74], [154], [155] that can simultaneously account for multiple changes in the microstructure (demyelination, axonal damage, microglial infiltration, exchange effects etc) and provide superior specificity to the DTI metrics.

Activated microglia is known to colocalise with iron [156], [157] and correlate positively with R_1 and R_2^* [29], [49], [108], [147]. However, CD68 is found to weakly correlate with R_1 and R_2^* after accounting for subject-specific confounds (Figure 4.7, Table 4.8). Our results suggest a negative correlation between non-activated microglia (Iba1 after accounting for CD68) and R_1/R_2^*. Future studies may incorporate iron-stained IHC to elucidate the contributions of iron to relaxometry metrics.

4.6 Limitations

There are limitations to this MRI-microscopy analysis. First, we use SAF—a semi-quantitative metric defined via a segmentation threshold—to quantify MRI-microscopy relationships. Depending on how the SAF threshold is derived, this may result in subtly different SAF maps. Further, SAF may not scale linearly with protein density, as anything above the stain threshold was considered a positive stain. While our results show key trends between MR parameters and proteins, the exact MRI-SAF slopes may not be directly comparable to other studies using different thresholding methods or stain densities. Here, a key advantage of our data-driven SAF is that it is less sensitive to non-biological staining variations both within and between slides, which if unaccounted for, can bias stain density metrics. Finally, we do not incorporate other microscopy metrics that may relate to MRI. For example, we do not include the fibre orientation dispersion and microglial cell morphology, which may explain variance in FA or other MR parameters.

4.7 Conclusion

We implemented an end-to-end MRI-microscopy workflow that combined high-quality MRI-IHC co-registrations with the SAF pipeline to perform voxelwise comparisons between multimodal MRI- and IHC-derived parameters. The pipeline was applied to co-registered MRI and IHC data from postmortem human brains. Our results emphasise the need to simultaneously analyse multiple stains when validating MRI, so as to avoid misleading inference due to the spatial covariance of multiple microstructural features. Interestingly, we found several diffusion-weighted metrics' sensitivity to activated microglia–a biomarker of neuroinflammation. This result held after accounting for spatial covariance of other stains (myelin, neurofilaments and non-activated microglia), suggesting MR specificity to aspects of neuroinflammation related to microglial activation, irrespective of other microstructural changes (axonal loss, demyelination or general microglia infiltration). Finally, subject ID was found to be the strongest predictor of some MR parameters, highlighting the need to consider tissue processing confounds when comparing postmortem MRI across subjects. Together, our results demonstrate the MRI-microscopy workflow as a valuable approach for IHC analyses and future investigations relating MRI to disease pathology.

4.8 Acknowledgements and contributions

I would like to extend my genuine appreciation to Istvan N. Huszar for co-registering the MRI and microscopy data. I am again deeply grateful to the donors and benefactors of the Oxford Brain Bank who kindly provided all human tissues for this study. I was responsible for conceiving the study design, implementing the MRI-microscopy workflow, conducting correlation and regression analyses, and drafting the manuscript.

4.9 Appendix

4.9.1 Correlating other DTI metrics with IHC

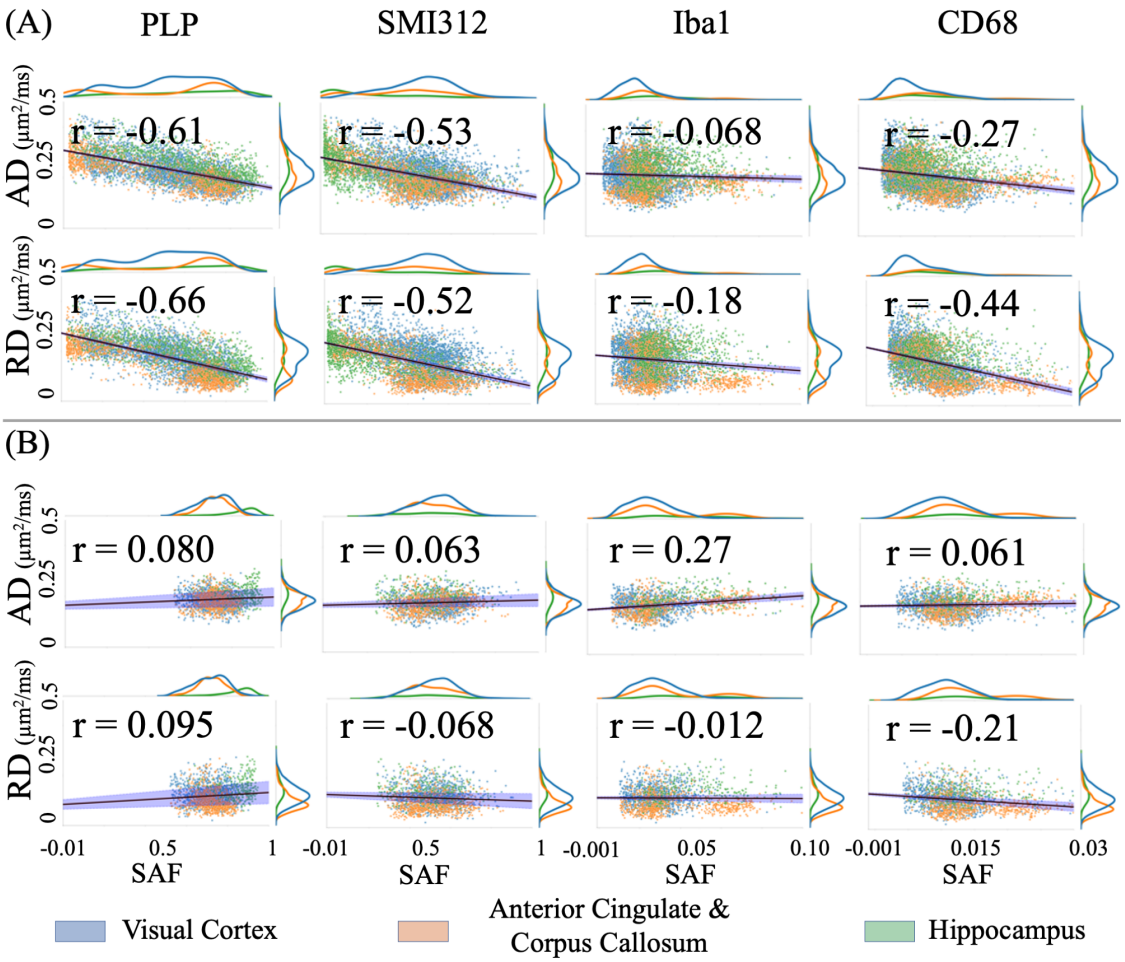

Figure 4.10: Correlating other DTI-derived parameters (AD, RD) with IHC SAF. This is done with all tissue voxels (A), and with voxels found the tissue's WM only (B). Data is interpreted similarly to Figure 4.6.

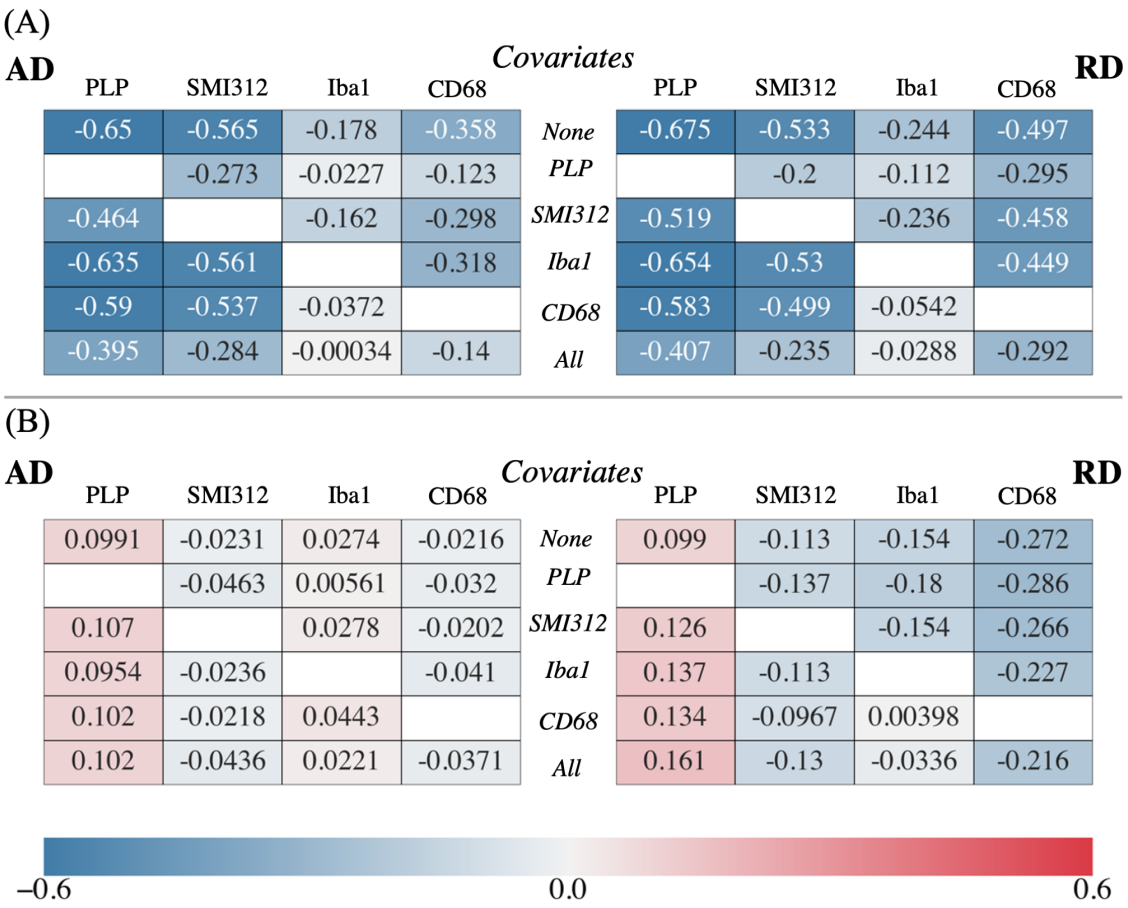

Figure 4.11: Partial correlation analysis between other DTI-derived parameters (AD, RD) and IHC stains for (A) both white and gray matter voxels and (B) for white matter voxels only. Each quadrant in either (A) or (B) is interpreted similarly to Figure 4.7. PLP (myelin); SMI312 (neurofilaments); Iba1 (microglia); CD68 (activated microglia).

All voxels/WM only

(A) Multiple regression offset and slopes

	Offset	PLP	SMI312	Iba1	CD68	Subject	r_{fit}
AD [$\mu m^2/ms$]	0.302/ 0.149	-0.0988/ 0.0374	-0.0738/ -0.0120*	-0.000839*/ 0.0506*	-1.22/ -0.208*	0.0413/ 0.0359	0.729/ 0.526
RD [$\mu m^2/ms$]	0.279/ 0.100	-0.118/ 0.0789	-0.0685/ -0.0476	-0.0767/ -0.109*	-3.30/ -2.03	0.0345/ 0.0294	0.740/ 0.404

*not significant ($p>0.05$)

(B) Relative Importance [%]

	PLP	SMI312	Iba1	CD68	Subject
AD	42.2/2.11	28.2/0.685	0.844/12.7	6.83/1.03	21.9/83.4
RD	45.1/9.28	24.1/5.64	2.29/4.64	18.7/31.5	9.82/48.9

Figure 4.12: Multiple linear regression predicting RD and MD using multiple IHC stains. Values are computed from all tissue voxels, or from voxels located in the tissue's WM only. The table is interpreted similarly to Figure 4.8

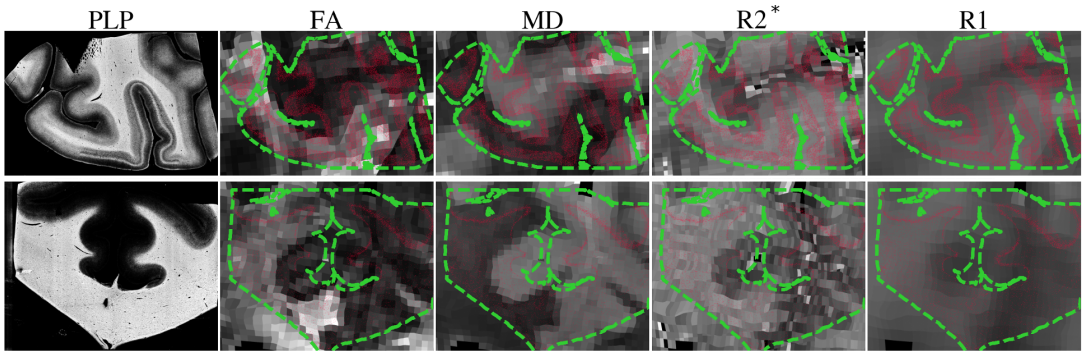

Figure 4.13: Examples of bad MRI-IHC co-registrations that were excluded from the analysis. This figure is interpreted similarly to Figure 4.4. Contours of the tissue mask (green dashed) generated from the PLP slide were observed to be completely misaligned with the MRI-derived parameter maps.

5

Parameter inference using continuous change in degenerate biophysical diffusion models

Contents

Foreword

Biophysical modelling of diffusion MRI (dMRI) may elucidate key microstructural features. However, most models include many input parameters, making simultaneous estimations of all parameters ill-posed. To overcome this, the recently published Bayesian framework EstimatioN for CHange (BENCH) characterises which parameter changes are consistent with measured signal variations, rather than inferring the actual parameters from a single measurement/sample. BENCH has been previously applied to identify which biophysical parameters could explain group-wise signal differences (e.g. patients vs. controls). Here, we adapted BENCH to interpret changes in continuous variables ("continuous BENCH"). We validate continuous BENCH using synthetic dMRI data from numerical simulations. We then applied it to ex-vivo macaque brain data to estimate which biophysical model parameter best explains the measured change in dMRI signal, as described by microscopy glial cell soma and axon metrics derived from the same brain.

Publications relating to this work

Conference proceedings:

Kor DZL, Rafipoor H, Cottaar M, Miller KL*, Howard AFD* "Parameter inference using continuous change in degenerate biophysical diffusion models", Proceedings of the 31st Annual Meeting of the ISMRM, Toronto, 2023.

5.1 Introduction

Diffusion MRI (dMRI) provides sensitivity to the microstructural details in the brain. However, dMRI signals are inherently non-specific—changes in different microstructure may produce the same change in dMRI signal. Hence, the interpretation of exact micrometre-scale features for a signal decay measured in a millimetre-scale MRI voxel is challenging, if not ill-posed.

To address this, biophysical diffusion models help separate dMRI signals into biologically meaningful tissue parameters (termed "biophysical parameters"). When modelling the brain WM microstructure, the standard model (c.f Section 2.3.3) is commonly used. The standard model can be extended by adding more compartments (e.g. a sphere compartment being used to describe signal contributions from cell soma) to explain the complex microstructure more accurately. However, this requires the estimation of more parameters. When fitted to dMRI data commonly acquired using a linear diffusion encoding protocol (e.g. HARDI), this often results in a solution degeneracy. To overcome this degeneracy and perform a reliable fit, one can make assumptions about the tissue microstructure to constrain the standard model (e.g. NODDI [64]). However, this introduces significant biases and is known to be an oversimplification [69].

Here, we aim to circumvent model fitting altogether by using the Bayesian EstimatioN of CHange (BENCH) framework. BENCH achieves this by characterising the effect of parameter changes on the dMRI signal, instead of estimating the parameters themselves. Briefly, BENCH uses a generative model (M) to train "change models" where, for a set of input biophysical parameters ($\boldsymbol{\nu}$) we generate a dMRI signal ($\mathbf{S}$), and the change in a dMRI signal induced by a small change in the different biophysical model parameters ($\frac{\partial \mathbf{S}}{\partial \boldsymbol{\nu}}$; also termed "change vector"). Note that $\mathbf{S}$ represents the generated dMRI signal, while $\mathbf{y}$ is the measured dMRI signal. The central concept is that the change models' outputs can be compared with a measured variation in a dMRI signal $\mathbf{y}$ in a dataset to infer the likelihood that a change in

a biophysical model parameter explains the measured signal variation. Crucially, the degenerate model does not need to be inverted to infer parametric change, facilitating the use of more complex and otherwise inaccessible biophysical models.

Previously, BENCH was used to infer microstructural differences between two categorical groups (patients versus controls). Here, we investigate which biophysical model parameters explain dMRI signal variation along an axis defined by different microscopy metrics derived from histologically stained sections. To accomplish this, we need to infer change that corresponds to a continuous, rather than a categorical, variable.

Specifically, we ask this central question: does dMRI signal measured from the WM possess sensitivity to variability in axons and/or cell bodies? Cell bodies or soma are often excluded from HARDI data analysis due to the increased model degeneracy when including a cell soma compartment. Nevertheless, the density of soma in WM—attributed predominantly to glia—has interesting clinical implications, particularly with respect to neuroinflammation [158].

To answer this question, we developed "continuous BENCH" to relate changes in dMRI signal to variations in the density and dispersion of axons or cell soma extracted from microscopy. Continuous BENCH was first validated on synthetic data generated using numerical simulation of microstructure mesh substrates, demonstrating the feasibility of detecting continuous variables simulating axon and soma density. Continuous BENCH was then applied to a real ex-vivo macaque brain with co-registered dMRI and microscopy data. The specific microscopy stains target axons and cell soma, enabling the derivation of metrics of dispersion and density variations of these cellular compartments across the brain. These metrics (termed "continuous variables") provided the axis along which we characterise the direction of change in our measured dMRI signal. We then used continuous BENCH to estimate which biophysical model parameter best explains the measured change in the dMRI signal, as described by the microscopy-derived axon and cell soma metrics.

5.2 Method

We first outline the theory of BENCH (Section 5.2.1), before describing continuous BENCH. The full continuous BENCH pipeline is illustrated in Figure 5.1. BENCH's training stage (Section 5.2.2) characterises changes in a generated dMRI signal ($\mathbf{S}$) due to changes in biophysical parameters ($\frac{\partial \mathbf{S}}{\partial \boldsymbol{\nu}}$; termed "change vector") through the use of a generative biophysical model (M). This is accomplished by training change models with data generated from a biophysical diffusion model for WM (c.f. Section 2.3.3). Next, we used the continuous variables ($\mathbf{x}$) derived from our data and a generalised linear model (GLM) (Section 5.2.3) to compute the measured changes in the dMRI signal with respect to said continuous variables ($\boldsymbol{\beta} = \frac{\partial \mathbf{y}}{\partial \mathbf{x}}$, termed "direction of change"). Finally, BENCH's inference stage (Section 5.2.4) uses the outputs from the previous two steps ($\frac{\partial \mathbf{S}}{\partial \boldsymbol{\nu}}$ and $\frac{\partial \mathbf{y}}{\partial \mathbf{x}}$) to infer which biophysical parameter is most likely to change due to changes in the continuous variables-of-interest.

The theory of BENCH (Section 5.2.1), the training of change models (Section 5.2.2), and the inference stage (Section 5.2.4) were all previously proposed in [155]. The use of continuous variables (Section 5.2.3) and the application of BENCH to relate biophysical parameters to continuous variables-of-interest (Section 5.3 onward) are the main novel extensions of this chapter.

5.2.1 Theory

Suppose there is a biophysical model (M) that generates a dMRI signal ($\mathbf{S}$) with input biophysical parameters ($\boldsymbol{\nu}$), where $\mathbf{S} = M(\boldsymbol{\nu})$. We aim to find a change in which biophysical parameter ($\hat{\Delta\nu}$) best describes a measured change in the dMRI signal ($\boldsymbol{\Delta}\mathbf{y}$) from a baseline dMRI measurement $\mathbf{y}$.

We explain these quantities using an example. $\mathbf{y}$ may represent the dMRI signal measured from a region-of-interest (ROI) in the brain of a healthy control. $\boldsymbol{\Delta}\mathbf{y}$ denotes the difference in dMRI signal measured from the same ROI in a patient

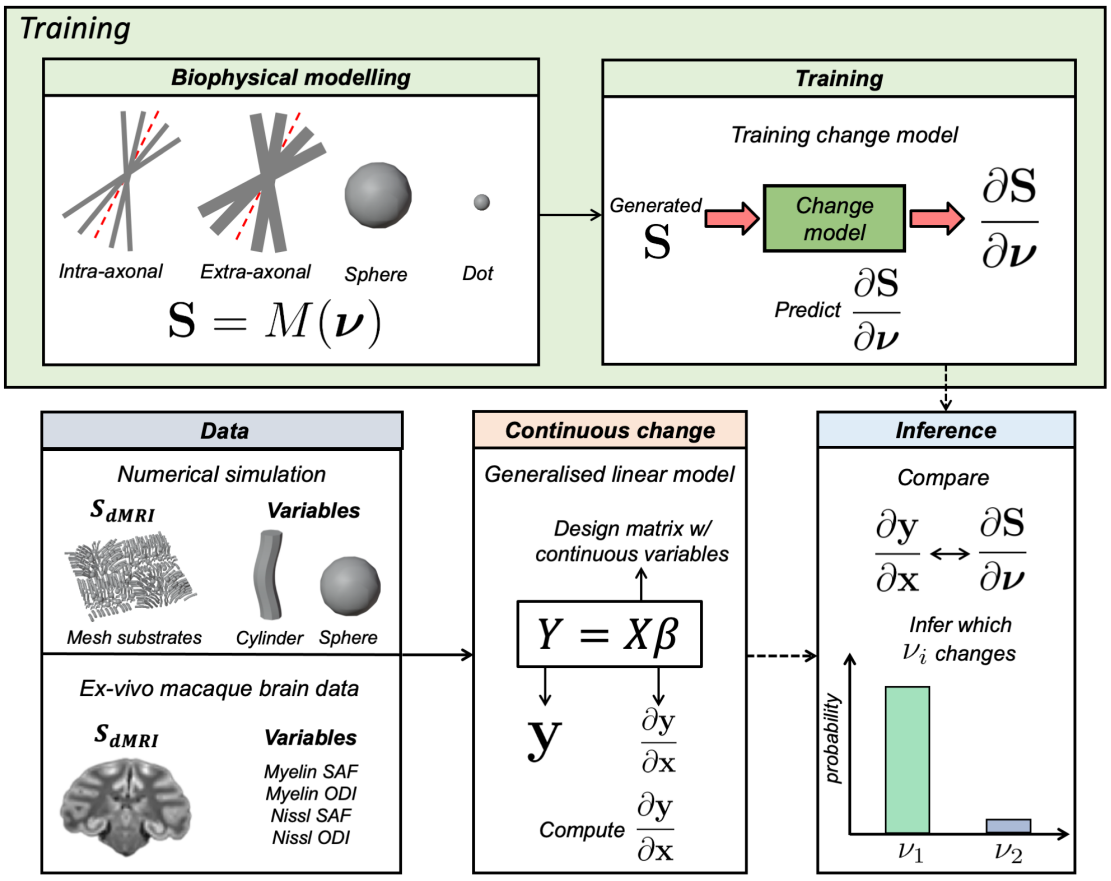

Figure 5.1: An overview of continuous BENCH. First, in BENCH's training stage (green box; "Training"), we aim to infer changes in the generated dMRI signal with respect to changes in biophysical parameters ($\frac{\partial \mathbf{S}}{\partial \boldsymbol{\nu}}$). This is achieved by training "change models" (or regression models) for each biophysical parameter (ν_i) from a designated diffusion biophysical model (M) using generated data. Next, we quantify how the measured dMRI signal changes due to our continuous variables-of-interest ($\frac{\partial \mathbf{y}}{\partial \mathbf{x}}$) using a generalised linear model (beige box; "Continuous change"). This is computed from either numerically simulated or real ex-vivo macaque brain data (blue box; "Data"). The simulated data is to demonstrate continuous BENCH under conditions where the ground truth is known, while the ex-vivo brain data shows continuous BENCH applied in realistic conditions. Finally, the inference stage (blue box; "Inference") uses Bayes' rule to calculate the probability of a given biophysical parameter driving the measured signal variability.

(p), relative to the healthy control (c). If M is invertible, then the biophysical parameter values ($\boldsymbol{\nu_p}$, $\boldsymbol{\nu_c}$) could be computed separately ($\boldsymbol{\nu} = M^{-1}(\mathbf{y})$), and the resulting difference in parameters ($\boldsymbol{\nu_p} - \boldsymbol{\nu_c} = \boldsymbol{\Delta\nu}$) is interpreted to be explaining $\boldsymbol{\Delta}\mathbf{y}$. As $\boldsymbol{\Delta\nu}$ is a vector denoting the change in all biophysical parameters (e.g. diffusivities and volume fractions), we can represent it with

$$\boldsymbol{\Delta\nu} = |\Delta\nu|\hat{\Delta\nu}. \tag{5.1}$$

In BENCH, we assumed that only one parameter changes at a time. Hence, $\hat{\Delta\nu}$ denotes which parameter has changed, and $|\Delta\nu|$ is the amount of change for that parameter. However, if M is degenerate, then multiple biophysical parameter sets ($\boldsymbol{\nu}$) will map to the same measured dMRI signal $\mathbf{y}$. This means that inverting the model to estimate $\boldsymbol{\nu}$, and subsequently $\hat{\Delta\nu}$, is infeasible.

In BENCH, we bypassed the model inversion by inferring $P(\hat{\Delta\nu}|\mathbf{y}, \boldsymbol{\Delta}\mathbf{y})$, the probability of which biophysical parameter is most likely to change given a baseline dMRI signal ($\mathbf{y}$) and a measured change in signal ($\boldsymbol{\Delta}\mathbf{y}$), using Bayes' rule:

$$P(\hat{\Delta\nu} \mid \mathbf{y},\ \boldsymbol{\Delta}\mathbf{y}) \ = \ \frac{P(\boldsymbol{\Delta}\mathbf{y} \mid \mathbf{y},\ \hat{\Delta\nu}\ )P(\hat{\Delta\nu} \mid \mathbf{y})}{\Sigma_{\hat{\Delta\nu}'}\ P(\boldsymbol{\Delta}\mathbf{y} \mid \mathbf{y},\ \hat{\Delta\nu}')\ P(\hat{\Delta\nu}' \mid \mathbf{y})}, \tag{5.2}$$

where the denominator is a normalisation constant, and $P(\hat{\Delta\nu}|\mathbf{y})$ is the prior. In principle, the prior can be any form. Here, we assumed a uniform distribution. This implies that no biophysical parameter is more likely to change given any measured baseline dMRI signal. Hence, we only needed to estimate the likelihood $P(\boldsymbol{\Delta}\mathbf{y}|\mathbf{y}, \hat{\Delta\nu})$, which we achieved through the first stage of BENCH: the training stage.

5.2.2 Training stage

The main objective of this stage is to produce a trained change model to estimate $P(\boldsymbol{\Delta}\mathbf{y}|\mathbf{y}, \hat{\Delta}\nu)$ for each parameter.

Figure 5.2 outlines how this is done, in the context of an example degenerate biophysical diffusion model that has parameters ν_1 and ν_2 (where $\boldsymbol{\nu} = [\nu_1, \nu_2]$). As this is a degenerate model, multiple combinations of ν_1 and ν_2 will map to the same generated dMRI signal data point (where $\mathbf{S} = [S_1, S_2]$).

We aim to train a change model for each parameter (ν_1 and ν_2). We start with ν_1. If we perturb one parameter combination (red datapoint in $\boldsymbol{\nu}$ graph, Figure 5.2) in the direction of ν_1 by a unit amount ($\hat{\Delta\nu}_1$, orange arrow in $\boldsymbol{\nu}$ graph), this produces a change vector in the signal space ($\frac{\partial \mathbf{S}}{\partial \hat{\Delta\nu}_1}$, orange arrow in $\mathbf{S}$ graph). This can then be repeated for the other parameter combinations to obtain a distribution of change vectors (green $N(\boldsymbol{\mu_1}, \boldsymbol{\sigma_1})$ in $\mathbf{S}$ graph). In general, both $\boldsymbol{\mu_1}$ and $\boldsymbol{\sigma_1}$ will vary over the measured dMRI signal space y according to simple functions $C(\cdot)$. During the training phase, we train "ν_1 change models" to estimate this $\boldsymbol{\mu_1}$ and $\boldsymbol{\sigma_1}$ separately, when given a measured baseline dMRI signal data point (purple point in $\mathbf{y}$ graph) as input ($C_{1,\boldsymbol{\mu}} = \boldsymbol{\mu_1}(\mathbf{y})$, $C_{1,\sigma} = \boldsymbol{\sigma_1}(\mathbf{y})$). This process is repeated for other parameters (e.g. ν_2) to train their respective change models (e.g. ($C_{2,\boldsymbol{\mu}} = \boldsymbol{\mu_2}(\mathbf{y})$, $C_{2,\boldsymbol{\sigma}} = \boldsymbol{\sigma_2}(\mathbf{y})$)).

We will now describe in detail 1) how we generated the training data, 2) how we trained the change models, and 3) how we related the output of the trained change models back to the probability distribution of a change in dMRI signal due to a change in a specific parameter ($P(\boldsymbol{\Delta}\mathbf{y}|\mathbf{y}, \hat{\Delta}\nu)$).

Generating training data

We required a different training dataset for each parameter's change models to calculate $\boldsymbol{\mu}$ and $\boldsymbol{\sigma}$. The training dataset is generated by the following steps, for

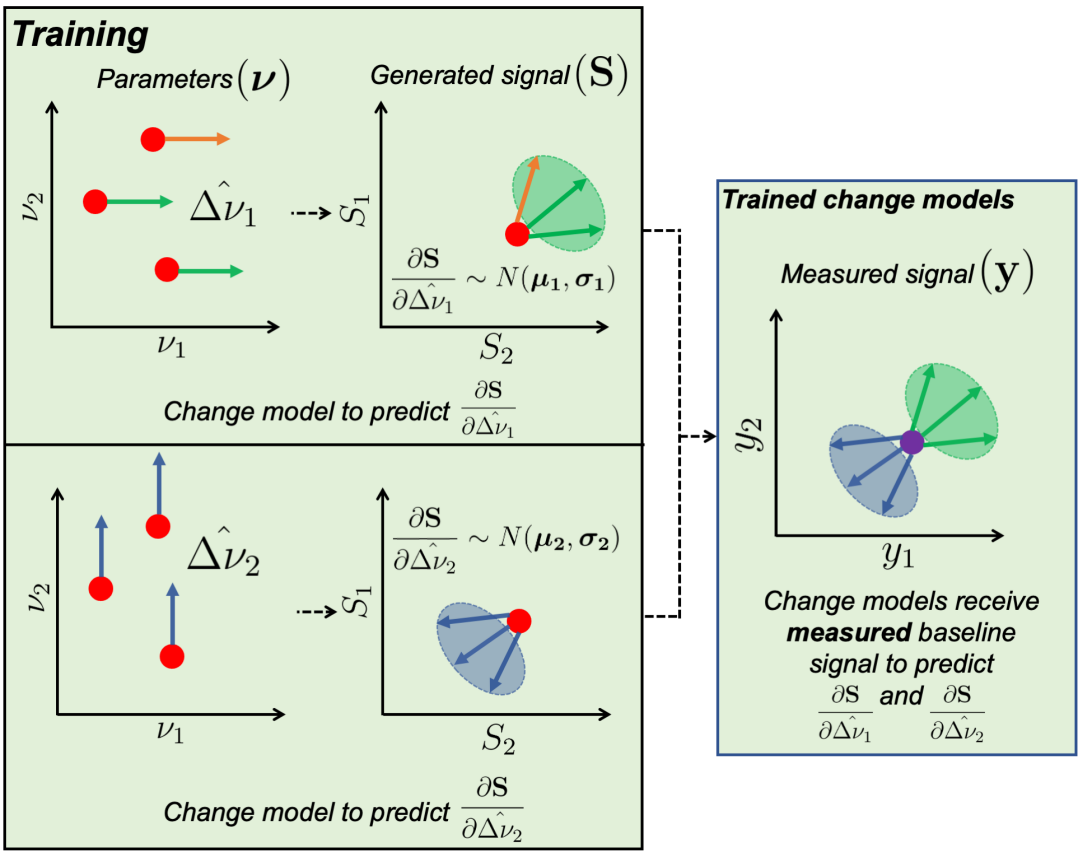

Figure 5.2: Illustration of the training stage. This is done in the context of a degenerate diffusion biophysical model with biophysical parameters ν_1 and ν_2. As the model is degenerate, several parameter combinations (red points, $\boldsymbol{\nu}$ graph) generate the same signal data point (red point, $\mathbf{S}$ graph). During the training phase (box titled "Training"), we aim to train individual change models for these two parameters. Suppose we increase one parameter combination in the direction of ν_1 ($\hat{\Delta\nu}_1$, orange arrow in $\boldsymbol{\nu}$ graph), this maps to a change vector in the signal space ($(\frac{\partial \mathbf{S}}{\partial \hat{\Delta\nu}_1}$) orange arrow in $\mathbf{S}$ graph). If we repeat this for other parameter combinations, we can get a normal distribution of change vectors (green $N(\boldsymbol{\mu_1}, \boldsymbol{\sigma_1})$). For ν_1, we train change models to predict this $\boldsymbol{\mu_1}$ and $\boldsymbol{\sigma_1}$ separately, given a baseline dMRI signal data point. This process is repeated for other parameters (e.g. ν_2) to generate their corresponding change models (box with trained change models). Once the change models are trained (box titled "Trained change models"), they receive a separate measured baseline dMRI signal (purple point, $\mathbf{y}$ graph) to predict the distribution of both change vectors ($\frac{\partial \mathbf{S}}{\partial \hat{\Delta\nu}_1}$, $\frac{\partial \mathbf{S}}{\partial \hat{\Delta\nu}_2}$).

a sample parameter ν_i (where $i = 1, 2, \ldots$ is the parameter index):

1. Sample a parameter combination ($\boldsymbol{\nu}$) from a set of prior distributions. These distributions are predefined empirically based on the data.

2. Generate a signal ($\mathbf{S} = M(\boldsymbol{\nu})$) with the biophysical model (M)

3. Induce a small change in the chosen parameter ($\boldsymbol{\Delta\nu_i} = |\Delta\nu_i|\hat{\Delta}\nu_i$).

4. Generate a new signal ($\boldsymbol{\Delta S} = M(\boldsymbol{\nu} + \boldsymbol{\Delta\nu_i})$) with the new parameter combination.

5. Compute the corresponding change vector $\frac{\partial \mathbf{S}}{\partial \hat{\Delta}\nu_i}$ using:

$$\frac{\partial \mathbf{S}}{\partial \hat{\Delta}\nu_i} \approx \frac{M(\boldsymbol{\nu} + \boldsymbol{\Delta\nu_i}) - M(\boldsymbol{\nu})}{|\Delta\nu_i|}, \tag{5.3}$$

   where we assumed that dMRI signals change linearly with parameter.

6. Repeat steps 1 to 5 to generate a predefined number of pairs of ($\frac{\partial \mathbf{S}}{\partial \hat{\Delta}\nu_i}$,$\mathbf{S}$).

We repeated these steps for all parameters of the biophysical model M. As M is degenerate, there will be cases where different $\boldsymbol{\nu}$ generate the same $\mathbf{S}$, but produce different $\frac{\partial \mathbf{S}}{\partial \hat{\Delta}\nu_i}$. In other words, there is a distribution of $\frac{\partial \mathbf{S}}{\partial \hat{\Delta}\nu_i}$ for each $\mathbf{S}$. In BENCH, we assumed this distribution to be a normal distribution $N(\boldsymbol{\mu_i}, \boldsymbol{\sigma_i})$, which we parameterised with our change models.

Training change models

For each biophysical parameter ν_i, the change models should infer a distribution of change vectors ($N(\boldsymbol{\mu_i}(\mathbf{y}), \boldsymbol{\sigma_i}(\mathbf{y}))$), given a measured baseline dMRI signal ($\mathbf{y}$). Here, we represented our change models as regression models trained on our generated pairs ($\frac{\partial \mathbf{S}}{\partial \hat{\Delta}\nu_i}$,$\mathbf{S}$). To estimate $\boldsymbol{\mu_i}(\mathbf{y})$ for parameter ν_i, the regression model is:

$$\boldsymbol{\mu_i}(\mathbf{y}) = F(\mathbf{y}) \cdot \omega_i, \tag{5.4}$$

where $F(\mathbf{y})$ is the design matrix, and F can be a linear or non-linear transformation of $\mathbf{y}$. Here, we used a linear transformation, where ω_i are the weights of this regression model. Note that $\mathbf{y}$ represents the input measured baseline dMRI signal after the model has been trained, though the generated dMRI signal ($\mathbf{S}$) is used during training. This concept of inputting $\mathbf{y}$ is core to the original BENCH framework, where we only need to train the change models once before carrying out the inference stage with any newly measured baseline and change in dMRI signal [155].

$\boldsymbol{\sigma_i}(\mathbf{y})$ is estimated with a similar formulation, albeit an additional transformation T to ensure that $\boldsymbol{\sigma_i}(\mathbf{y})$ is a positive definite matrix:

$$\boldsymbol{\sigma_i}(\mathbf{y}) = T(G(\mathbf{y}) \cdot \eta_i). \tag{5.5}$$

Briefly, T includes the arrangements of elements, exponentiation of the diagonals, and the matrix multiplication for the inverse Cholesky decomposition. η_i are the weights of this model. G is another design matrix, where the functional form may be different to F. Transformation T is required to create a valid covariance matrix. For more details on T and G, please refer to [155].

For both $\boldsymbol{\mu_i}(\mathbf{y})$ and $\boldsymbol{\sigma_i}(\mathbf{y})$, the training aims to estimate optimal weights ω_i and η_i, which is accomplished by maximising a likelihood function for pairs of $(\frac{\partial \mathbf{S}}{\partial \hat{\Delta\nu_i}}, \mathbf{S})$ in the training data. A different set of weights are estimated for each biophysical parameter. The exact details on the likelihood function and the optimisation process are as published in [155].

Relating change model outputs to the likelihood of measured change

Once the regression models for biophysical parameter ν_i have been trained, they output the mean and variance of the normal distribution of change vectors, such that:

$$\frac{\partial \mathbf{y}}{\partial \hat{\Delta\nu}_i} \sim N(\boldsymbol{\mu_i}(\mathbf{y}), \boldsymbol{\sigma_i}(\mathbf{y})). \tag{5.6}$$

A change vector can be related to a measured change in the dMRI signal through a Taylor expansion:

$$\boldsymbol{\Delta y} \approx \frac{\partial \mathbf{y}}{\partial \hat{\Delta\nu}_i} |\Delta\nu_i|. \tag{5.7}$$

This is effectively the likelihood of a measured change in the dMRI signal $\boldsymbol{\Delta y}$ if only biophysical parameter ν_i changes by amount $|\Delta\nu_i|$, given a measured baseline dMRI signal $\mathbf{y}$. Equation 5.6 can be rewritten as:

$$P(\Delta\mathbf{y}|\mathbf{y}, \hat{\Delta\nu}_i, |\Delta\nu_i|) = N(|\Delta\nu_i|\boldsymbol{\mu_i}(\mathbf{y}), |\Delta\nu_i|^2\boldsymbol{\sigma_i}(\mathbf{y}) + \boldsymbol{\sigma_l}), \tag{5.8}$$

where $\boldsymbol{\sigma_l}$ is termed the "noise covariance matrix" derived for the l^{th} continuous variable. These continuous variables (c.f. Section 5.2.3) and noise covariance matrix (c.f. Section 5.2.4) are discussed and defined later. We then marginalised $P(\Delta\mathbf{y}|\mathbf{y}, \hat{\Delta\nu}_i, |\Delta\nu_i|)$ with respect to $|\Delta\nu_i|$ to get $P(\boldsymbol{\Delta y}|\mathbf{y}, \hat{\Delta\nu}_i)$, which is used in BENCH's inference stage (Section 5.2.4).

5.2.3 Defining directions of change: extending BENCH to continuous variables

BENCH requires us to define a measured baseline dMRI signal $\mathbf{y}$ and a measured dMRI signal change $\boldsymbol{\Delta y}$ that are meaningful to the research question. Here,

meaningful change is defined as a measured change in dMRI signal due to variables-of-interest (i.e. $\frac{\partial \mathbf{y}}{\partial \mathbf{x}}$). We call this a direction of change.

Previously, Rafipoor et al. defined two discrete groups (i.e. healthy controls and patients) [155]. In many cases, however, separating dMRI signal measurements into distinct groups may be arbitrary and/or unmeaningful. Here, we extended the BENCH framework to consider continuous variables to broaden the applicability of BENCH to more research questions. Specifically, we related changes in the dMRI signal to continuous variables-of-interest via a generalised linear model (GLM), in the case where there are p continuous variables:

$$Y_{n\times m} = X_{n\times(p+1)}\beta_{(p+1)\times m}, \tag{5.9}$$

where:

$$\begin{bmatrix} y_{1,1} & y_{1,k} & \cdots & y_{1,m} \\ y_{j,1} & y_{j,k} & \cdots & y_{2,m} \\ \vdots & \vdots & \ddots & \vdots \\ y_{n,1} & y_{n,k} & \cdots & y_{n,m} \end{bmatrix} = \begin{bmatrix} 1 & x_{1,1} & x_{1,2} & \dots & x_{1,p} \\ 1 & x_{j,1} & x_{j,2} & \dots & x_{j,l} \\ \vdots & \vdots & \vdots & \ddots & \vdots \\ 1 & x_{n,1} & x_{n,2} & \dots & x_{n,p} \end{bmatrix} \begin{bmatrix} \beta_{mean,1} & \beta_{mean,k} & \dots & \beta_{mean,m} \\ \beta_{1,1} & \beta_{1,k} & \dots & \beta_{1,m} \\ \vdots & \vdots & \ddots & \vdots \\ \beta_{p,1} & \beta_{p,k} & \dots & \beta_{p,m} \end{bmatrix}. \tag{5.10}$$

Here, $j = 1, \dots, n$ subjects or voxels, $l = 1, \dots, p$ continuous variables, and $k = 1, \dots, m$ dMRI signal summary measures (as described later in Section 5.3.1). Hence, the dMRI signal measured at j^{th} subject or voxel is $\mathbf{y_j} = [y_{j,1}, y_{j,2}, \dots, y_{j,m}]$. The l^{th} continuous variable measured across all subjects or voxels is $\mathbf{x_l} = [x_{1,l}, x_{2,l}, \dots, x_{n,l}]$.

The dMRI signal summary measures averaged across the subjects or voxels is $\boldsymbol{\beta_{mean}} = [\beta_{mean,1}, \beta_{mean,2}, \dots, \beta_{mean,k}]$. The change vector characterising the measured change in dMRI signal summary measures with respect to the l^{th} continuous variable is $\boldsymbol{\beta_l} = [\beta_{l,1}, \beta_{l,2}, \dots, \beta_{l,k}]$, or the direction of change derived using the l^{th} continuous variable. Here, $\beta_{l,k}$ is the partial derivative of the k^{th} dMRI signal

summary measure with respect to the l^{th} continuous variable. We calculated βs by multiplying the matrix of summary measures with the pseudoinverse of the design matrix [159].

5.2.4 Inference stage

In the inference stage, we combined outputs from the training stage and the GLM to infer which biophysical parameter ($\hat{\Delta\nu_i}$) is most likely to change due to a change in the continuous variables-of-interest. From the training stage, this involves the probability distribution of change vectors, ($P(\mathbf{\Delta y}|\mathbf{y}, \hat{\Delta\nu_i})$). From the GLM stage, this involves the mean measured dMRI signal ($\boldsymbol{\beta_{mean}}$) and the directions of change ($\boldsymbol{\beta_l}$). We illustrated the inference stage in Figure 5.3.

First, the mean dMRI signal ($\boldsymbol{\beta_{mean}}$), indicated by the purple data point in Figure 5.3, is the measured baseline dMRI signal. $\boldsymbol{\beta_{mean}}$ is inputted into each change model to determine the distribution of change vectors (i.e. $N(\boldsymbol{\mu_i}(\boldsymbol{\beta_{mean}}), \boldsymbol{\sigma_i}(\boldsymbol{\beta_{mean}}))$), and subsequently, the $P(\mathbf{\Delta y}|\mathbf{y} = \boldsymbol{\beta_{mean}}, \hat{\Delta\nu_i})$ for each biophysical parameter (blue and green ellipses in Figure 5.3).

Next, we computed the measured change in dMRI signal (black data point in Figure 5.3) due to each continuous variable by multiplying their direction of change ($\boldsymbol{\beta_l}$) with the change effect size (δ_l). δ_l is the dynamic range of the continuous variable, as measured directly from the data (described later in Section 5.4). Both $\boldsymbol{\beta_l}$ and δ_l are used to evaluate likelihood $P(\mathbf{\Delta y} = \boldsymbol{\beta_l} \times \delta_l|\mathbf{y} = \boldsymbol{\beta_{mean}}, \hat{\Delta\nu_i})$.

Finally, for each continuous variable, we evaluated the likelihood $P(\mathbf{\Delta y} = \boldsymbol{\beta_l} \times \delta_l|\mathbf{y} = \boldsymbol{\beta_{mean}}, \hat{\Delta\nu_i})$. For each biophysical parameter, this likelihood is inputted into Bayes' rule (Equation 5.2) to generate $P(\hat{\Delta\nu_i}|\mathbf{y} = \boldsymbol{\beta_{mean}}, \mathbf{\Delta y} = \boldsymbol{\beta_l} \times \delta_l)$. We normalised these likelihoods across all biophysical parameters. The final result is an inference (bar chart in Figure 5.3) of which parameter ν_i most likely explains the measured change in dMRI signal induced by a change in a particular variable-of-interest

x_l (e.g. the number of axons or cell bodies). We produced a separate inference for each continuous variable-of-interest.

To account for measurement noise in the dMRI signal, the inference stage uses a covariance matrix of each $\boldsymbol{\beta_l}$, which was earlier termed the "noise covariance matrix" or $\boldsymbol{\sigma_l}$ in Equation 5.8. While this is estimated directly from the data, we adopted different strategies based on the size of the dataset n (i.e. the number of subjects or voxels). We will later describe the strategies separately when analysing either the numerical simulated or ex-vivo data.

5.3 Data simulation and acquisition

5.3.1 Numerical simulations

Monte Carlo simulations [160] of spins diffusing in a geometric space designed to mimic the WM were performed to establish whether our method can detect subtle changes approximating the density of axons and soma. Artificial 3D meshes (Figure 5.4) were created with axons as undulating cylinders (radius = 2.5 μm [161]; undulation amplitude = 1 μm) and cellular soma as spheres (radius = 1.8 μm [132]). Axons were manually oriented to simulate fibre dispersion, approximately following a Watson distribution [64]. Substrates (size = $200 \times 200 \times 25$ μm^3) were generated for various numbers of undulating cylinders (n=[4, 48, 88, 128, 168, 208, 248, 288, 328]) and spheres (n=[0, 9, 15, 21, 27, 33, 39, 45, 51, 57]), which resulted in substrates with varying intra-axonal (0 to 15% of substrate) and sphere (or intra-soma) (0 to 0.2% of substrate) volume fractions, respectively. Simulations were performed using 160,000 spins (uniformly initialised in both intra- and extra-axonal space) with a time step of 8.62 μs [162], a bulk water diffusivity of 1.7 $\mu m^2/ms$ [64], and impermeable membranes. dMRI signals were simulated for each substrate using acquisition parameters identical to the Human Connectome Project [163]: 90 gradient directions acquired at b = 1, 2, and 3 $ms/\mu m^2$ per b-value and

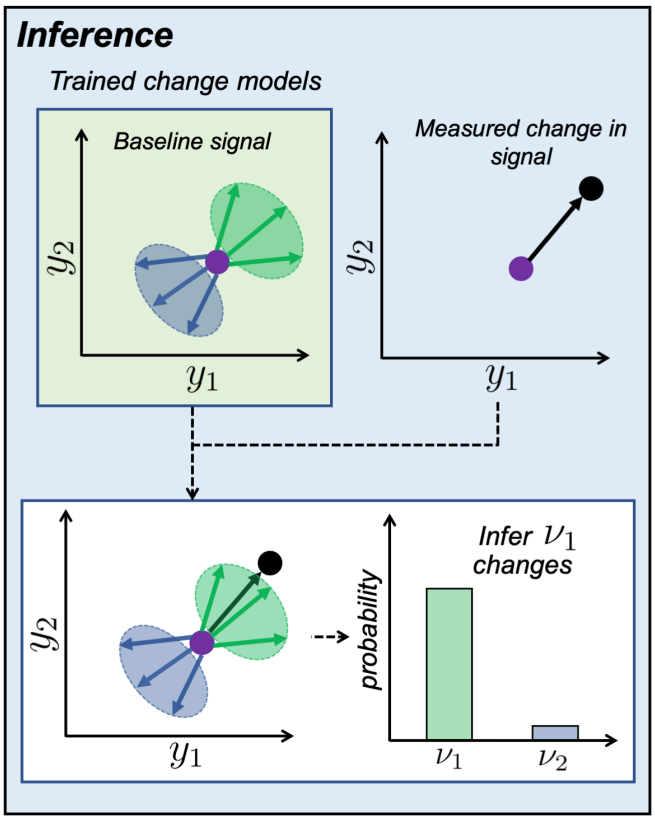

Figure 5.3: Illustration of the inference stage. With the trained change models and a baseline dMRI signal (purple dot), we can generate a distribution of change vectors for ν_1 (green ellipse) and ν_2 (blue ellipse). We then compare a measured dMRI signal change associated with a continuous variable (purple to black dot) with the distribution of change vectors using Equation 5.2 (Bayes's rule equation). This allows us to estimate the probability of each parameter explaining the measured change in the dMRI signal. The pattern of change (described more in Figure 5.7) from the training models which is most similar to that measured in the data will be selected as the most likely (i.e. highest probability) change model. In this case, we would infer that the dMRI signal change associated with the continuous variable is due to a change in ν_1.

18 images acquired at b = 0 $ms/\mu m^2$. Other parameters include: $\Delta = 43.1$ ms, $TE = 65.3$ ms, $G = 56, 79, 97$ mT/m, $\delta = 10.6$ ms.

BENCH is designed to work with rotationally invariant summary measures of the signal, rather than the raw dMRI signals themselves. In brief, we used the coefficients from the spherical harmonic decomposition [63], [164], [165] of the dMRI signal. These coefficients allowed us to calculate summary measures that are invariant to fibre orientations, given that we are only interested in microstructural

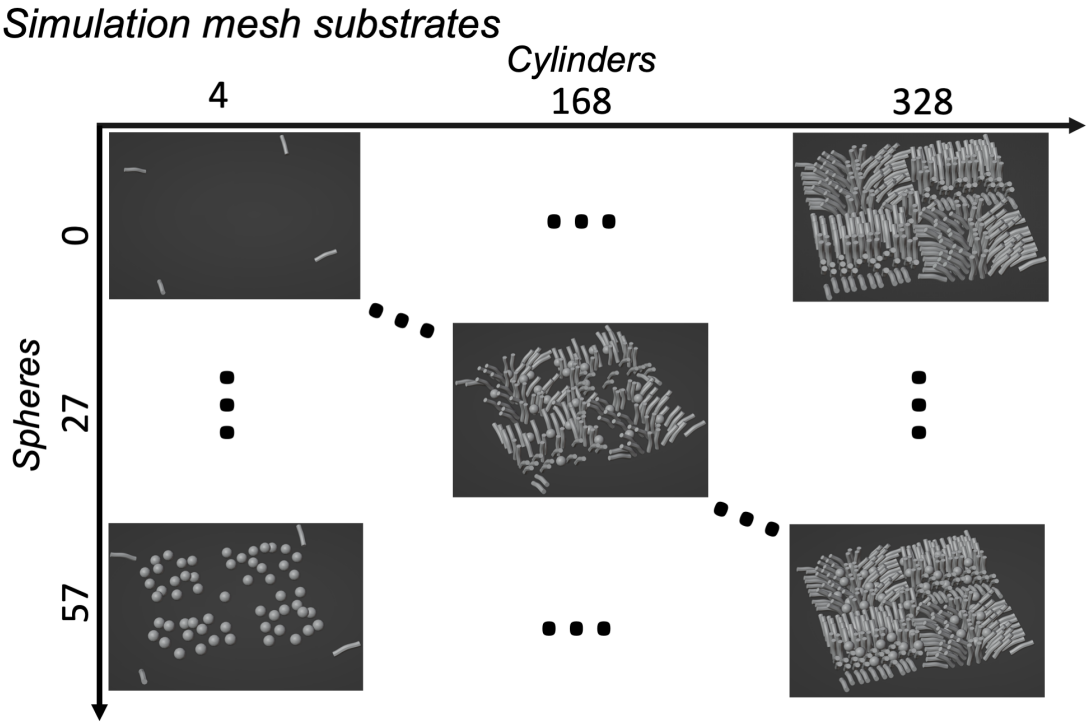

Figure 5.4: The mesh substrates used for simulation. A total of 88 substrates were used, each with a different number of cylinders (myelinated axons; diameter = 5 μm [82]) and spheres (glial cell soma; diameter =10 μm [132]). Simulations were performed with 160,000 spins, a time step of 8.62 μs [162], and a water diffusivity of 1.7 $\mu m^2/ms$ to synthesise dMRI signals. Spins were uniformly initialised in both the intra- and extra-axonal space. Impermeable membranes were assumed. dMRI signals were synthesised with SNR=75.

changes. The summary measures are the weighted average of the squared coefficients (derived at $l = 0$ and 2). For more details, please refer to Appendix 5.10.1. This resulted in 7 rotationally invariant summary measures (2 summary measures $\times$ 3 shells + 1 b_0 mean) per mesh substrate.

5.3.2 Ex-vivo macaque brain data

We then applied continuous BENCH to previously published ex-vivo macaque brain data [166], where postmortem dMRI and co-registered [128] microscopy metrics specific to cell soma and myelin were available. Note that we only describe the data relevant to this work.

Diffusion MRI data

The acquisition and preprocessing of the ex-vivo HARDI data from a perfusion-fixed brain of an adult rhesus macaque have been previously described in [166]. Briefly, this data acquired on a 7T small animal scanner (Agilent) with 1000 gradient directions at b = 4, 7, 10 ms/μm^2, along with 80 images acquired at negligible diffusion-weighting (b $\sim$ 0 ms/μm^2). As the data acquired at b = 4 ms/μm^2 had significant non-linear deformations, it was not used in this particular analysis. Other parameters include resolution = 1 mm isotropic, TE = 42.5 ms, TR = 6.4 s, δ = 14 ms, and Δ = 24 ms. The tissue temperature was kept at a constant 20℃. A WM mask was generated [166], and hand-edited to remove subcortical WM that may have complex microstructure. Rotationally invariant summary measures (2 summary measures $\times$ 2 shells + 1 b_0 mean) were calculated from the DW signal (c.f. Appendix 5.10.1).

Microscopy data

Following MRI data acquisition, the macaque brain was sectioned along the anterior-posterior axis to produce coronal tissue sections (mostly 50 μm thick; 100 μm thick for one section), and processed according to the full microscopy protocols published in [166]. Sections were subsequently processed to produce regularly interspersed slides with a range of contrasts targeting specific cellular constituents (polarised light imaging/histology). In this study, we applied continuous BENCH to the sections stained with Cresyl violet to visualise Nissl bodies, and Gallyas silver, which targets myelin. Each stain was repeated every 350 μm throughout the brain. Sections were imaged at a resolution of 0.28 μm per pixel. All microscopy slices were co-registered to the MRI volume using TIRL [128], [166].

The histology images were analysed to extract two quantitative metrics: the stained area fraction (SAF) and the orientation dispersion index (ODI) (Section 2.2.3). The SAF is a metric for microstructure density, while the ODI describes how dispersed

the microstructure is. The details of how both SAF and ODI are derived for this particular dataset are published in [167]. In brief, stain segmentation was performed using data-driven thresholds based on a weighted-Otsu method [125], similar to that implemented in Chapter 3. Dispersion was quantified by performing structure tensor analysis to estimate the primary fibre orientation per pixel [33]. A Bingham distribution was then fitted to the combined orientations within a voxel to calculate a voxel-wise ODI comparable with MRI.

Continuous BENCH was applied to a subset of samples extracted from the full ex-vivo brain, as only a few microscopy slides were processed for SAF and ODI at the time of this analysis. We only chose WM voxels with available co-registered dMRI, Nissl-derived and myelin-derived data (1702 voxels in total). The final mask, which highlights the subset of samples and WM voxels used, is shown in Appendix Figure 5.10.

5.4 Data analysis

We applied continuous BENCH to both numerical simulation and ex-vivo macaque brain data. For either dataset, we need to specify:

- a generative biophysical model M used for training change models (c.f Section 5.2.2)

- the measured direction of change $\boldsymbol{\beta_l}$ (c.f Section 5.2.3) and the uncertainty on $\boldsymbol{\beta_l}$ (i.e. $\boldsymbol{\sigma_l}$ or the noise covariance matrix for l^{th} continuous variable) (c.f Section 5.2.4)

5.4.1 Biophysical model and change models

Biophysical model

For both datasets, we used an extended WM standard model. This model included an intra-axonal compartment modelled as dispersed sticks, an extra-axonal compartment characterised as dispersed zeppelins, and the intra-soma compartment modelled as a sphere. When analysing data numerically simulated from mesh substrates, we omitted the CSF compartment as we did not assume a free water diffusivity of 3.0 μm^2/ms within the substrates. A dot compartment was included when analysing ex-vivo data. This was to account for a compartment of "stationary water" observed to be present in ex-vivo data. In total, our biophysical models require 9 and 10 model parameters for simulated and ex-vivo data, respectively (Figure 5.5). In both cases, the signal fractions were assumed to sum to 1.

Change models

Each change model was trained using 30,000 pairs of its generated change vector and baseline signal ($\frac{\partial \mathbf{S}}{\partial \hat{\Delta\nu_i}}$,$\mathbf{S}$) produced from the generative biophysical model (c.f. Section 5.2.2). We trained a change model for each biophysical parameter. For signal fractions, we constrained the change in any two of them to sum to 1. For example, an increase in the sphere signal fraction must result in a decrease in either the extra-axonal or the intra-axonal signal fraction. This led to individual change models characterising opposite change between two signal fractions (e.g. sphere fraction replacing extra-axonal fraction ($f_{sph} - f_{ex}$)).

Parameter	Units	Description	Range
f_{in}	-	Signal fraction for intra-axonal compartment	[0, 1]
f_{ex}	-	Signal fraction for extra-axonal compartment	[0, 1]
f_{sph}	-	Signal fraction for intra-soma compartment	[0, 0.10]
ODI	-	Orientation dispersion index	[0.01, 0.50]
$D_{a,in}$	$\mu m^2/ms$	Axial diffusivity for the intra-axonal compartment	[0.01, 2.5] [0.50, 1.5]
$D_{a,ex}$	$\mu m^2/ms$	Axial diffusivity for the extra-axonal compartment	[0.01, 2.5] [0.50, 1.5]
$D_{r,ex}$	$\mu m^2/ms$	Radial diffusivity for the intra-axonal compartment	[0.01, 2.5] [0.50, 1.5]
D_{sph}	$\mu m^2/ms$	Isotropic diffusivity for the intra-soma compartment	[0.01, 2.5] [0.50, 1.5]
R_{sph}	μm	Radius of the intra-soma compartment	[0.01, 10]
f_{dot}	-	Signal fraction for the dot compartment	[0, 0.10]

Used when modelling real ex-vivo data

Figure 5.5

Figure 5.5: Parameters required for the biophysical diffusion models used. The models differ based on which dataset (i.e. simulated or ex-vivo data) we were analysing. The parameters and/or ranges that differ when modelling the ex-vivo data are shaded in grey.

5.4.2 Measured direction of change

Direction of change

The GLM (c.f. Section 5.2.3) was set up with the microscopy metrics as the explanatory variables. For simulated data, the explanatory variables were the number of spheres and cylinders included in each substrate, which served as a proxy for sphere (intra-soma) and cylinder (intra-axonal) volume fractions, respectively. When analysing ex-vivo data, we used the four microscopy metrics within the same brain: the Nissl SAF, Nissl ODI, myelin SAF, and myelin ODI.

With the GLM, we defined the baseline dMRI signal $\boldsymbol{\beta_{mean}}$ and the direction of change in different metrics, for both the simulated data ($\boldsymbol{\beta_{cylinders}}$, $\boldsymbol{\beta_{spheres}}$) and the ex-vivo data ($\boldsymbol{\beta_{NisslSAF}}$, $\boldsymbol{\beta_{NisslODI}}$, $\boldsymbol{\beta_{myelinSAF}}$, $\boldsymbol{\beta_{myelinODI}}$). For ex-vivo data, we first investigated how each microscopy-derived metric individually explains variance in the dMRI data by performing a separate GLM for each metric (termed "single regressor"). We then determined how each metric uniquely explains variance in the dMRI data by using all metrics as regressors in the same GLM design matrix (termed "all regressors").

As previously explained in Section 5.2.4, we required the measured change in the dMRI signal due to each continuous variable for inference. This measured change was computed by multiplying their change vector ($\boldsymbol{\beta_l}$) with the change effect size (δ_l). In the simulated data, the change effect sizes for cylinders and spheres are the full range of cylinders (n= 57) and spheres (n= 328), respectively. For the ex-vivo data, the change effect size for each microscopy-derived metric was taken to be the 99.9 minus 0.1 percentile of the microscopy-derived metric's distribution across the brain.

Noise covariance

BENCH's inference stage also requires the uncertainties on estimates of the different directions of change (i.e. noise covariance). For the simulated data, $\boldsymbol{\sigma_{cylinders}}$ was taken to be the covariance of $\boldsymbol{\beta_{cylinders}}$ computed from 100 different instances of additive Rician noise (SNR=75). $\boldsymbol{\sigma_{spheres}}$ was derived similarly for $\boldsymbol{\beta_{spheres}}$. In the ex-vivo data, the noise covariance was derived from the data via a bootstrapping method (2000 iterations). In each iteration, we sampled 1000 voxels from the white matter mask and computed $\boldsymbol{\beta_{NisslSAF}}$, $\boldsymbol{\beta_{NisslODI}}$, $\boldsymbol{\beta_{myelinSAF}}$ and $\boldsymbol{\beta_{myelinODI}}$. $\boldsymbol{\sigma_l}$ was taken to be the covariance of $\boldsymbol{\beta_l}$ across iterations. Because the signal fractions were constrained to sum to 1 in each voxel, this resulted in the b_0 mean term (i.e. equivalent to dMRI signal acquired at b $\sim$ 0 ms/μm^2 or $\mathbf{S_0}$) of the dMRI signal summary measures possessing negligible variance when measured across all voxels. This is problematic for BENCH's originally implemented inference stage because it requires a non-zero variance term for b_0 mean term. To address this issue, we added a fixed noise term along the matrix's diagonal (i.e. variance for all summary measures, including b_0 mean). This term is the noise variance computed from the SNR estimated from $\mathbf{S_0}$ (σ=1/SNR) divided by the number of voxels.

5.4.3 Inference

The measured change in dMRI signal due to different continuous variables ($\boldsymbol{\beta_l} \times \delta_l$), along with their noise covariance term ($\boldsymbol{\sigma_l}$), were used for inference. In the simulated data, we present the inferred probability averaged across 100 iterations. For ex-vivo data, the final probabilities were generated from a single inference.

5.5 Results

5.5.1 Numerical simulations

Inference

Continuous BENCH was applied to simulated data from mesh substrates with differing numbers of cylinders and spheres (i.e. different axon and sphere volume fractions) to validate its ability to attribute these changes to appropriate biophysical model parameters (i.e. different f_{in} and f_{sph}). For increasing numbers of cylinders, the highest parameter changes were $(f_{in} - f_{sph})$ and $(f_{in} - f_{ex})$ (i.e. increasing intra-axonal signal fractions replacing sphere and extra-axonal signal fractions (Figure 5.6; both probabilities$\sim$40%)). With an increase in spheres, continuous BENCH primarily inferred (Figure 5.6; probability$\sim$70%) a correct change in $(f_{sph} - f_{ex})$.

We show the change in each dMRI signal summary measure with respect to the number of cylinders or spheres measured from the simulated data (Figure 5.7, left, titled "Measured"). This is termed the "pattern of change". We visually compared the measured pattern of change with the output of the BENCH training stage, where each subplot on the right shows the generated pattern of change for each biophysical parameter (Figure 5.7, right, titled "Generated"). If the training stage's pattern of change for a particular biophysical parameter is most similar to the measured pattern of change due to a metric (e.g. number of cylinders), BENCH infers a link between this parameter and the metric with high probability. We observed that a change in the number of cylinders (Δcylinders) (green subplot under "Measured") resulted in a pattern of change most similar to the generated profiles of change for $(f_{in} - f_{ex})$ and $(f_{in} - f_{sph})$ (green subplots under "Generated"). A measured pattern of change due to the number of spheres (Δspheres) (red subplot under "Measured") is most similar to the generated pattern of change for $(f_{sph} - f_{ex})$ (red subplot under "Generated"). These expected results suggest that our continuous BENCH results are reasonable.

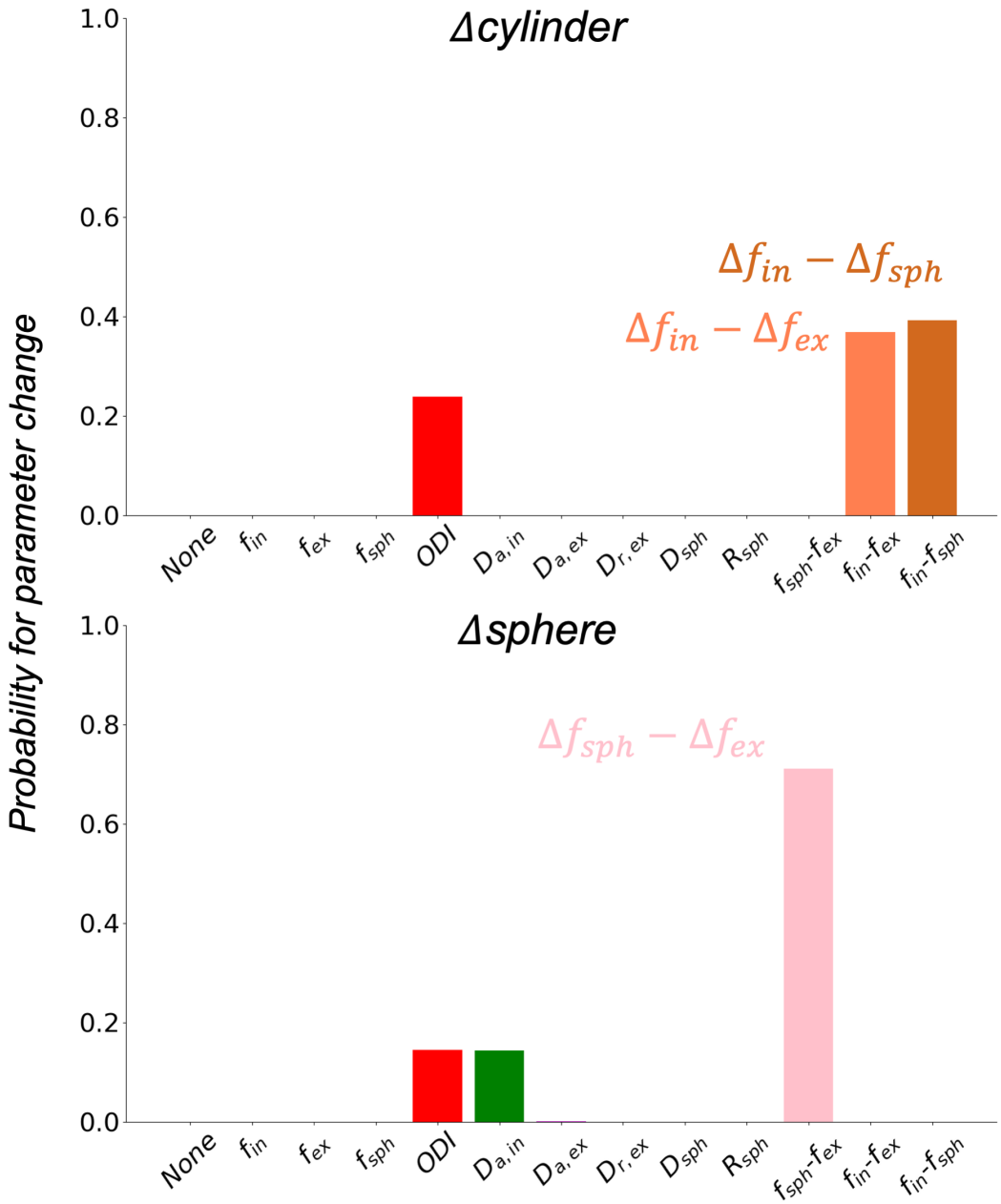

Figure 5.6: Inference of which biophysical parameter(s) is likely to change, given a change in cylinders and spheres in the mesh substrates. When there was a change in cylinders ("Δcylinder"), continuous BENCH primarily inferred intra-axonal volume fraction replacing extra-axonal and sphere volume fractions ("$\Delta f_{in} - \Delta f_{ex}$", "$\Delta f_{in} - \Delta f_{sph}$"). Continuous BENCH also inferred that the ODI parameter may have changed. For the continuous variable corresponding to change in spheres ("Δsphere"), an increase in sphere volume fraction replacing extra-axonal volume fraction ("$\Delta f_{sph} - \Delta f_{ex}$") was inferred, as expected, with secondary inferences of changes in ODI and the intra-axonal axial diffusivity ("$\Delta D_{a,in}$").

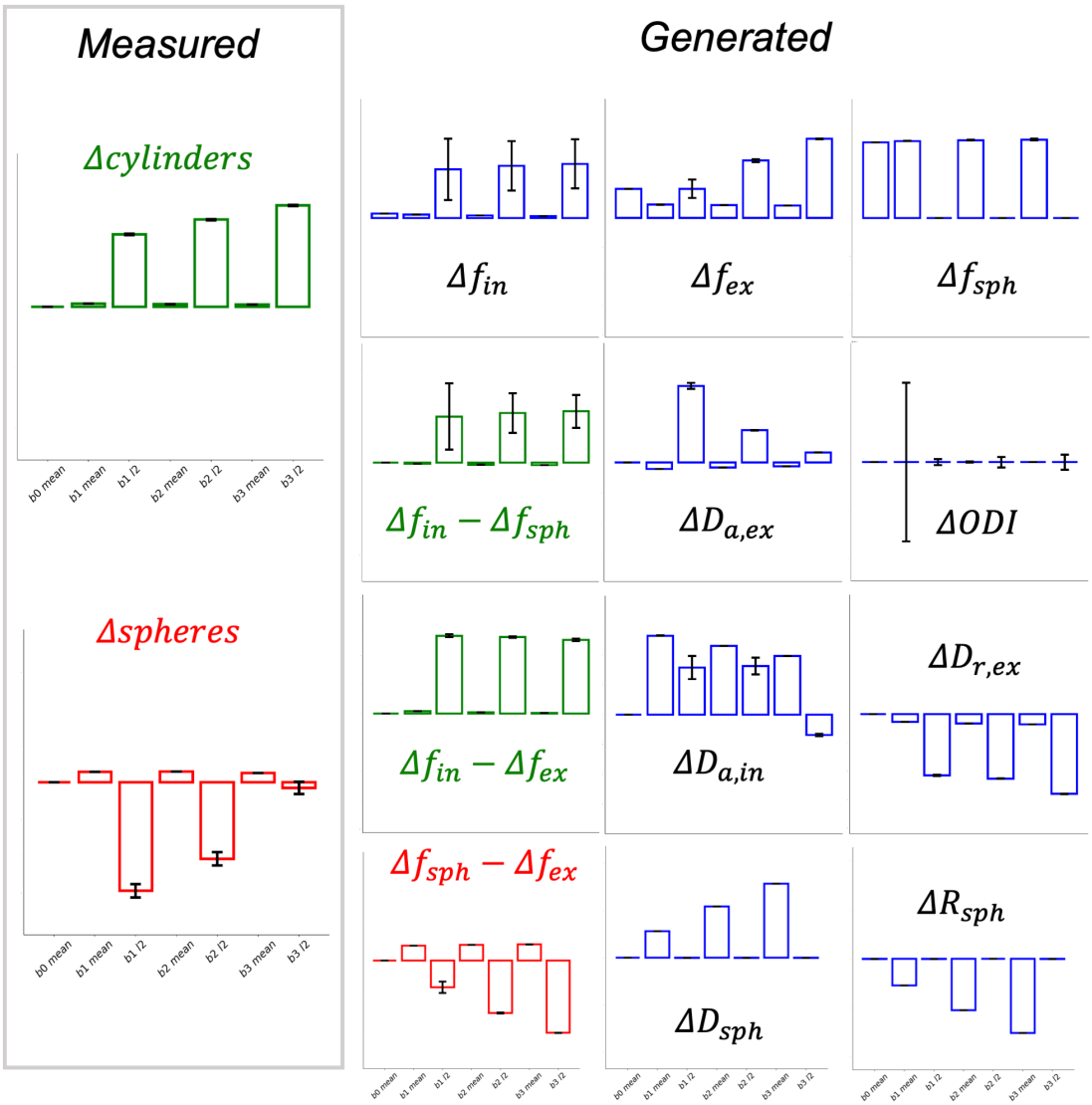

Figure 5.7: The pattern of how each dMRI signal summary measure changes, given a change in a quantity (i.e. continuous variable or biophysical parameter). This is termed the "pattern of change". The bar chart shows the mean change for each summary measure, along with its standard deviation. The pattern of change measured from the continuous variables-of-interest in the numerical simulation (left box) is visually compared with the pattern of change generated from BENCH's trained change models. We colour-matched the BENCH profiles of change most visually similar to the measured profiles of change (green: cylinders; red: spheres). x-axis (dMRI summary measures): b_0 mean, b_1 mean, b_1 $l2$, b_2 mean, b_2 $l2$, b_3 mean, b_3 $l2$

5.5.2 Ex-vivo macaque brain data

Inference

We first explored how each metric independently explains the variations in the dMRI data ("single regressor"). To better understand the interplay between different metrics and to account for shared variance, we incorporated all metrics simultaneously into a unified GLM design matrix ("all regressors"). This approach not only allows us to understand the combined influence of different metrics but also enables us to discern the contribution of each metric by considering the overlapping variance they may share.

Single regressor Continuous BENCH was applied to ex-vivo macaque data to relate changes in biophysical model parameters to microscopy-derived continuous variables—specifically, myelin and Nissl SAF and ODI (Figure 5.8). Here, each continuous variable was used as the only regressor in separate GLMs. An increase in myelin SAF was primarily attributed to a reduction in radial diffusivity in the extra-axonal space ($D_{r,ex}$) (probability$\sim$60%). The increased density of Nissl was primarily linked to the dot compartment signal fraction being replaced by the extra-axonal signal fraction ($f_{ex} - f_{dot}$) (probability$\sim$60%) and secondarily by the intra-axonal signal fraction ($f_{in} - f_{dot}$) (probability$\sim$40%). An increase in either myelin- or Nissl-derived dispersion led to an increase in the ODI biophysical model parameter (probability$\sim$100%).

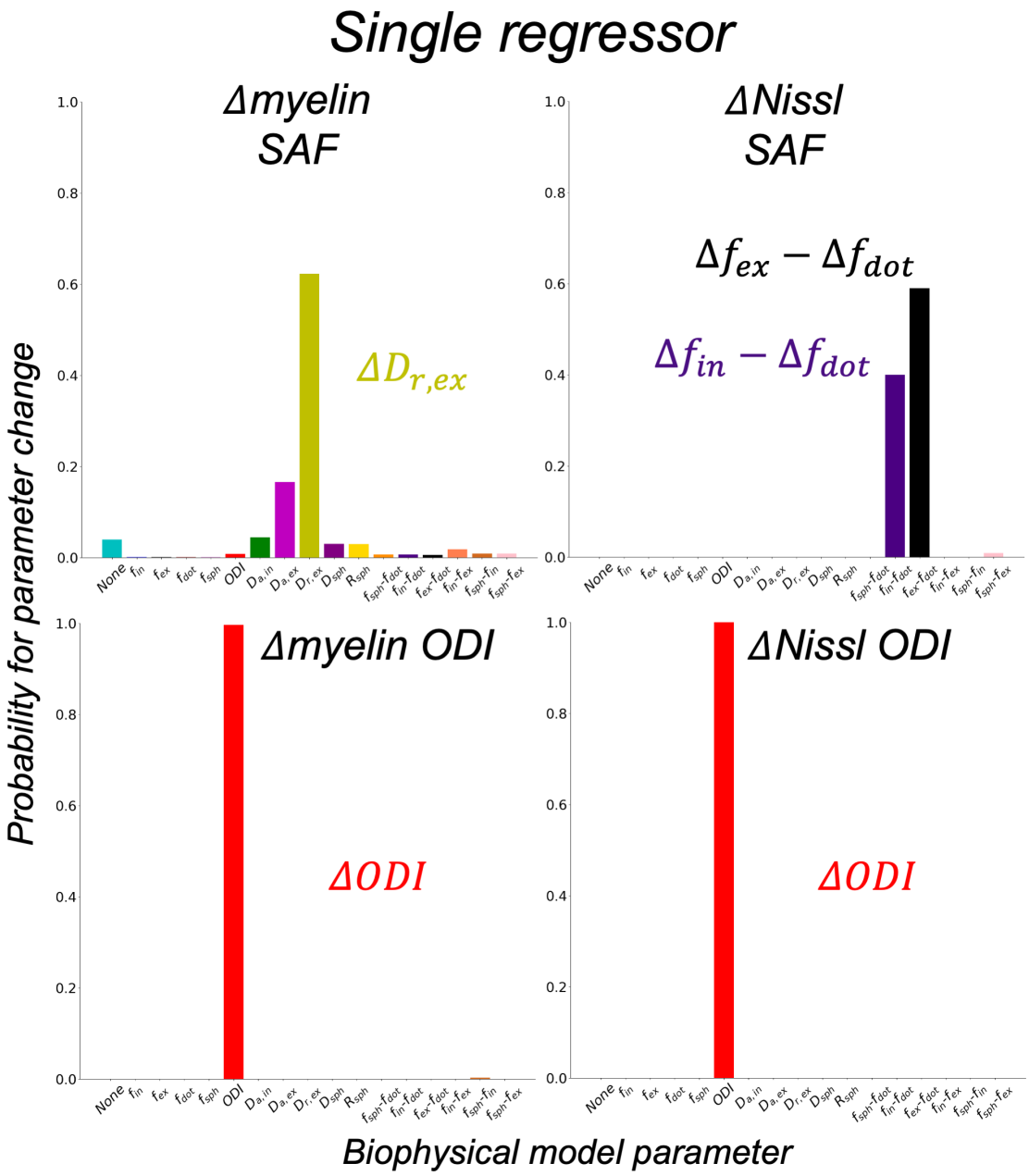

Figure 5.8: Inferred probabilities when using each microscopy-derived metric (one plot per metric) as the only regressor in the GLM. The x-axis lists the different biophysical model parameters present in the model, while the y-axis denotes the probability of the biophysical model parameter changing, given a change in the microscopy-derived metric. Each bar plot represents the parameter's probability normalised by the inferred probabilities of all model parameters. SAF: stained area fraction, ODI: orientation dispersion index

All regressors When using all metrics simultaneously as regressors in the GLM, the inferred probabilities were largely similar to when single regressors were used, except for the Nissl-derived ODI (Figure 5.9). An increase in Nissl-derived ODI was not confidently linked to any specific parameter change, with "None" the highest probability at ∼13%. This means continuous BENCH infers that the change in signal associated with Nissl-derived ODI is better explained by noise rather than any biophysical model parameter.

5.6 Discussion

In this work, we developed continuous BENCH to relate changes in biophysical model parameters to changes in any continuous variable. We first applied continuous BENCH to simulated data, where the most likely change in parameters inferred by BENCH accurately reflected the simulated changes in spheres/cylinders in mesh substrates, validating our approach. We then applied continuous BENCH to ex-vivo macaque MRI data with microscopy metrics acquired in the same brain, where our results are both well aligned with findings from previous studies and suggest novel links between biophysical model parameters and "ground truth" microscopy.

5.6.1 Numerical simulations

The measured pattern of change from the data and those inferred by BENCH were well aligned, which demonstrates the overall approach when the ground truth is known. When applied to mesh substrates with different numbers of cylinders (representing axons) or spheres (soma), continuous BENCH inferred the most probable change to be an increase in f_{in} and f_{sph} (both replacing other signal fractions), respectively. These results confirm that continuous BENCH can accurately infer changes in soma- and axon-like structures, within the assumptions of this highly simplified simulation where membranes are impermeable.

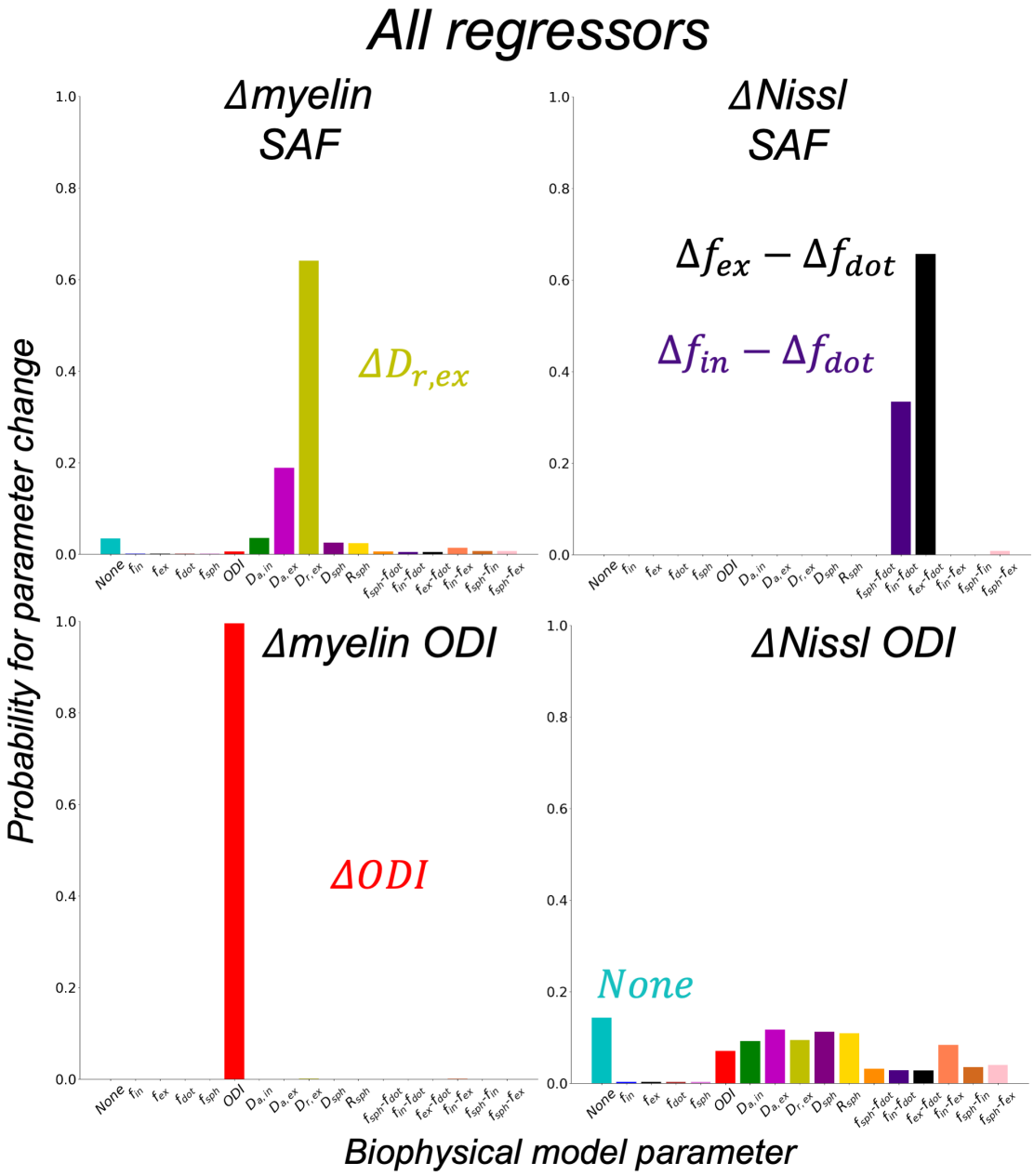

Figure 5.9: Inferred probabilities when using all microscopy-derived metrics as regressors in the same GLM. Results are shown as similarly described in Figure 5.8.

Although cylinders are linked to the intra-axonal compartment, continuous BENCH infers a replacement in both the sphere ($f_{in} - f_{sph}$) and extra-axonal ($f_{in} - f_{ex}$) compartments. The former is unexpected; in the mesh substrates, we simulated a decrease in the extra-axonal compartment when the number of cylinders was increased (i.e. increased intra-axonal compartment), without altering the sphere compartment. This result may be explained by the relatively low packing densities simulated in our substrates, where diffusing spins in the extra-axonal space will encounter fewer membranes. Therefore, diffusion in the extra-axonal space may be better characterised by an isotropic diffusion compartment (e.g. ball/CSF, sphere) rather than the axially symmetric zeppelin we used, which represents anisotropic diffusion. This may explain why the isotropic sphere compartment is identified as being replaced as we add more cylinders to the apparently 'isotropic' extra-axonal space, given that no CSF compartment was modelled. Regardless, BENCH still mainly links cylinders to f_{in}, as confirmed by the similar generated (Δf_{in}) and measured (Δcylinders) patterns of change (Figure 5.7).

Notably, in both cases where the numbers of cylinders or spheres changed, continuous BENCH inferred some probability of ODI changing. For cylinders, there will be a real change in orientation dispersion. As the number of cylinders differs between substrates, it is impossible to precisely maintain the same distribution of cylinder orientations between mesh substrates.

Increasing the number of spheres in our mesh substrates may lead to a decrease in extra-axonal radial diffusivity due to the increased restriction in water diffusion. However, increasing the orientation dispersion of cylinders should have a similar effect on the dMRI signal as would an increase in the extra-axonal radial diffusivity [72]. This presents a clear inconsistency regarding how diffusivities would change if ODI was truly associated with spheres in our substrates. We suspect that the link between ODI and spheres is due to the uncertainty in estimating its change vectors (i.e. $\frac{\partial \mathbf{S}}{\partial ODI}$). This uncertainty is evident from the large variances observed in the pattern of change subplot (ΔODI subplot in Figure 5.7). These large variances

suggest that a small change in the ODI leads to a large change in the dMRI signal summary measures, particularly in its $l2$-terms that measure tissue anisotropy.

5.6.2 Ex-vivo macaque brain data

Myelin SAF

In our results, myelin SAF, a proxy measure of myelin density, was linked to radial diffusivity in the extra-axonal space ($D_{r,ex}$). This aligns well with previous studies that have hypothesised and shown that decreased myelin around axons is associated with an increased radial diffusivity [168], [169]. Myelin has a short T_2 ($\sim$10 to 30 ms [170]), relative to the echo time (42.5 ms) used when acquiring the ex-vivo MRI data. Therefore, myelin does not directly contribute to the dMRI signal via a specific signal compartment, though its lipid bilayers can still restrict diffusing water. Given that we also assume radial diffusion in the intra-axonal compartment to be negligible, the restriction of water diffusion due to myelin should be reflected as a change in radial diffusion in the extra-axonal space.

Nissl SAF

Continuous BENCH primarily relates increasing Nissl SAF to an increase in f_{ex}. In WM, Nissl stains reflect glia, rather than neurons. Hence, Nissl SAF is a metric for glial cell soma density. An increase in glial cell soma might lead to a change in the sphere or intra-soma signal fraction (f_{sph}) and/or the radius of the soma (R_{sph}) if exchange across the soma boundaries is negligible. Conversely, an increase in glial cell soma may also result in an increase in the extra-axonal signal fraction (f_{ex}), if exchange is fast and the sphere/extra-axonal space are in effect combined. Our results indicate the latter. This is contrary to what we expected, as our analysis of simulated data revealed continuous BENCH's ability to detect changes in sphere-like compartments. We hypothesise that the deviations in inferred model

parameters between simulated and ex-vivo data may be linked to fundamental differences between postmortem tissue and what we assume in mesh substrates (e.g. sphere and cylinders with impermeable membranes, bulk water diffusivity$\sim$1.7 μm^2/ms) when generating our simulated data.

Continuous BENCH also infers that increasing Nissl SAF relates to a decrease in the dot compartment signal fraction. The microstructural source of the "stationary" dot compartment is unclear. A "dot"-like compartment measured from in-vivo data may be related to the noise floor, if noise characteristics are not properly accounted for [79]. Ex-vivo data generally is modelled by a much larger dot compartment ($\sim$30%) and is often attributed to fixation effects and/or temperature dependence of postmortem tissue when scanning [76], [80], [81]. Recently, Veraart et al. hypothesised that the dot compartment is related to water trapped in vacuoles formed in the myelin sheaths in fixed tissue, following temperature-dependent (i.e. below 32℃) disruption of the myelin sheath's multilamellar structure [82]. This hypothesis implies that a decrease in the dot compartment relates to a decrease in myelin sheaths trapping these vacuoles. This also aligns with what we have previously seen in other postmortem datasets acquired in our group [166], [171], where we observed a larger dot compartment signal fraction in WM versus GM. Assuming this hypothesis is true, our results suggest that increased Nissl SAF might be linked to lower myelin content, and could be explained by an increased proliferation of microglia in regions undergoing or have undergone demyelination.

Notably, continuous BENCH also infers a potential increase in f_{in} , with $(f_{in} - f_{dot})$ the second mostly likely parameter change for Nissl SAF. f_{in} describes the signal fraction related to "stick-like" tissue features, which may include glial processes alongside axons. The observed increase in f_{in} could be explained by there being more glial processes contributing to the dMRI signal in regions of high Nissl SAF. This interpretation is consistent with the models proposed and results published by other studies [73], [74] which have attempted to model the glia's effect on the dMRI signal.

Myelin and Nissl ODI

Reassuringly, our results indicate that the biophysical model parameter ODI best explains the variation in microscopy-derived ODI. This is true for ODI metrics derived from both myelin and Nissl stains when continuous BENCH modelled them as single regressors (Figure 5.8). However, this relationship disappears when considering all microscopy metrics concurrently in the same GLM. Here, the Nissl-derived ODI is no longer attributed to any model parameter (Figure 5.9). Instead, the unique variance of the myelin-derived ODI is attributed by continuous BENCH to model parameter ODI, and that the Nissl stain contributed no new information in the context of axonal fibre bundle dispersion.

What Nissl-derived orientation dispersion metrics (i.e. ODI) actually represent is an avenue that requires more investigation. These metrics are assumed to reflect the organisation of glial cells which may be organised to follow axonal orientation. This assumption is consistent with results published by Schurr and Mezer, where they showed visual similarities between the orientation maps derived from Nissl staining and polarised light imaging of WM regions in human and nonhuman primate brains [172]. Our results imply that although Nissl-derived ODI may provide a useful approximation for axonal dispersion in the WM, the axonal dispersion probed by dMRI (i.e. via ODI) is nevertheless more accurately represented by ODI derived from myelin staining.

5.7 Limitations

There are limitations to this study. First, our numerical simulation only validates continuous BENCH's ability to accurately infer simple changes in intra-soma and intra-axonal compartments in specific conditions, such as the case where membranes are impermeable. These conditions may not be met when applying continuous BENCH to ex-vivo data. This can be addressed by performing simulations that

include other conditions, such as fast exchange between compartments and/or a different bulk diffusivity due to fixation effects. Second, the mesh substrates used for simulations are not microstructurally realistic. Future validation work would benefit by incorporating more realistic packing densities, brain cell morphologies [173], [174], axon diameters (i.e. $\sim$1 μm [161] instead of 5 μm), and a more realistic bulk water diffusivity ($\sim$2-3 μm^2/ms) into their substrates. Given that we also performed inferences on ex-vivo dMRI data, our analysis would also benefit from substrates simulating ex-vivo conditions. Third, the biophysical model used when analysing ex-vivo data may not contain all compartments sensitive to changes in microscopy metrics. In future biophysical models, consideration could be given to include an extra unrestricted isotropic water compartment, due to its potential sensitivity to changes in cellular soma with non-negligible exchange with the extra-cellular space. Fourth, dMRI data acquired at b = 4 ms/μm^2 was excluded due to substantial non-linear deformations. Consequently, the analysis focused on data obtained at b = 7 and 10 ms/μm^2. While including lower b-values could potentially enhance the characterisation of the dMRI signal, the primary determinant of results accuracy lies in the training of the change models. For this study, we trained the change models using simulated dMRI data corresponding to the same set of b-values (i.e., b = 7, 10 ms/μm^2). We do not anticipate a significant change in the results even if we include data acquired at lower b-values (i.e. b = 4 ms/μm^2), provided the change models are consistently trained with the same set of b-values. Fifth, our study was performed using a small subset of slides extracted from the whole macaque brain where, as data becomes available, we plan to repeat these analyses on slides spanning the entire brain. Lastly, we do not incorporate other microscopy-derived metrics that may relate to dMRI. For example, we do not include metrics derived from neurofilament staining, which may better explain variation in ODI or other model parameters.

5.8 Conclusion

We introduced continuous BENCH, a pipeline to infer changes in continuous variables using degenerate biophysical diffusion models. Here, continuous BENCH was used to examine dMRI's sensitivity to changes in axons and glia. Our method was first validated on simulated data. We then applied it to ex-vivo macaque brain data to investigate the dMRI signal's specificity to myelin and glial cell soma in the WM. We confirmed previously observed specificity of MRI parameters relating to myelin density and dispersion. We showed that an increase in myelin specifically leads to a decrease in radial diffusivity in the extra-axonal space. The dispersion derived from the microscopy of myelinated axons was also confidently linked to a measured change in the model parameter orientation dispersion index. Finally, we reported that increased glial cell soma density is related to an increase in extra-axonal compartment. This may suggest fast exchange across the soma boundary and that the intra-soma/extra-axonal space are in effect combined. Further, we observed a complementary decrease in the dot compartment, which we hypothesise to be increased glial proliferation following demyelination. Together, this demonstrates continuous BENCH as an effective method to uncover specific relationships between microscopy and complex biophysical models that are otherwise inaccessible due to solution degeneracies.

5.9 Acknowledgements and contributions

I am immensely grateful to Amy Howard for providing the ex-vivo data for this study, and to Michiel Cottaar and Hossein Rafipoor for their valuable feedback on the implementation and troubleshooting of BENCH. My personal contributions are the design and implementation of continuous BENCH. This involves adapting the code from the original BENCH to develop continuous BENCH. My contributions also include data simulation, data analysis, and manuscript writing and review.

5.10 Appendix

5.10.1 Summary measures for diffusion MRI data

dMRI summary measures were calculated using the spherical harmonic decomposition [164] of the dMRI signal. Here, the dMRI signal can be decomposed into a unique linear combination of orthonormal basis functions over the surface of a unit sphere (spherical harmonics):

$$S(\theta, \phi) = \sum_{l=0}^{\infty} \sum_{m=-l}^{l} C_{l,m} Y_{l,m}(\theta, \phi). \tag{5.11}$$

Here, the dMRI signal S is parameterised by the polar (θ) and azimuthal (ϕ) angles of the standard spherical coordinate system and is now described as a linear combination of coefficients (C) and spherical harmonics (Y) up to a pre-decided degree $l = 0, 1, 2, \dots$ and order $m = -l, \dots, l$. Since the dMRI signal S is symmetric around the origin, only even-degree harmonics (i.e., $l = 0, 2, 4, \dots$) have non-zero coefficients.

We then computed rotationally invariant measures for each shell of dMRI signal as:

$$y_l = \frac{1}{2l+1} \sum_{m=-l}^{l} C_{l,m}^2, \tag{5.12}$$

where y_l is the summary measure at degree l for a single shell of data [63], [165]. Here, we set $l = 0, 2$ (i.e. 0th and 2nd degree), since a higher l quantifies the signal anisotropy, but at a much lower SNR. Lastly, we took the mean over the norm to ensure that the scale remains constant across degrees. With this formulation, we summarised all measured dMRI signal data points with 5-7 rotationally invariant summary measures (2 summary measures $\times$ 2-3 shells + 1 b_0 mean) per voxel.

5.10.2 Mask for ex-vivo macaque brain data

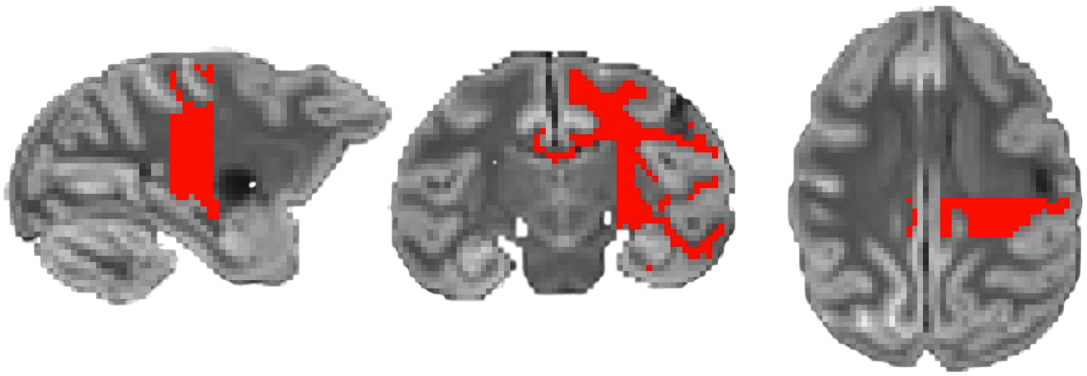

Figure 5.10: The final WM mask (red) containing the 1702 voxels used for analysis. The mask is overlaid on the ex-vivo dMRI data of the macaque brain.

6

Conclusion and future directions

Contents

In this thesis, we have proposed techniques to improve on current methods that aim to compare and characterise relationships between qMRI parameters and tissue parameters derived from chemical and IHC staining. In Chapter 3, we improved the microscopy analysis process by introducing a pipeline that rapidly extracts quantitative metrics from IHC data in a data-driven manner. Importantly, the pipeline addresses common IHC artefacts, which, if overlooked, might lead to spurious MRI-IHC correlations. Chapter 4 demonstrated how this pipeline can be applied alongside high-quality MRI-histology co-registrations to perform multimodal MRI-IHC analyses across multiple brain regions and subjects to derive important MRI-IHC relationships. Chapter 5 develops a method for advanced

microstructural modelling of the dMRI signal ("continuous BENCH"), to link biophysically meaningful model parameters from dMRI to microscopy-derived metrics for axons and glial cell soma. These techniques serve as building blocks in facilitating a more precise interpretation of microstructural change from MRI parameters and inspire a more structured methodology in preparing and processing microscopy data when relating them to MRI data.

6.1 Future work

Building on the techniques presented in this thesis, we explore how our automated pipeline can be further leveraged in bridging the gap between microscopy and MRI. We demonstrate the pipeline's adaptability to a different dataset and discuss how the pipeline can be utilised for the curation of future IHC datasets. Later, we delve into other opportunities to employ continuous BENCH, linking continuous metrics beyond microscopy to dMRI data.

6.1.1 Mouse models to understand MRI-microscopy relationships

As demonstrated in Chapters 3 and 4, the automated pipeline is a step forward in interpreting the specific microstructural underpinnings of MRI signal changes. However, there are several factors that prevent a more complete understanding of MRI-microscopy relationships. Firstly, these relationships were characterised in the context of postmortem tissue, making direct translation to in-vivo MRI, and subsequent clinical application, non-trivial. To unlock MRI's full potential in non-invasively providing diagnostic and mechanistic insight into the brain, we need to bridge the gap between in-vivo and ex-vivo MRI. Secondly, we performed the analysis on a few regions sparsely sampled from the brain. Though these brain regions were highly relevant for investigating ALS pathology [96], we are still unable to characterise whole-brain MRI-microscopy variations. Lastly, our

MRI-microscopy relationships only draw from density-based microscopy metrics, ignoring the influence of dispersion and cellular morphology on MRI signals.

To overcome these limitations, one could use a mouse model. A mouse model would allow for the high-quality curation of in-vivo MRI, ex-vivo MRI, and IHC data in the same brain, thereby enabling a three-way comparison. Here, ex-vivo MRI would function as the intermediary that possesses the same signal mechanisms as in-vivo MRI, while sharing the same tissue state as IHC. Given enough time and resources, one could also densely sample multiple regions across whole mouse brains. As the automated pipeline is stain- and species-agnostic, the pipeline could process these samples in a high-throughput manner. The pipeline could also be easily extended to compute dispersion metrics by applying structure tensor analysis [33] on the protein structures from the DAB channel. Crucially, the pipeline aims to minimise potential between-slide variations due to IHC staining artefacts through a set of data-driven methods, thereby enabling comparison across slides. Coupled with voxelwise MRI-microscopy co-registrations (as shown in Chapter 4), machine learning models trained on all three sets of data (in-vivo MRI, ex-vivo MRI, IHC-derived metrics) could, in principle, predict multiple IHC-derived metrics given multiple MRI contrast. Some studies are already exploring this avenue, ranging from comprehensive data curation [166] to the use of deep-learning models to predict histological metrics from multi-contrast MRI [134].

A mouse model confers one additional benefit: it allows for hypothesis-driven experiments. For example, one could introduce a genetic mutation encoding an alteration in a specific protein and then investigate how this manifests as an MRI signal change across various time points. The mouse could then be sacrificed and have its brain sectioned and stained for various proteins, bridging the gap between MRI and microscopy. Moreover, the controlled environment in which mice are raised minimises confounding variables, making the measured MRI outcomes more directly attributable to the introduced genetic changes. This level of environmental control is typically unachievable in human studies. On this front, our lab is currently

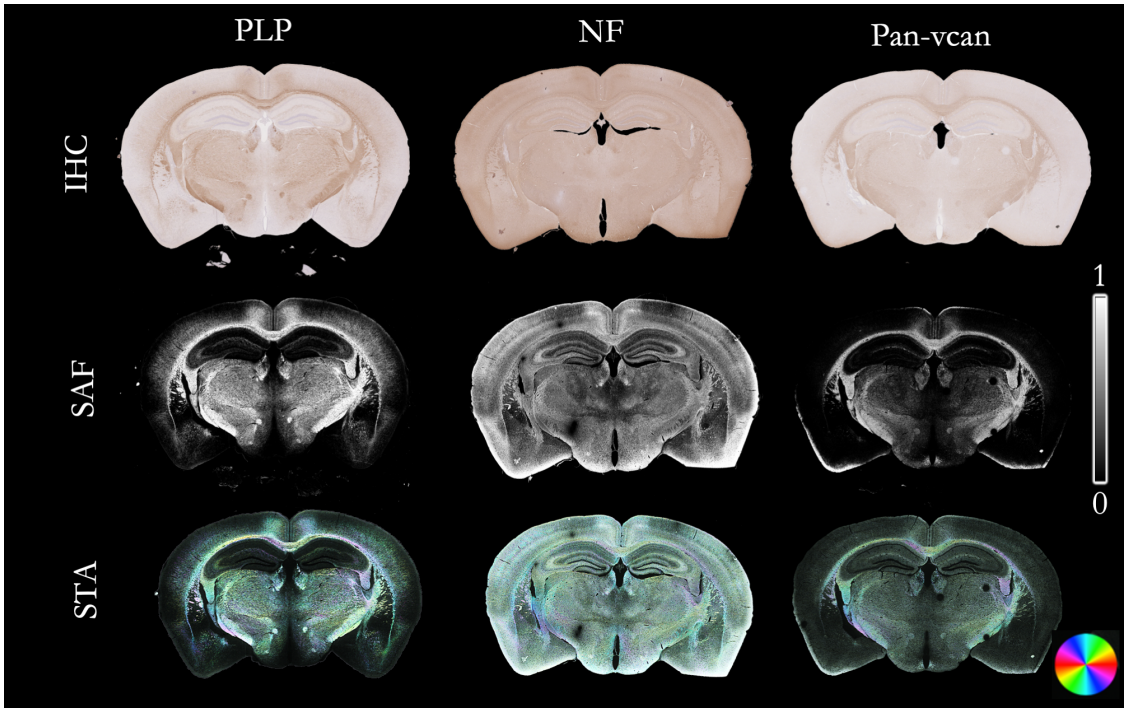

Figure 6.1: The IHC slides (top row), stain area fraction (SAF) maps (middle row) and mean fibre orientation maps (bottom row). The mean fibre orientation maps are displayed as directionally encoded colour maps, where each pixel represents the mean orientation calculated through structure tensor analysis (STA) for a given patch size. The pipeline produces sensible outputs for different stains (columns), such as myelin (PLP) and neurofilament (NF), and versican (Pan-vcan). Pan-vcan represents all versican proteins, which are involved in a diverse range of functions with respect to remyelination and the formation of the axon's extracellular matrix. In the future, one could utilise this pipeline to simultaneously relate multiple densities (i.e. SAF) and dispersion metrics derived from IHC to MRI parameters. These images were provided by Cristiana Tisca [171].

investigating how a genetic mutation affecting an extracellular protein translates into MRI changes [171]. Preliminary strides have already been made. In Figure 6.1, we show some results of how this pipeline has helped facilitate the processing of IHC stains to derive dispersion and density metrics.

Building on the results in Chapter 4, we can use a mouse inflammation model to investigate the notable relationship between DTI's FA and activated microglia density. By employing both microscopy and multimodal MRI, we can identify the specific biophysical mechanisms related to inflammation and clarify which are tied to MRI-visible microstructural changes.

6.1.2 Optimising IHC protocols

The IHC data we analysed were stained for commonly investigated proteins, such as myelin, neurofilament and microglia. As such, our IHC staining protocols were generally well-tested and reliable. However, this may not be the case for many lesser-known proteins, which is especially of interest in many hypothesis-driven studies [171]. Hence, producing reliable IHC data for these proteins still remains a challenge.

The pipeline can be used to optimise IHC protocols to reliably produce IHC data without artefacts. If present, these artefacts may influence the IHC-derived metrics and by extension, MRI-IHC relationships. In this optimisation process, one can first prepare and stain a preliminary batch of sections using an initial IHC protocol. The sections would then be rapidly processed with our automated pipeline. If the slides exhibit noticeable artefacts in the resulting SAF maps, the IHC protocol can be iteratively refined to remove said artefacts for future batches of tissue sections.

6.1.3 Application to other microscopy techniques

The SAF pipeline can be adapted to process data from various microscopy techniques by selectively using specific steps. For instance, data labeled using immunofluorescence or chemical staining, which lacks a counterstain like hematoxylin, would skip the stain separation step. Subsequent steps can still be applied to generate SAF maps. In the case of 3D microscopy techniques, such as CLARITY followed by immunostaining [175], the pipeline could potentially produce SAF maps slice-by-slice. However, the reconstruction of these slices into a 3D volume would require further development and evaluation.

6.1.4 Linking diffusion MRI to different phenotypes in UK Biobank

We have conceptualised, implemented and applied continuous BENCH to investigate our main hypothesis of which diffusion biophysical model parameters relate to microscopy metrics associated with myelin and glial density and organisation. In theory, however, this approach can be used for any continuous metrics that may relate to changes in the dMRI signal. Here, we shift our focus from microscopy to any continuous metric that has been shown to influence brain microstructure.

Clinical studies often first divide people into different groups (e.g. patient populations) and then look at differences between groups. However, this grouping can be challenging, particularly in many clinical disorders (e.g. psychiatric, neurological, vascular), resulting in inhomogeneous groups that lack statistical power. Here, we use continuous BENCH to look directly at the measured clinical variables, which are often continuous in nature. This approach is powerful because this allows us to consider the dynamic range reflected across a large sample size while removing the arbitrary step of grouping samples. Hence, this approach is most effective when applied to a large biomedical database, such as the UK Biobank.

The UK Biobank is a large-scale biomedical database and research resource, containing genetic, clinical, and imaging-derived phenotypes from up to half a million UK participants [176]. Its primary aim is to support a diverse range of research projects to improve the prevention, diagnosis, and treatment of a wide array of illnesses. Crucially, the UK Biobank provides the brain MRI data of more than 44,000 subjects, ensuring sufficient statistical power when drawing conclusions about relationships between MRI-derived parameters and different phenotypes.

Many research projects have benefited from the UK Biobank. This includes the observation of DTI (e.g. FA, MD) and biophysical model parameters (e.g. intra-axonal volume fraction) being linked with multiple clinical phenotypes, such as blood pressure and glycated hemoglobin levels (i.e. blood glucose), in specific brain

regions [177]–[179]. However, most studies were exploratory research focused on finding associations between different clinical phenotypes with dMRI data. As such, they had only used a precomputed set of dMRI-derived parameters [177]. These parameters come from either DTI, NODDI or the ball and sticks model. Though these precomputed parameters have shown sensitivity to different phenotypes, they lack specificity due to the limitations of these models. For example, we may expect a clinical phenotype to be related to glia due to factors relating to inflammation. However, glia may not be explicitly included in the precomputed model parameters due to issues with model degeneracy, as described in Section 2.3.3. We leverage continuous BENCH's ability to circumvent solution degeneracies, allowing access to more complex biophysical models. Here, we aim to more precisely elucidate which biophysical model parameter best explains the observed change in the dMRI signal, as described by clinical phenotypes. In this preliminary study, we first outline the necessary steps to curate UK Biobank data and present early results relating clinical phenotypes to brain dMRI data.

Diffusion MRI to clinical phenotypes

We curated phenotypes from different sub-categories: blood pressure (sub-category ID 10001), blood count (sub-category ID 100081), blood biochemistry (sub-category ID 17518), infectious diseases (sub-category ID 51428), NMR metabolomics (sub-category ID 220), and urine assays (sub-category ID 100083). Some sub-categories were selected due to their known associations with brain dMRI, while some were chosen to explore potential associations. We only selected phenotypes that are continuous variables. The dataset was then cleaned and preprocessed using the FMRIB UK Biobank Normalisation, Parsing And Cleaning Kit (FUNPACK) software [180], ensuring that all NaN values and highly correlated phenotypes were removed. This resulted in a final dataset of 86 phenotypes from 44,011 subjects. All subjects have brain dMRI data.

To apply continuous BENCH to this dataset, we first needed to specify a generative biophysical model to train the change models. We used an extended WM standard model, that included an intra-axonal compartment modelled as dispersed sticks, an extra-cellular compartment characterised as dispersed zeppelins, a CSF compartment represented as a ball, and the intra-soma compartment modelled as a sphere. During training, the baseline signal and change vector were calculated for 30,000 different combinations of input parameters (c.f. Section 5.2.2).

Continuous BENCH also requires us to define an interesting direction of change within the data i.e. the measured change in dMRI signal due to the phenotype-of-interest. For each voxel in standard space, a GLM was set up with the dMRI signal across subjects as the observation/response variable, and the clinical phenotypes as the explanatory variables. To account for confounding effects (e.g. age, sex, site), we also included the full confound dataset as explanatory variables [181]. We performed inference on each voxel in the brain WM, where we output a probability of which biophysical parameter is most likely to change, given a change in the clinical phenotype. We overlaid the JHU DTI-based white-matter atlas to determine the WM regions which were affected [182], [183].

Interesting results were found for many of the 86 phenotypes tested. Here, we present the preliminary results for two clinical phenotypes—systolic blood pressure and glycated haemoglobin—that are already known to explain significant variation in dMRI data in key WM regions [177]–[179]. For systolic blood pressure (Figure 6.2, top row), increasing blood pressure was linked to an increasing extra-axonal radial diffusivity ($D_{r,ex}$) in the corpus callosum. Elevated blood pressure is a known risk factor for hypertension [184]. This implies that hypertension may relate to demyelination in the brain WM due to reduced blood flow to areas of ischemia in WM tracts. An increase in glycated haemoglobin was linked to a decrease in intra-axonal signal fraction (f_{in}) (Figure 6.2, middle and bottom row). In the anterior corona radiata, retrolenticular portion of the internal capsule and the corpus callosum (Figure 6.2, middle row), the decrease in f_{in} is accompanied by

an increase in the signal fraction of the isotropic compartment (f_{iso}), suggesting possible microstructural changes relating to axonal degeneration and/or edema. In parts of the retrolenticular portion of the internal capsule and the cingulum bundle, we observed the decrease in f_{in} alongside an increase in the sphere compartment signal fraction (f_{sph}). This may indicate neuroinflammation and may relate to the increased proliferation of glial cells following axonal degeneration. Together, our preliminary results demonstrate the use of continuous BENCH in clinical studies that seek to relate key biomarkers (e.g. glycated haemoglobin) of diseases (e.g. diabetes) to specific brain microstructural changes. For the remaining 84 phenotypes, we aim to perform similar analyses, cross-referencing with the literature on known links between phenotypes and microstructural changes. In the process, we might also uncover new associations.

Thus far, we have only considered non-imaging derived phenotypes. There is also a growing interest in adopting a multi-organ approach for disease prevention, driven by the understanding that many diseases share common risk factors across different organ systems [185]. Hence, another promising avenue would be to use continuous BENCH to link imaging-derived phenotypes (IDP) from different organs to one another e.g. brain and cardiac IDPs.

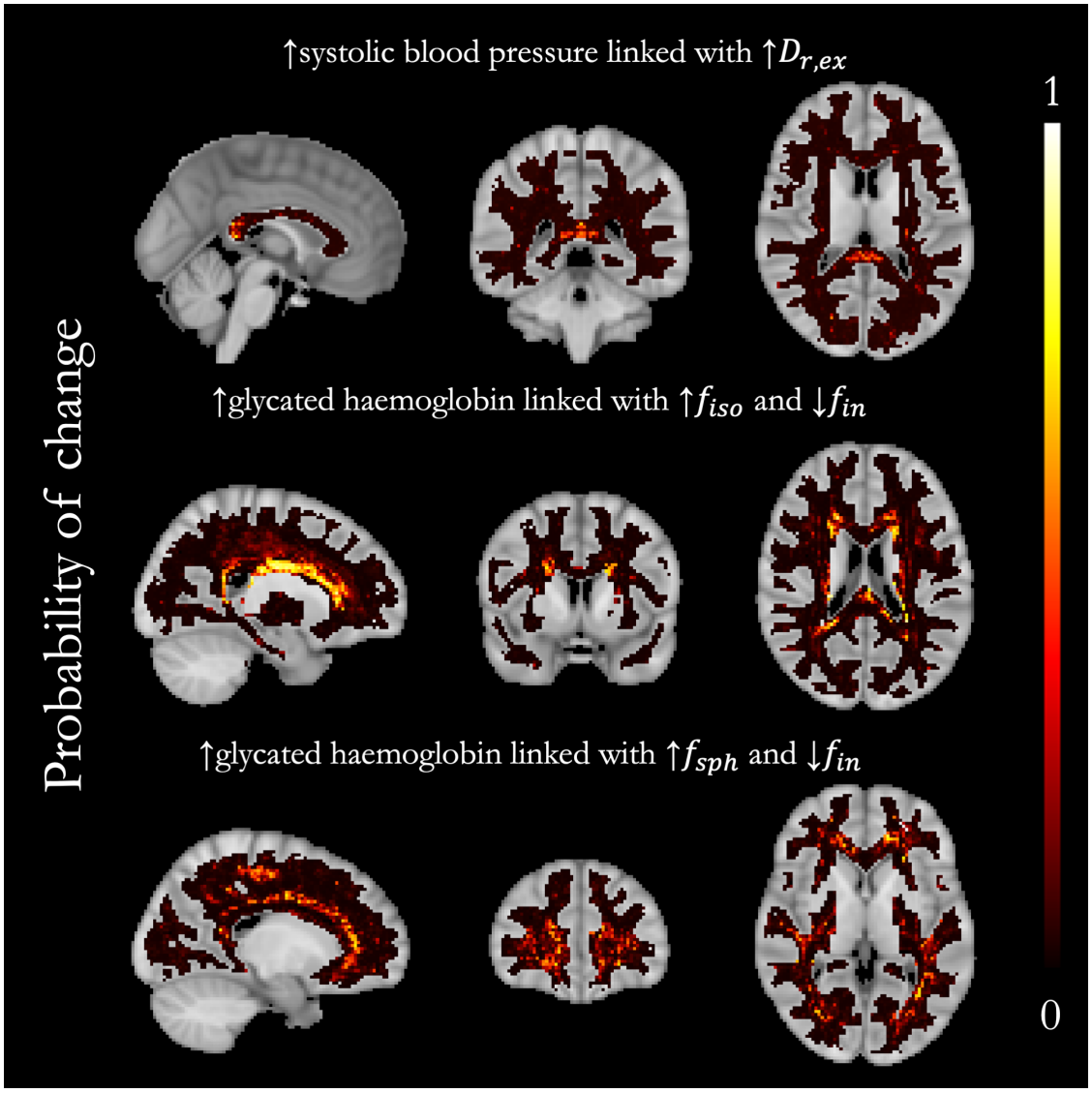

Figure 6.2: Preliminary results when linking two example clinical phenotypes—systolic blood pressure (top row), glycated haemoglobin (mid and bottom row)—to biophysical model parameters.

Originality is nothing but judicious imitation.

— Voltaire

References

[1] G. K. York and D. A. Steinberg, "Chapter 3: Neurology in ancient Egypt," eng, *Handbook of Clinical Neurology*, vol. 95, pp. 29–36, 2010.

[2] M. Glickstein, "Golgi and Cajal: The neuron doctrine and the 100th anniversary of the 1906 Nobel Prize," English, *Current Biology*, vol. 16, no. 5, R147–R151, Mar. 2006, Publisher: Elsevier. [Online]. Available: https://www.cell.com/current-biology/abstract/S0960-9822(06)01203-6 (visited on 09/19/2023).

[3] K. Brodmann, *Vergleichende Lokalisationslehre der Grosshirnrinde in ihren Prinzipien dargestellt auf Grund des Zellenbaues*, ger. Leipzig: Johann Ambrosius Barth, 1909, OCLC: 645157545.

[4] D. B. Schmolze, C. Standley, K. E. Fogarty, and A. H. Fischer, "Advances in microscopy techniques," eng, *Archives of Pathology & Laboratory Medicine*, vol. 135, no. 2, pp. 255–263, Feb. 2011.

[5] R. E. Gordon, "Electron microscopy: A brief history and review of current clinical application," eng, *Methods in Molecular Biology (Clifton, N.J.)*, vol. 1180, pp. 119–135, 2014.

[6] J. H. Stonard, *Bancroft's Theory and Practice of Histological Techniques (Seventh Edition)*, Seventh Edition, S. K. Suvarna, C. Layton, and J. D. Bancroft, Eds. Oxford: Churchill Livingstone, 2013, pp. 587–588. [Online]. Available: https://www.sciencedirect.com/science/article/pii/B978070204226300024X.

[7] P. Dreizen, "The Nobel prize for MRI: A wonderful discovery and a sad controversy," English, *The Lancet*, vol. 363, no. 9402, p. 78, Jan. 2004, Publisher: Elsevier. [Online]. Available: https://www.thelancet.com/journals/lancet/article/PIIS0140-6736(03)15182-3/fulltext (visited on 09/19/2023).

[8] L. J. Edwards, E. Kirilina, S. Mohammadi, and N. Weiskopf, "Microstructural imaging of human neocortex in vivo," eng, *NeuroImage*, vol. 182, pp. 184–206, Nov. 2018.

[9] C. Granziera, J. Wuerfel, F. Barkhof, *et al.*, "Quantitative magnetic resonance imaging towards clinical application in multiple sclerosis," *Brain*, vol. 144, no. 5, pp. 1296–1311, May 2021. [Online]. Available: https://doi.org/10.1093/brain/awab029 (visited on 10/18/2021).

[10] C. Beaulieu, "The basis of anisotropic water diffusion in the nervous system - a technical review," eng, *NMR in biomedicine*, vol. 15, no. 7-8, pp. 435–455, 2002.

[11] I. O. Jelescu and E. Fieremans, "Chapter 2 - Sensitivity and specificity of diffusion MRI to neuroinflammatory processes," in *Advances in Magnetic Resonance Technology and Applications*, ser. Imaging Neuroinflammation, C. Laule and J. D. Port, Eds., vol. 9, Academic Press, Jan. 2023, pp. 31–50. [Online]. Available: https://www.sciencedirect.com/science/article/pii/B9780323917711000101 (visited on 12/25/2023).

[12] U. Ndubaku and M. E. de Bellard, "Glial cells: Old cells with new twists," *Acta histochemica*, vol. 110, no. 3, pp. 182–195, 2008. [Online]. Available: https://www.ncbi.nlm.nih.gov/pmc/articles/PMC2365468/ (visited on 09/19/2023).

[13] W. a. H. Rushton, "A theory of the effects of fibre size in medullated nerve," en, *The Journal of Physiology*, vol. 115, no. 1, pp. 101–122, 1951, _eprint: https://onlinelibrary.wiley.com/doi/pdf/10.1113/jphysiol.1951.sp004655. [Online]. Available: https://onlinelibrary.wiley.com/doi/abs/10.1113/jphysiol.1951.sp004655 (visited on 09/19/2023).

[14] S. G. Waxman and M. V. L. Bennett, "Relative Conduction Velocities of Small Myelinated and Non-myelinated Fibres in the Central Nervous System," en, *Nature New Biology*, vol. 238, no. 85, pp. 217–219, Aug. 1972, Number: 85 Publisher: Nature Publishing Group. [Online]. Available: https://www.nature.com/articles/newbio238217a0 (visited on 09/19/2023).

[15] T. Hirano, "Purkinje Neurons: Development, Morphology, and Function," en, *The Cerebellum*, vol. 17, no. 6, pp. 699–700, Dec. 2018. [Online]. Available: https://doi.org/10.1007/s12311-018-0985-7 (visited on 09/19/2023).

[16] B. A. Barres, "The Mystery and Magic of Glia: A Perspective on Their Roles in Health and Disease," English, *Neuron*, vol. 60, no. 3, pp. 430–440, Nov. 2008, Publisher: Elsevier. [Online]. Available: https://www.cell.com/neuron/abstract/S0896-6273(08)00886-6 (visited on 09/19/2023).

[17] N. Baumann and D. Pham-Dinh, "Biology of Oligodendrocyte and Myelin in the Mammalian Central Nervous System," *Physiological Reviews*, vol. 81, no. 2, pp. 871–927, Apr. 2001, Publisher: American Physiological Society. [Online]. Available: https://journals.physiology.org/doi/full/10.1152/physrev.2001.81.2.871 (visited on 09/19/2023).

[18] D. E. Korzhevskii and O. V. Kirik, "Brain Microglia and Microglial Markers," en, *Neuroscience and Behavioral Physiology*, vol. 46, no. 3, pp. 284–290, Mar. 2016. [Online]. Available: https://doi.org/10.1007/s11055-016-0231-z (visited on 08/30/2022).

[19] W. J. Streit, "Microglia as neuroprotective, immunocompetent cells of the CNS," en, *Glia*, vol. 40, no. 2, pp. 133–139, 2002, _eprint: https://onlinelibrary.wiley.com/doi/pdf/10.1002/glia.10154. [Online]. Available: https://onlinelibrary.wiley.com/doi/abs/10.1002/glia.10154 (visited on 09/19/2023).

[20] E. L. House and B. Pansky, "A Functional Approach to Neuroanatomy," en-US, *Academic Medicine*, vol. 35, no. 11, p. 1067, Nov. 1960. [Online]. Available: https://journals.lww.com/academicmedicine/citation/1960/11000/a_functional_approach_to_neuroanatomy.27.aspx (visited on 09/22/2023).

[21] A. Yendiki, M. Aggarwal, M. Axer, A. F. D. Howard, A.-M. v. C. van Walsum, and S. N. Haber, "Post mortem mapping of connectional anatomy for the validation of diffusion MRI," *NeuroImage*, vol. 256, p. 119 146, Aug. 2022. [Online]. Available: https://www.sciencedirect.com/science/article/pii/S1053811922002737 (visited on 09/19/2023).

[22] A. Lazari and I. Lipp, "Can MRI measure myelin? Systematic review, qualitative assessment, and meta-analysis of studies validating microstructural imaging with myelin histology," en, *NeuroImage*, vol. 230, p. 117 744, Apr. 2021. [Online]. Available: https://www.sciencedirect.com/science/article/pii/S1053811921000215 (visited on 12/29/2021).

[23] A. De Barros, G. Arribarat, J. Combis, P. Chaynes, and P. Péran, "Matching ex vivo MRI With Iron Histology: Pearls and Pitfalls," *Frontiers in Neuroanatomy*, vol. 13, 2019. [Online]. Available: https://www.frontiersin.org/article/10.3389/fnana.2019.00068 (visited on 01/18/2022).

[24] C. M. van der Loos, "Multiple immunoenzyme staining: Methods and visualizations for the observation with spectral imaging," eng, *The Journal of Histochemistry and Cytochemistry: Official Journal of the Histochemistry Society*, vol. 56, no. 4, pp. 313–328, Apr. 2008.

[25] A. C. Ruifrok and D. A. Johnston, "Quantification of histochemical staining by color deconvolution," eng, *Analytical and Quantitative Cytology and Histology*, vol. 23, no. 4, pp. 291–299, Aug. 2001.

[26] S. Wharton and R. Bowtell, "Fiber orientation-dependent white matter contrast in gradient echo MRI," eng, *Proceedings of the National Academy of Sciences of the United States of America*, vol. 109, no. 45, pp. 18 559–18 564, Nov. 2012.

[27] C. Langkammer, F. Schweser, N. Krebs, *et al.*, "Quantitative susceptibility mapping (QSM) as a means to measure brain iron? A post mortem validation study," eng, *NeuroImage*, vol. 62, no. 3, pp. 1593–1599, Sep. 2012.

[28] D. Kor, C. Birkl, S. Ropele, *et al.*, "The role of iron and myelin in orientation dependent R2* of white matter," eng, *NMR in biomedicine*, vol. 32, no. 7, e4092, Jul. 2019.

[29] S. Hametner, V. Endmayr, A. Deistung, *et al.*, "The influence of brain iron and myelin on magnetic susceptibility and effective transverse relaxation - A biochemical and histological validation study," eng, *NeuroImage*, vol. 179, pp. 117–133, Oct. 2018.

[30] M. Tolcos, D. H. Rowitch, and J. Dean, "Oligodendrocytes: Cells of Origin for White Matter Injury in the Developing Brain," en, in *Prenatal and Postnatal Determinants of Development*, ser. Neuromethods, D. W. Walker, Ed., New York, NY: Springer, 2016, pp. 281–301. [Online]. Available: https://doi.org/10.1007/978-1-4939-3014-2_14 (visited on 09/16/2023).

[31] J. Warntjes, A. Persson, J. Berge, and W. Zech, "Myelin Detection Using Rapid Quantitative MR Imaging Correlated to Macroscopically Registered Luxol Fast Blue–Stained Brain Specimens," *AJNR: American Journal of Neuroradiology*, vol. 38, no. 6, pp. 1096–1102, Jun. 2017. [Online]. Available: https://www.ncbi.nlm.nih.gov/pmc/articles/PMC7960095/ (visited on 12/29/2021).

[32] J. Mollink, M. Hiemstra, K. L. Miller, *et al.*, "White matter changes in the perforant path area in patients with amyotrophic lateral sclerosis," eng, *Neuropathology and Applied Neurobiology*, vol. 45, no. 6, pp. 570–585, Oct. 2019.

[33] M. D. Budde and J. A. Frank, "Examining brain microstructure using structure tensor analysis of histological sections," eng, *NeuroImage*, vol. 63, no. 1, pp. 1–10, Oct. 2012.

[34] V. Mlynárik, "Introduction to nuclear magnetic resonance," *Analytical Biochemistry*, Introduction to in vivo Magnetic Resonance Spectroscopy (MRS): A method to non-invasively study metabolism, vol. 529, pp. 4–9, Jul. 2017. [Online]. Available: https://www.sciencedirect.com/science/article/pii/S0003269716300719 (visited on 09/19/2023).

[35] L. G. Hanson, "Is quantum mechanics necessary for understanding magnetic resonance?" en, *Concepts in Magnetic Resonance Part A*, vol. 32A, no. 5, pp. 329–340, 2008, _eprint: https://onlinelibrary.wiley.com/doi/pdf/10.1002/cmr.a.20123. [Online]. Available: https://onlinelibrary.wiley.com/doi/abs/10.1002/cmr.a.20123 (visited on 09/19/2023).

[36] F. Bloch, "Nuclear Induction," *Physical Review*, vol. 70, no. 7-8, pp. 460–474, Oct. 1946, Publisher: American Physical Society. [Online]. Available: https://link.aps.org/doi/10.1103/PhysRev.70.460 (visited on 09/19/2023).

[37] J. Keeler, "Understanding nmr spectroscopy," 2002. [Online]. Available: https://www.repository.cam.ac.uk/handle/1810/257040.

[38] G. B. Chavhan, P. S. Babyn, B. Thomas, M. M. Shroff, and E. M. Haacke, "Principles, techniques, and applications of T2*-based MR imaging and its special applications," eng, *Radiographics: A Review Publication of the Radiological Society of North America, Inc*, vol. 29, no. 5, pp. 1433–1449, 2009.

[39] E. L. Hahn, "An Accurate Nuclear Magnetic Resonance Method for Measuring Spin-Lattice Relaxation Times," *Physical Review*, vol. 76, no. 1, pp. 145–146, Jul. 1949, Publisher: American Physical Society. [Online]. Available: https://link.aps.org/doi/10.1103/PhysRev.76.145 (visited on 09/19/2023).

[40] H. Y. Carr and E. M. Purcell, "Effects of Diffusion on Free Precession in Nuclear Magnetic Resonance Experiments," *Physical Review*, vol. 94, no. 3, pp. 630–638, May 1954, Publisher: American Physical Society. [Online]. Available: https://link.aps.org/doi/10.1103/PhysRev.94.630 (visited on 09/19/2023).

[41] A. D. Elster, "Gradient-echo MR imaging: Techniques and acronyms," eng, *Radiology*, vol. 186, no. 1, pp. 1–8, Jan. 1993.

[42] C. W. J. van der Weijden, D. V. García, R. J. H. Borra, *et al.*, "Myelin quantification with MRI: A systematic review of accuracy and reproducibility," eng, *NeuroImage*, vol. 226, p. 117 561, Feb. 2021.

[43] N. Gelman, J. R. Ewing, J. M. Gorell, E. M. Spickler, and E. G. Solomon, "Interregional variation of longitudinal relaxation rates in human brain at 3.0 T: Relation to estimated iron and water contents," en, *Magnetic Resonance in Medicine*, vol. 45, no. 1, pp. 71–79, 2001, _eprint: https://onlinelibrary.wiley.com/doi/pdf/10.1002/1522-2594%28200101%2945%3A1%3C71%3A%3AAID-MRM1011%3E3.0.CO%3B2-2. [Online]. Available: https://onlinelibrary.wiley.com/doi/abs/10.1002/1522-2594%28200101%2945%3A1%3C71%3A%3AAID-MRM1011%3E3.0.CO%3B2-2 (visited on 09/19/2023).

[44] C. Laule, I. M. Vavasour, S. H. Kolind, *et al.*, "Magnetic resonance imaging of myelin," eng, *Neurotherapeutics: The Journal of the American Society for Experimental NeuroTherapeutics*, vol. 4, no. 3, pp. 460–484, Jul. 2007.

[45] C. Stüber, M. Morawski, A. Schäfer, *et al.*, "Myelin and iron concentration in the human brain: A quantitative study of MRI contrast," eng, *NeuroImage*, vol. 93 Pt 1, pp. 95–106, Jun. 2014.

[46] A. Lutti, F. Dick, M. I. Sereno, and N. Weiskopf, "Using high-resolution quantitative mapping of R1 as an index of cortical myelination," eng, *NeuroImage*, vol. 93 Pt 2, pp. 176–188, Jun. 2014.

[47] F. Dick, A. T. Tierney, A. Lutti, O. Josephs, M. I. Sereno, and N. Weiskopf, "In vivo functional and myeloarchitectonic mapping of human primary auditory areas," eng, *The Journal of Neuroscience: The Official Journal of the Society for Neuroscience*, vol. 32, no. 46, pp. 16 095–16 105, Nov. 2012.

[48] M. I. Sereno, A. Lutti, N. Weiskopf, and F. Dick, "Mapping the human cortical surface by combining quantitative T(1) with retinotopy," eng, *Cerebral Cortex (New York, N.Y.: 1991)*, vol. 23, no. 9, pp. 2261–2268, Sep. 2013.

[49] C. Langkammer, N. Krebs, W. Goessler, *et al.*, "Quantitative MR Imaging of Brain Iron: A Postmortem Validation Study," *Radiology*, vol. 257, no. 2, pp. 455–462, Nov. 2010, Publisher: Radiological Society of North America. [Online]. Available: https://pubs.rsna.org/doi/full/10.1148/radiol.10100495 (visited on 02/08/2022).

[50] J. Cohen-Adad, J. R. Polimeni, K. G. Helmer, *et al.*, "T2* mapping and B0 orientation-dependence at 7T reveal cyto- and myeloarchitecture organization of the human cortex," *NeuroImage*, vol. 60, no. 2, pp. 1006–1014, Apr. 2012. [Online]. Available: https://www.sciencedirect.com/science/article/pii/S1053811912000705 (visited on 09/19/2023).

[51] N. Gelman, J. M. Gorell, P. B. Barker, *et al.*, "MR imaging of human brain at 3.0 T: Preliminary report on transverse relaxation rates and relation to estimated iron content," eng, *Radiology*, vol. 210, no. 3, pp. 759–767, Mar. 1999.

[52] P. A. Hardy, D. Gash, R. Yokel, A. Andersen, Y. Ai, and Z. Zhang, "Correlation of R2 with total iron concentration in the brains of rhesus monkeys," eng, *Journal of magnetic resonance imaging: JMRI*, vol. 21, no. 2, pp. 118–127, Feb. 2005.

[53] I. M. Vavasour, K. P. Whittall, A. L. MacKay, D. K. Li, G. Vorobeychik, and D. W. Paty, "A comparison between magnetization transfer ratios and myelin water percentages in normals and multiple sclerosis patients," eng, *Magnetic Resonance in Medicine*, vol. 40, no. 5, pp. 763–768, Nov. 1998.

[54] G. R. Moore, E. Leung, A. L. MacKay, *et al.*, "A pathology-MRI study of the short-T2 component in formalin-fixed multiple sclerosis brain," eng, *Neurology*, vol. 55, no. 10, pp. 1506–1510, Nov. 2000.

[55] A. MacKay, C. Laule, I. Vavasour, T. Bjarnason, S. Kolind, and B. Mädler, "Insights into brain microstructure from the T2 distribution," eng, *Magnetic Resonance Imaging*, vol. 24, no. 4, pp. 515–525, May 2006.

[56] H. Johansen-Berg and T. E. J. Behrens, *Diffusion MRI: From Quantitative Measurement to In-Vivo Neuroanatomy*, 2nd. London, UK: Academic Press, 2014.

[57] A. Einstein, "Über die von der molekularkinetischen Theorie der Wärme geforderte Bewegung von in ruhenden Flüssigkeiten suspendierten Teilchen," en, *Annalen der Physik*, vol. 322, no. 8, pp. 549–560, 1905, _eprint: https://onlinelibrary.wiley.com/doi/pdf/10.1002/andp.19053220806. [Online]. Available: https://onlinelibrary.wiley.com/doi/abs/10.1002/andp.19053220806 (visited on 09/19/2023).

[58] E. W. Woolard, "Review of Investigations on the Theory of the Brownian Movement.," *The American Mathematical Monthly*, vol. 35, no. 6, pp. 318–320, 1928, Publisher: Mathematical Association of America. [Online]. Available: https://www.jstor.org/stable/2298685 (visited on 09/19/2023).

[59] D. S. Novikov, E. Fieremans, S. N. Jespersen, and V. G. Kiselev, "Quantifying brain microstructure with diffusion MRI: Theory and parameter estimation," en, *NMR in Biomedicine*, vol. 32, no. 4, e3998, 2019, _eprint: https://onlinelibrary.wiley.com/doi/pdf/10.1002/nbm.3998. [Online]. Available: https://onlinelibrary.wiley.com/doi/abs/10.1002/nbm.3998 (visited on 11/01/2022).

[60] P. J. Basser, J. Mattiello, and D. LeBihan, "MR diffusion tensor spectroscopy and imaging," eng, *Biophysical Journal*, vol. 66, no. 1, pp. 259–267, Jan. 1994.

[61] A. L. Alexander, J. E. Lee, M. Lazar, and A. S. Field, "Diffusion Tensor Imaging of the Brain," *Neurotherapeutics*, Advances in Neuroimaging/Neuroethics, vol. 4, no. 3, pp. 316–329, Jul. 2007. [Online]. Available: https://www.sciencedirect.com/science/article/pii/S1878747923006530 (visited on 09/19/2023).

[62] M. W. A. Caan, H. G. Khedoe, D. H. J. Poot, *et al.*, "Estimation of Diffusion Properties in Crossing Fiber Bundles," *IEEE Transactions on Medical Imaging*, vol. 29, no. 8, pp. 1504–1515, Aug. 2010, Conference Name: IEEE Transactions on Medical Imaging.

[63] D. S. Novikov, J. Veraart, I. O. Jelescu, and E. Fieremans, "Rotationally-invariant mapping of scalar and orientational metrics of neuronal microstructure with diffusion MRI," *NeuroImage*, vol. 174, pp. 518–538, Jul. 2018. [Online]. Available: https://www.sciencedirect.com/science/article/pii/S1053811918301915 (visited on 09/19/2023).

[64] H. Zhang, T. Schneider, C. A. Wheeler-Kingshott, and D. C. Alexander, "NODDI: Practical in vivo neurite orientation dispersion and density imaging of the human brain," eng, *NeuroImage*, vol. 61, no. 4, pp. 1000–1016, Jul. 2012.

[65] I. O. Jelescu, M. Palombo, F. Bagnato, and K. G. Schilling, "Challenges for biophysical modeling of microstructure," *Journal of Neuroscience Methods*, vol. 344, p. 108 861, Oct. 2020. [Online]. Available: https://www.sciencedirect.com/science/article/pii/S0165027020302843 (visited on 09/19/2023).

[66] S. Coelho, J. M. Pozo, S. N. Jespersen, D. K. Jones, and A. F. Frangi, "Resolving degeneracy in diffusion MRI biophysical model parameter estimation using double diffusion encoding," eng, *Magnetic Resonance in Medicine*, vol. 82, no. 1, pp. 395–410, Jul. 2019.

[67] B. Lampinen, F. Szczepankiewicz, J. Mårtensson, *et al.*, "Towards unconstrained compartment modeling in white matter using diffusion-relaxation MRI with tensor-valued diffusion encoding," en, *Magnetic Resonance in Medicine*, vol. 84, no. 3, pp. 1605–1623, 2020, _eprint: https://onlinelibrary.wiley.com/doi/pdf/10.1002/mrm.28216. [Online]. Available: https://onlinelibrary.wiley.com/doi/abs/10.1002/mrm.28216 (visited on 09/21/2023).

[68] M. Reisert, V. G. Kiselev, and B. Dhital, "A unique analytical solution of the white matter standard model using linear and planar encodings," eng, *Magnetic Resonance in Medicine*, vol. 81, no. 6, pp. 3819–3825, Jun. 2019.

[69] I. O. Jelescu, J. Veraart, E. Fieremans, and D. S. Novikov, "Degeneracy in model parameter estimation for multi-compartmental diffusion in neuronal tissue," *NMR in biomedicine*, vol. 29, no. 1, pp. 33–47, Jan. 2016. [Online]. Available: https://www.ncbi.nlm.nih.gov/pmc/articles/PMC4920129/ (visited on 11/01/2022).

[70] M. Reisert, E. Kellner, B. Dhital, J. Hennig, and V. G. Kiselev, "Disentangling micro from mesostructure by diffusion MRI: A Bayesian approach," *NeuroImage*, vol. 147, pp. 964–975, Feb. 2017. [Online]. Available: https://www.sciencedirect.com/science/article/pii/S1053811916305353 (visited on 09/19/2023).

[71] B. Lampinen, F. Szczepankiewicz, M. Novén, *et al.*, "Searching for the neurite density with diffusion MRI: Challenges for biophysical modeling," en, *Human Brain Mapping*, vol. 40, no. 8, pp. 2529–2545, 2019, _eprint: https://onlinelibrary.wiley.com/doi/pdf/10.1002/hbm.24542. [Online]. Available: https://onlinelibrary.wiley.com/doi/abs/10.1002/hbm.24542 (visited on 09/19/2023).

[72] A. F. Howard, M. Cottaar, M. Drakesmith, *et al.*, "Estimating axial diffusivity in the NODDI model," eng, *NeuroImage*, vol. 262, p. 119 535, Nov. 2022.

[73] M. Palombo, A. Ianus, M. Guerreri, *et al.*, "SANDI: A compartment-based model for non-invasive apparent soma and neurite imaging by diffusion MRI," *NeuroImage*, vol. 215, p. 116 835, Jul. 2020. [Online]. Available: https://www.sciencedirect.com/science/article/pii/S1053811920303220 (visited on 09/20/2023).

[74] R. Garcia-Hernandez, A. Cerdán Cerdá, A. Trouve Carpena, *et al.*, "Mapping microglia and astrocyte activation in vivo using diffusion MRI," eng, *Science Advances*, vol. 8, no. 21, eabq2923, May 2022.

[75] B. Balinov, B. Jonsson, P. Linse, and O. Soderman, "The NMR Self-Diffusion Method Applied to Restricted Diffusion. Simulation of Echo Attenuation from Molecules in Spheres and between Planes," *Journal of Magnetic Resonance, Series A*, vol. 104, no. 1, pp. 17–25, Aug. 1993. [Online]. Available: https://www.sciencedirect.com/science/article/pii/S1064185883711848 (visited on 09/19/2023).

[76] G. J. Stanisz, G. A. Wright, R. M. Henkelman, and A. Szafer, "An analytical model of restricted diffusion in bovine optic nerve," en, *Magnetic Resonance in Medicine*, vol. 37, no. 1, pp. 103–111, 1997, _eprint: https://onlinelibrary.wiley.com/doi/pdf/10.1002/mrm.1910370115. [Online]. Available: https://onlinelibrary.wiley.com/doi/abs/10.1002/mrm.1910370115 (visited on 11/01/2022).

[77] C. H. Neuman, "Spin echo of spins diffusing in a bounded medium," *The Journal of Chemical Physics*, vol. 60, no. 11, pp. 4508–4511, Aug. 2003. [Online]. Available: https://doi.org/10.1063/1.1680931 (visited on 09/19/2023).

[78] B. Dhital, E. Kellner, V. G. Kiselev, and M. Reisert, "The absence of restricted water pool in brain white matter," eng, *NeuroImage*, vol. 182, pp. 398–406, Nov. 2018.

[79] C. M. Tax, F. Szczepankiewicz, M. Nilsson, and D. K. Jones, "The dot-compartment revealed? Diffusion MRI with ultra-strong gradients and spherical tensor encoding in the living human brain," *Neuroimage*, vol. 210, p. 116 534, Apr. 2020. [Online]. Available: https://www.ncbi.nlm.nih.gov/pmc/articles/PMC7429990/ (visited on 09/19/2023).

[80] D. C. Alexander, P. L. Hubbard, M. G. Hall, *et al.*, "Orientationally invariant indices of axon diameter and density from diffusion MRI," en, *NeuroImage*, vol. 52, no. 4, pp. 1374–1389, Oct. 2010. [Online]. Available: https://www.sciencedirect.com/science/article/pii/S1053811910007755 (visited on 08/01/2022).

[81] E. Panagiotaki, H. Fonteijn, B. Siow, *et al.*, "Two-compartment models of the diffusion MR signal in brain white matter," eng, *Medical image computing and computer-assisted intervention: MICCAI ... International Conference on Medical Image Computing and Computer-Assisted Intervention*, vol. 12, no. Pt 1, pp. 329–336, 2009.

[82] J. Veraart, D. Nunes, and N. Shemesh, "Detecting temperature-driven microstructural modulations in tissue using diffusion mri," in *Proceedings of the 31st Annual Meeting of the ISMRM*, Toronto, Canada, 2023.

[83] K. A. Johnson, N. C. Fox, R. A. Sperling, and W. E. Klunk, "Brain Imaging in Alzheimer Disease," *Cold Spring Harbor Perspectives in Medicine*, vol. 2, no. 4, a006213, Apr. 2012. [Online]. Available: `https://www.ncbi.nlm.nih.gov/pmc/articles/PMC3312396/` (visited on 01/18/2022).

[84] R. Geraldes, O. Ciccarelli, F. Barkhof, *et al.*, "The current role of MRI in differentiating multiple sclerosis from its imaging mimics," eng, *Nature Reviews. Neurology*, vol. 14, no. 4, pp. 199–213, Apr. 2018.

[85] G. Grolez, C. Moreau, V. Danel-Brunaud, *et al.*, "The value of magnetic resonance imaging as a biomarker for amyotrophic lateral sclerosis: A systematic review," *BMC Neurology*, vol. 16, no. 1, p. 155, Aug. 2016. [Online]. Available: `https://www.ncbi.nlm.nih.gov/pmc/articles/PMC5002331/` (visited on 01/18/2022).

[86] K.-A. Nave and H. B. Werner, "Myelination of the Nervous System: Mechanisms and Functions," *Annual Review of Cell and Developmental Biology*, vol. 30, no. 1, pp. 503–533, 2014, _eprint: https://doi.org/10.1146/annurev-cellbio-100913-013101. [Online]. Available: `https://doi.org/10.1146/annurev-cellbio-100913-013101` (visited on 08/30/2022).

[87] R. Barker, D. Wellington, M. M. Esiri, and S. Love, "Assessing white matter ischemic damage in dementia patients by measurement of myelin proteins," *Journal of Cerebral Blood Flow & Metabolism*, vol. 33, no. 7, pp. 1050–1057, Jul. 2013. [Online]. Available: `https://www.ncbi.nlm.nih.gov/pmc/articles/PMC3705431/` (visited on 08/30/2022).

[88] N. Ulfig, J. Nickel, and J. Bohl, "Monoclonal antibodies SMI 311 and SMI 312 as tools to investigate the maturation of nerve cells and axonal patterns in human fetal brain," eng, *Cell and Tissue Research*, vol. 291, no. 3, pp. 433–443, Mar. 1998.

[89] A. Atik, J. Cheong, R. Harding, S. Rees, R. De Matteo, and M. Tolcos, "Impact of daily high-dose caffeine exposure on developing white matter of the immature ovine brain," en, *Pediatric Research*, vol. 76, no. 1, pp. 54–63, Jul. 2014, Number: 1 Publisher: Nature Publishing Group. [Online]. Available: `https://www.nature.com/articles/pr201455` (visited on 08/30/2022).

[90] L. Schirmer, J. P. Antel, W. Brück, and C. Stadelmann, "Axonal loss and neurofilament phosphorylation changes accompany lesion development and clinical progression in multiple sclerosis," eng, *Brain Pathology (Zurich, Switzerland)*, vol. 21, no. 4, pp. 428–440, Jul. 2011.

[91] A. M. Jurga, M. Paleczna, and K. Z. Kuter, "Overview of General and Discriminating Markers of Differential Microglia Phenotypes," *Frontiers in Cellular Neuroscience*, vol. 14, 2020. [Online]. Available: https://www.frontiersin.org/articles/10.3389/fncel.2020.00198 (visited on 08/30/2022).

[92] F. Bagnato, S. Hametner, B. Yao, *et al.*, "Tracking iron in multiple sclerosis: A combined imaging and histopathological study at 7 Tesla," *Brain*, vol. 134, no. 12, pp. 3599–3612, Dec. 2011. [Online]. Available: https://www.ncbi.nlm.nih.gov/pmc/articles/PMC3235560/ (visited on 08/30/2022).

[93] R. Waller, L. Baxter, D. J. Fillingham, *et al.*, "Iba-1-/CD68+ microglia are a prominent feature of age-associated deep subcortical white matter lesions," en, *PLOS ONE*, vol. 14, no. 1, e0210888, Jan. 2019, Publisher: Public Library of Science. [Online]. Available: https://journals.plos.org/plosone/article?id=10.1371/journal.pone.0210888 (visited on 08/30/2022).

[94] S. Bachiller, I. Jiménez-Ferrer, A. Paulus, *et al.*, "Microglia in Neurological Diseases: A Road Map to Brain-Disease Dependent-Inflammatory Response," *Frontiers in Cellular Neuroscience*, vol. 12, p. 488, 2018. [Online]. Available: https://www.frontiersin.org/article/10.3389/fncel.2018.00488 (visited on 12/22/2021).

[95] M. C. Geloso, V. Corvino, E. Marchese, A. Serrano, F. Michetti, and N. D'Ambrosi, "The Dual Role of Microglia in ALS: Mechanisms and Therapeutic Approaches," *Frontiers in Aging Neuroscience*, vol. 9, p. 242, 2017. [Online]. Available: https://www.frontiersin.org/article/10.3389/fnagi.2017.00242 (visited on 01/10/2022).

[96] M. Pallebage-Gamarallage, S. Foxley, R. A. L. Menke, *et al.*, "Dissecting the pathobiology of altered MRI signal in amyotrophic lateral sclerosis: A post mortem whole brain sampling strategy for the integration of ultra-high-field MRI and quantitative neuropathology," eng, *BMC neuroscience*, vol. 19, no. 1, p. 11, Mar. 2018.

[97] B. C. Tendler, T. Hanayik, O. Ansorge, *et al.*, "The Digital Brain Bank, an open access platform for post-mortem imaging datasets," *eLife*, vol. 11, A. Fornito, C. Büchel, I. Lipp, K. Wagstyl, and T. Dickscheid, Eds., e73153, Mar. 2022, Publisher: eLife Sciences Publications, Ltd. [Online]. Available: https://doi.org/10.7554/eLife.73153 (visited on 09/21/2023).

[98] M. Goubran, R. R. Hammond, S. de Ribaupierre, *et al.*, "Magnetic resonance imaging and histology correlation in the neocortex in temporal lobe epilepsy," eng, *Annals of Neurology*, vol. 77, no. 2, pp. 237–250, Feb. 2015.

[99] S. Fjær, L. Bø, A. Lundervold, *et al.*, "Deep Gray Matter Demyelination Detected by Magnetization Transfer Ratio in the Cuprizone Model," en, *PLOS ONE*, vol. 8, no. 12, e84162, Dec. 2013, Publisher: Public Library of Science. [Online]. Available: https://journals.plos.org/plosone/article?id=10.1371/journal.pone.0084162 (visited on 01/19/2022).

[100] S. Fjær, L. Bø, K.-M. Myhr, Ø. Torkildsen, and S. Wergeland, "Magnetization transfer ratio does not correlate to myelin content in the brain in the MOG-EAE mouse model," en, *Neurochemistry International*, vol. 83-84, pp. 28–40, Apr. 2015. [Online]. Available: https://www.sciencedirect.com/science/article/pii/S0197018615000340 (visited on 01/19/2022).

[101] P. Dusek, E. Bahn, T. Litwin, *et al.*, "Brain iron accumulation in Wilson disease: A post mortem 7 Tesla MRI - histopathological study," eng, *Neuropathology and Applied Neurobiology*, vol. 43, no. 6, pp. 514–532, Oct. 2017.

[102] R. Yano, J. Hata, Y. Abe, *et al.*, "Quantitative temporal changes in DTI values coupled with histological properties in cuprizone-induced demyelination and remyelination," eng, *Neurochemistry International*, vol. 119, pp. 151–158, Oct. 2018.

[103] C. Wang, S. Foxley, O. Ansorge, *et al.*, "Methods for quantitative susceptibility and R2* mapping in whole post-mortem brains at 7T applied to amyotrophic lateral sclerosis," eng, *NeuroImage*, vol. 222, p. 117 216, Nov. 2020.

[104] Y. Abe, Y. Komaki, F. Seki, S. Shibata, H. Okano, and K. F. Tanaka, "Correlative study using structural MRI and super-resolution microscopy to detect structural alterations induced by long-term optogenetic stimulation of striatal medium spiny neurons," en, *Neurochemistry International*, vol. 125, pp. 163–174, May 2019. [Online]. Available: https://www.sciencedirect.com/science/article/pii/S0197018618304509 (visited on 12/29/2021).

[105] M. Mancini, A. Karakuzu, J. Cohen-Adad, M. Cercignani, T. E. Nichols, and N. Stikov, "An interactive meta-analysis of MRI biomarkers of myelin," *eLife*, vol. 9, S. Jbabdi, C. I. Baker, S. Jbabdi, and M. Does, Eds., e61523, Oct. 2020, Publisher: eLife Sciences Publications, Ltd. [Online]. Available: https://doi.org/10.7554/eLife.61523 (visited on 11/05/2021).

[106] A. Seewann, H. Vrenken, P. van der Valk, *et al.*, "Diffusely Abnormal White Matter in Chronic Multiple Sclerosis: Imaging and Histopathologic Analysis," *Archives of Neurology*, vol. 66, no. 5, pp. 601–609, May 2009. [Online]. Available: https://doi.org/10.1001/archneurol.2009.57 (visited on 12/29/2021).

[107] M. Bulk, B. Kenkhuis, L. M. van der Graaf, J. J. Goeman, R. Natté, and L. van der Weerd, "Postmortem T2*- Weighted MRI Imaging of Cortical Iron Reflects Severity of Alzheimer's Disease," eng, *Journal of Alzheimer's disease: JAD*, vol. 65, no. 4, pp. 1125–1137, 2018.

[108] V. Wiggermann, S. Hametner, E. Hernández-Torres, *et al.*, "Susceptibility-sensitive MRI of multiple sclerosis lesions and the impact of normal-appearing white matter changes," eng, *NMR in biomedicine*, vol. 30, no. 8, Aug. 2017.

[109] F. Bagnato, S. Hametner, E. Boyd, *et al.*, "Untangling the R2* contrast in multiple sclerosis: A combined MRI-histology study at 7.0 Tesla," eng, *PloS One*, vol. 13, no. 3, e0193839, 2018.

[110] N. Farahani, A. V. Parwani, and L. Pantanowitz, "Whole slide imaging in pathology: Advantages, limitations, and emerging perspectives," English, *Pathology and Laboratory Medicine International*, vol. 7, pp. 23–33, Jun. 2015, Publisher: Dove Press. [Online]. Available: `https://www.dovepress.com/whole-slide-imaging-in-pathology-advantages-limitations-and-emerging-p-peer-reviewed-fulltext-article-PLMI` (visited on 02/08/2022).

[111] M. N. Gurcan, L. Boucheron, A. Can, A. Madabhushi, N. Rajpoot, and B. Yener, "Histopathological Image Analysis: A Review," *IEEE reviews in biomedical engineering*, vol. 2, pp. 147–171, 2009. [Online]. Available: `https://www.ncbi.nlm.nih.gov/pmc/articles/PMC2910932/` (visited on 02/08/2022).

[112] M. T. McCann, J. A. Ozolek, C. A. Castro, B. Parvin, and J. Kovacevic, "Automated Histology Analysis: Opportunities for signal processing," *IEEE Signal Processing Magazine*, vol. 32, no. 1, pp. 78–87, Jan. 2015, Conference Name: IEEE Signal Processing Magazine.

[113] A. Madabhushi and G. Lee, "Image analysis and machine learning in digital pathology: Challenges and opportunities," eng, *Medical Image Analysis*, vol. 33, pp. 170–175, Oct. 2016.

[114] G. Bussolati and R. T. Radulescu, "Blocking Endogenous Peroxidases in Immunohistochemistry: A Mandatory, Yet Also Subtle Measure," en-US, *Applied Immunohistochemistry & Molecular Morphology*, vol. 19, no. 5, p. 484, Oct. 2011. [Online]. Available: `https://journals.lww.com/appliedimmunohist/Fulltext/2011/10000/Blocking_Endogenous_Peroxidases_in.19.aspx` (visited on 08/30/2022).

[115] M. Del Cerro, J. P. Cogen, and C. Del Cerro, "Retrospective demonstration of endogenous peroxidase activity in plastic-embedded tissues conventionally prepared for electron microscopy," eng, *The Journal of Histochemistry and Cytochemistry: Official Journal of the Histochemistry Society*, vol. 29, no. 7, pp. 874–876, Jul. 1981.

[116] G. Landini, G. Martinelli, and F. Piccinini, "Colour deconvolution: Stain unmixing in histological imaging," *Bioinformatics*, vol. 37, no. 10, pp. 1485–1487, May 2021. [Online]. Available: `https://doi.org/10.1093/bioinformatics/btaa847` (visited on 01/19/2022).

[117] E. L. Clarke and D. Treanor, "Colour in digital pathology: A review," eng, *Histopathology*, vol. 70, no. 2, pp. 153–163, Jan. 2017.

[118] D. J. Geijs, M. Intezar, J. A. W. M. v. d. Laak, and G. J. S. Litjens, "Automatic color unmixing of IHC stained whole slide images," in *Medical Imaging 2018: Digital Pathology*, vol. 10581, SPIE, Mar. 2018, pp. 165–171. [Online]. Available: `https://www.spiedigitallibrary.org/conference-proceedings-of-spie/10581/105810L/Automatic-color-unmixing-of-IHC-stained-whole-slide-images/10.1117/12.2293734.full` (visited on 01/19/2022).

[119] P. Bankhead, M. B. Loughrey, J. A. Fernández, *et al.*, "QuPath: Open source software for digital pathology image analysis," en, *Scientific Reports*, vol. 7, no. 1, p. 16 878, Dec. 2017, Number: 1 Publisher: Nature Publishing Group. [Online]. Available: `https://www.nature.com/articles/s41598-017-17204-5` (visited on 09/20/2023).

[120] C. A. Schneider, W. S. Rasband, and K. W. Eliceiri, "NIH Image to ImageJ: 25 years of image analysis," en, *Nature Methods*, vol. 9, no. 7, pp. 671–675, Jul. 2012, Number: 7 Publisher: Nature Publishing Group. [Online]. Available: https://www.nature.com/articles/nmeth.2089 (visited on 09/20/2023).

[121] M. Macenko, M. Niethammer, J. S. Marron, *et al.*, "A method for normalizing histology slides for quantitative analysis," in *2009 IEEE International Symposium on Biomedical Imaging: From Nano to Macro*, ISSN: 1945-8452, Jun. 2009, pp. 1107–1110.

[122] A. Vahadane, T. Peng, A. Sethi, *et al.*, "Structure-Preserving Color Normalization and Sparse Stain Separation for Histological Images," eng, *IEEE transactions on medical imaging*, vol. 35, no. 8, pp. 1962–1971, Aug. 2016.

[123] D. Carey, N. Wijayathunga, A. Bulpitt, and D. Treanor, "A Novel Approach for the Colour Deconvolution of Multiple Histological Stains," Jul. 2015. [Online]. Available: https://www.semanticscholar.org/paper/A-Novel-Approach-for-the-Colour-Deconvolution-of-Carey-Wijayathunga/0e1531ea514fe31c046d4cd006b1c73bd7372d9d (visited on 09/20/2023).

[124] N. Otsu, "A Threshold Selection Method from Gray-Level Histograms," *IEEE Transactions on Systems, Man, and Cybernetics*, vol. 9, no. 1, pp. 62–66, Jan. 1979, Conference Name: IEEE Transactions on Systems, Man, and Cybernetics.

[125] X.-c. Yuan, L.-s. Wu, and Q. Peng, "An improved Otsu method using the weighted object variance for defect detection," en, *Applied Surface Science*, vol. 349, pp. 472–484, Sep. 2015. [Online]. Available: https://www.sciencedirect.com/science/article/pii/S0169433215011319 (visited on 01/19/2022).

[126] S. Butterworth, "On the theory of filter amplifiers," *Experimental Wireless and the Wireless Engineer*, vol. 7, pp. 536–541, 1930.

[127] P. Virtanen, R. Gommers, T. E. Oliphant, *et al.*, "SciPy 1.0: Fundamental algorithms for scientific computing in Python," en, *Nature Methods*, vol. 17, no. 3, pp. 261–272, Mar. 2020, Number: 3 Publisher: Nature Publishing Group. [Online]. Available: https://www.nature.com/articles/s41592-019-0686-2 (visited on 08/26/2022).

[128] I. N. Huszar, M. Pallebage-Gamarallage, S. Bangerter-Christensen, *et al.*, "Tensor image registration library: Deformable registration of stand-alone histology images to whole-brain post-mortem MRI data," *NeuroImage*, vol. 265, p. 119 792, Jan. 2023. [Online]. Available: https://www.sciencedirect.com/science/article/pii/S1053811922009132 (visited on 09/20/2023).

[129] F. Grussu, T. Schneider, C. Tur, *et al.*, "Neurite dispersion: A new marker of multiple sclerosis spinal cord pathology?" *Annals of Clinical and Translational Neurology*, vol. 4, no. 9, pp. 663–679, Aug. 2017. [Online]. Available: https://www.ncbi.nlm.nih.gov/pmc/articles/PMC5590517/ (visited on 12/29/2021).

[130] M. Khodanovich, A. Pishchelko, V. Glazacheva, *et al.*, "Quantitative Imaging of White and Gray Matter Remyelination in the Cuprizone Demyelination Model Using the Macromolecular Proton Fraction," en, *Cells*, vol. 8, no. 10, p. 1204, Oct. 2019, Number: 10 Publisher: Multidisciplinary Digital Publishing Institute. [Online]. Available: https://www.mdpi.com/2073-4409/8/10/1204 (visited on 01/04/2022).

[131] J. Praet, N. V. Manyakov, L. Muchene, *et al.*, "Diffusion kurtosis imaging allows the early detection and longitudinal follow-up of amyloid--induced pathology," *Alzheimer's Research & Therapy*, vol. 10, no. 1, p. 1, Jan. 2018. [Online]. Available: https://doi.org/10.1186/s13195-017-0329-8 (visited on 12/29/2021).

[132] C. Kozlowski and R. M. Weimer, "An Automated Method to Quantify Microglia Morphology and Application to Monitor Activation State Longitudinally In Vivo," en, *PLOS ONE*, vol. 7, no. 2, e31814, Feb. 2012, Publisher: Public Library of Science. [Online]. Available: https://journals.plos.org/plosone/article?id=10.1371/journal.pone.0031814 (visited on 01/19/2022).

[133] A. Janowczyk, R. Zuo, H. Gilmore, M. Feldman, and A. Madabhushi, "HistoQC: An Open-Source Quality Control Tool for Digital Pathology Slides," eng, *JCO clinical cancer informatics*, vol. 3, pp. 1–7, Apr. 2019.

[134] Z. Liang, C. H. Lee, T. M. Arefin, *et al.*, "Virtual mouse brain histology from multi-contrast MRI via deep learning," *eLife*, vol. 11, S. Jbabdi, F. P. de Lange, and S. Jbabdi, Eds., e72331, Jan. 2022, Publisher: eLife Sciences Publications, Ltd. [Online]. Available: https://doi.org/10.7554/eLife.72331 (visited on 09/20/2023).

[135] B. C. Tendler, S. Foxley, M. Hernandez-Fernandez, *et al.*, "Use of multi-flip angle measurements to account for transmit inhomogeneity and non-Gaussian diffusion in DW-SSFP," en, *NeuroImage*, vol. 220, p. 117 113, Oct. 2020. [Online]. Available: https://www.sciencedirect.com/science/article/pii/S1053811920305991 (visited on 11/05/2021).

[136] D. Z. L. Kor, S. Jbabdi, I. N. Huszar, *et al.*, "An automated pipeline for extracting histological stain area fraction for voxelwise quantitative MRI-histology comparisons," en, *NeuroImage*, vol. 264, p. 119 726, Dec. 2022. [Online]. Available: https://www.sciencedirect.com/science/article/pii/S1053811922008473 (visited on 11/13/2022).

[137] M. Jenkinson, P. Bannister, M. Brady, and S. Smith, "Improved optimization for the robust and accurate linear registration and motion correction of brain images," eng, *NeuroImage*, vol. 17, no. 2, pp. 825–841, Oct. 2002.

[138] Y. Zhang, M. Brady, and S. Smith, "Segmentation of brain MR images through a hidden Markov random field model and the expectation-maximization algorithm," eng, *IEEE transactions on medical imaging*, vol. 20, no. 1, pp. 45–57, Jan. 2001.

[139] P. J. Huber, "Robust Statistics," en, in *International Encyclopedia of Statistical Science*, M. Lovric, Ed., Berlin, Heidelberg: Springer, 2011, pp. 1248–1251. [Online]. Available: https://doi.org/10.1007/978-3-642-04898-2_594 (visited on 01/19/2022).

[140] U. Grömping, "Variable importance in regression models," en, *WIREs Computational Statistics*, vol. 7, no. 2, pp. 137–152, 2015, _eprint: https://onlinelibrary.wiley.com/doi/pdf/10.1002/wics.1346. [Online]. Available: https://onlinelibrary.wiley.com/doi/abs/10.1002/wics.1346 (visited on 10/11/2021).

[141] J. M. Peters, R. R. Struyven, A. K. Prohl, *et al.*, "White matter mean diffusivity correlates with myelination in tuberous sclerosis complex," eng, *Annals of Clinical and Translational Neurology*, vol. 6, no. 7, pp. 1178–1190, Jul. 2019.

[142] A. S. Shatil, M. N. Uddin, K. M. Matsuda, and C. R. Figley, "Quantitative Ex Vivo MRI Changes due to Progressive Formalin Fixation in Whole Human Brain Specimens: Longitudinal Characterization of Diffusion, Relaxometry, and Myelin Water Fraction Measurements at 3T," *Frontiers in Medicine*, vol. 5, 2018. [Online]. Available: https://www.frontiersin.org/article/10.3389/fmed.2018.00031 (visited on 01/19/2022).

[143] J. A. McNab, S. Jbabdi, S. C. L. Deoni, G. Douaud, T. E. J. Behrens, and K. L. Miller, "High resolution diffusion-weighted imaging in fixed human brain using diffusion-weighted steady state free precession," eng, *NeuroImage*, vol. 46, no. 3, pp. 775–785, Jul. 2009.

[144] S. Foxley, S. Jbabdi, S. Clare, *et al.*, "Improving diffusion-weighted imaging of post-mortem human brains: SSFP at 7 T," eng, *NeuroImage*, vol. 102 Pt 2, pp. 579–589, Nov. 2014.

[145] S.-W. Sun, J. J. Neil, H.-F. Liang, *et al.*, "Formalin fixation alters water diffusion coefficient magnitude but not anisotropy in infarcted brain," eng, *Magnetic Resonance in Medicine*, vol. 53, no. 6, pp. 1447–1451, Jun. 2005.

[146] S.-W. Sun, J. J. Neil, and S.-K. Song, "Relative indices of water diffusion anisotropy are equivalent in live and formalin-fixed mouse brains," eng, *Magnetic Resonance in Medicine*, vol. 50, no. 4, pp. 743–748, Oct. 2003.

[147] A. Roebroeck, K. L. Miller, and M. Aggarwal, "Ex vivo diffusion MRI of the human brain: Technical challenges and recent advances," eng, *NMR in biomedicine*, vol. 32, no. 4, e3941, Apr. 2019.

[148] H. Hakkarainen, A. Sierra, S. Mangia, *et al.*, "MRI relaxation in the presence of fictitious fields correlates with myelin content in normal rat brain," en, *Magnetic Resonance in Medicine*, vol. 75, no. 1, pp. 161–168, 2016, _eprint: https://onlinelibrary.wiley.com/doi/pdf/10.1002/mrm.25590. [Online]. Available: https://onlinelibrary.wiley.com/doi/abs/10.1002/mrm.25590 (visited on 01/19/2022).

[149] B. M. Davis, M. Salinas-Navarro, M. F. Cordeiro, L. Moons, and L. De Groef, "Characterizing microglia activation: A spatial statistics approach to maximize information extraction," en, *Scientific Reports*, vol. 7, no. 1, p. 1576, May 2017, Number: 1 Publisher: Nature Publishing Group. [Online]. Available: https://www.nature.com/articles/s41598-017-01747-8 (visited on 08/26/2022).

[150] C. Guglielmetti, J. Veraart, E. Roelant, *et al.*, "Diffusion kurtosis imaging probes cortical alterations and white matter pathology following cuprizone induced demyelination and spontaneous remyelination," *NeuroImage*, vol. 125, pp. 363–377, Jan. 2016. [Online]. Available: https://www.sciencedirect.com/science/article/pii/S1053811915009635 (visited on 12/25/2023).

[151] J. Zhuo, S. Xu, J. L. Proctor, *et al.*, "Diffusion kurtosis as an in vivo imaging marker for reactive astrogliosis in traumatic brain injury," *NeuroImage*, Neuroergonomics: The human brain in action and at work, vol. 59, no. 1, pp. 467–477, Jan. 2012. [Online]. Available: https://www.sciencedirect.com/science/article/pii/S1053811911008275 (visited on 12/25/2023).

[152] P.-L. Chiang, H.-L. Chen, C.-H. Lu, *et al.*, "White matter damage and systemic inflammation in Parkinson's disease," *BMC Neuroscience*, vol. 18, no. 1, p. 48, Jun. 2017. [Online]. Available: https://doi.org/10.1186/s12868-017-0367-y (visited on 11/09/2021).

[153] A. Samara, T. Murphy, J. Strain, *et al.*, "Neuroinflammation and White Matter Alterations in Obesity Assessed by Diffusion Basis Spectrum Imaging," *Frontiers in Human Neuroscience*, vol. 13, 2020. [Online]. Available: https://www.frontiersin.org/article/10.3389/fnhum.2019.00464 (visited on 01/19/2022).

[154] M. Taquet, A. Jankovski, G. Rensonnet, *et al.*, "Extra-axonal restricted diffusion as an in-vivo marker of reactive microglia," eng, *Scientific Reports*, vol. 9, no. 1, p. 13 874, Sep. 2019.

[155] H. Rafipoor, Y.-Q. Zheng, L. Griffanti, S. Jbabdi, and M. Cottaar, "Identifying microstructural changes in diffusion MRI; How to circumvent parameter degeneracy," en, *NeuroImage*, vol. 260, p. 119 452, Oct. 2022. [Online]. Available: https://www.sciencedirect.com/science/article/pii/S1053811922005638 (visited on 11/01/2022).

[156] J. Y. Kwan, S. Y. Jeong, P. Van Gelderen, *et al.*, "Iron accumulation in deep cortical layers accounts for MRI signal abnormalities in ALS: Correlating 7 tesla MRI and pathology," eng, *PloS One*, vol. 7, no. 4, e35241, 2012.

[157] U. W. Kaunzner, Y. Kang, S. Zhang, *et al.*, "Quantitative susceptibility mapping identifies inflammation in a subset of chronic multiple sclerosis lesions," eng, *Brain: A Journal of Neurology*, vol. 142, no. 1, pp. 133–145, Jan. 2019.

[158] M. K. Jha, S. Jeon, and K. Suk, "Glia as a Link between Neuroinflammation and Neuropathic Pain," *Immune Network*, vol. 12, no. 2, pp. 41–47, Apr. 2012. [Online]. Available: https://www.ncbi.nlm.nih.gov/pmc/articles/PMC3382663/ (visited on 09/20/2023).

[159] O. M. Baksalary and G. Trenkler, "The Moore–Penrose inverse: A hundred years on a frontline of physics research," en, *The European Physical Journal H*, vol. 46, no. 1, p. 9, Apr. 2021. [Online]. Available: https://doi.org/10.1140/epjh/s13129-021-00011-y (visited on 09/20/2023).

[160] P. Cook, Y. Bai, S. Nedjati-Gilani, *et al.*, "Camino: Open-source diffusion-mri reconstruction and processing," in *14th Scientific Meeting of the International Society for Magnetic Resonance in Medicine*, 2006, p. 2759.

[161] J. Veraart, D. Nunes, U. Rudrapatna, *et al.*, "Noninvasive quantification of axon radii using diffusion MRI," *eLife*, vol. 9, F. P. de Lange, B. Forstmann, B. Forstmann, S. Jbabdi, and R. Mulkern, Eds., e49855, Feb. 2020, Publisher: eLife Sciences Publications, Ltd. [Online]. Available: https://doi.org/10.7554/eLife.49855 (visited on 11/01/2022).

[162] M. G. Hall and D. C. Alexander, "Convergence and Parameter Choice for Monte-Carlo Simulations of Diffusion MRI," *IEEE Transactions on Medical Imaging*, vol. 28, no. 9, pp. 1354–1364, Sep. 2009, Conference Name: IEEE Transactions on Medical Imaging.

[163] D. C. Van Essen, S. M. Smith, D. M. Barch, *et al.*, "The WU-Minn Human Connectome Project: An overview," eng, *NeuroImage*, vol. 80, pp. 62–79, Oct. 2013.

[164] J. .-. Tournier, F. Calamante, D. G. Gadian, and A. Connelly, "Direct estimation of the fiber orientation density function from diffusion-weighted MRI data using spherical deconvolution," *NeuroImage*, vol. 23, no. 3, pp. 1176–1185, Nov. 2004. [Online]. Available: https://www.sciencedirect.com/science/article/pii/S1053811904004100 (visited on 09/20/2023).

[165] M. Kazhdan, T. Funkhouser, and S. Rusinkiewicz, "Rotation Invariant Spherical Harmonic Representation of 3D Shape Descriptors," English, ISSN: 1727-8384, 2003, pp. 156–165.

[166] A. F. D. Howard, I. N. Huszar, A. Smart, *et al.*, "An open resource combining multi-contrast MRI and microscopy in the macaque brain," en, *Nature Communications*, vol. 14, no. 1, p. 4320, Jul. 2023, Number: 1 Publisher: Nature Publishing Group. [Online]. Available: https://www.nature.com/articles/s41467-023-39916-1 (visited on 09/20/2023).

[167] A. Howard, I. N. Huszar, S. Zhu, *et al.*, "Towards whole-brain, quantitative characterisation of microscopy-derived microstructure in the bigmac dataset," in *Proceedings of the 31st Annual Meeting of the ISMRM*, Toronto, Canada, 2023.

[168] S.-K. Song, J. Yoshino, T. Q. Le, *et al.*, "Demyelination increases radial diffusivity in corpus callosum of mouse brain," eng, *NeuroImage*, vol. 26, no. 1, pp. 132–140, May 2005.

[169] V. A. Janve, Z. Zu, S.-Y. Yao, *et al.*, "The radial diffusivity and magnetization transfer pool size ratio are sensitive markers for demyelination in a rat model of type III multiple sclerosis (MS) lesions," *NeuroImage*, vol. 74, pp. 298–305, Jul. 2013. [Online]. Available: https://www.sciencedirect.com/science/article/pii/S1053811913001614 (visited on 09/20/2023).

[170] A. MacKay, K. Whittall, J. Adler, D. Li, D. Paty, and D. Graeb, "In vivo visualization of myelin water in brain by magnetic resonance," eng, *Magnetic Resonance in Medicine*, vol. 31, no. 6, pp. 673–677, Jun. 1994.

[171] C. Tisca, M. Tachrount, A. Smart, *et al.*, "Linking mri to histology in the mouse brain: A framework for data acquisition and pre-processing," in *Proceedings of the Annual Meeting of the OHBM*, Montreal, 2023.

[172] R. Schurr and A. A. Mezer, "The glial framework reveals white matter fiber architecture in human and primate brains," eng, *Science (New York, N.Y.)*, vol. 374, no. 6568, pp. 762–767, Nov. 2021.

[173] R. Callaghan, D. C. Alexander, M. Palombo, and H. Zhang, "ConFiG: Contextual Fibre Growth to generate realistic axonal packing for diffusion MRI simulation," *NeuroImage*, vol. 220, p. 117 107, Oct. 2020. [Online]. Available: https://www.sciencedirect.com/science/article/pii/S1053811920305930 (visited on 09/20/2023).

[174] M. Palombo, D. C. Alexander, and H. Zhang, "A generative model of realistic brain cells with application to numerical simulation of the diffusion-weighted MR signal," eng, *NeuroImage*, vol. 188, pp. 391–402, Mar. 2019.

[175] J. R. Epp, Y. Niibori, H.-L. (Hsiang, *et al.*, "Optimization of CLARITY for Clearing Whole-Brain and Other Intact Organs," en, *eNeuro*, vol. 2, no. 3, May 2015, Publisher: Society for Neuroscience Section: Methods/New Tools. [Online]. Available: https://www.eneuro.org/content/2/3/ENEURO.0022-15.2015 (visited on 12/25/2023).

[176] C. Sudlow, J. Gallacher, N. Allen, *et al.*, "UK biobank: An open access resource for identifying the causes of a wide range of complex diseases of middle and old age," eng, *PLoS medicine*, vol. 12, no. 3, e1001779, Mar. 2015.

[177] K. L. Miller, F. Alfaro-Almagro, N. K. Bangerter, *et al.*, "Multimodal population brain imaging in the UK Biobank prospective epidemiological study," *Nature neuroscience*, vol. 19, no. 11, pp. 1523–1536, Nov. 2016. [Online]. Available: https://www.ncbi.nlm.nih.gov/pmc/articles/PMC5086094/ (visited on 03/15/2023).

[178] K. A. Wartolowska and A. J. Webb, "White matter damage due to pulsatile versus steady blood pressure differs by vascular territory: A cross-sectional analysis of the UK Biobank cohort study," en, *Journal of Cerebral Blood Flow & Metabolism*, vol. 42, no. 5, pp. 802–810, May 2022, Publisher: SAGE Publications Ltd STM. [Online]. Available: https://doi.org/10.1177/0271678X211058803 (visited on 02/23/2023).

[179] A. Alotaibi, A. Podlasek, A. AlTokhis, *et al.*, *White Matter Microstructural Alteration in Type 2 Diabetes: A Combined UK Biobank Study of Diffusion Tensor Imaging and Neurite Orientation Dispersion and Density Imaging*, en, Pages: 2022.07.09.22277453, Jul. 2022. [Online]. Available: https://www.medrxiv.org/content/10.1101/2022.07.09.22277453v1 (visited on 02/23/2023).

[180] P. McCarthy, *Funpack*, Apr. 2023. [Online]. Available: https://zenodo.org/record/7837337 (visited on 09/21/2023).

[181] F. Alfaro-Almagro, P. McCarthy, S. Afyouni, *et al.*, "Confound modelling in UK Biobank brain imaging," en, *NeuroImage*, vol. 224, p. 117 002, Jan. 2021. [Online]. Available: https://www.sciencedirect.com/science/article/pii/S1053811920304882 (visited on 03/30/2023).

[182] S. Wakana, A. Caprihan, M. M. Panzenboeck, *et al.*, "Reproducibility of quantitative tractography methods applied to cerebral white matter," eng, *NeuroImage*, vol. 36, no. 3, pp. 630–644, Jul. 2007.

[183] K. Hua, J. Zhang, S. Wakana, *et al.*, "Tract Probability Maps in Stereotaxic Spaces: Analyses of White Matter Anatomy and Tract-Specific Quantification," *NeuroImage*, vol. 39, no. 1, pp. 336–347, Jan. 2008. [Online]. Available: https://www.ncbi.nlm.nih.gov/pmc/articles/PMC2724595/ (visited on 09/21/2023).

[184] S. Oparil, M. C. Acelajado, G. L. Bakris, *et al.*, "Hypertension," *Nature reviews. Disease primers*, vol. 4, p. 18 014, Mar. 2018. [Online]. Available: https://www.ncbi.nlm.nih.gov/pmc/articles/PMC6477925/ (visited on 09/21/2023).

[185] C. McCracken, Z. Raisi-Estabragh, M. Veldsman, *et al.*, "Multi-organ imaging demonstrates the heart-brain-liver axis in UK Biobank participants," en, *Nature Communications*, vol. 13, no. 1, p. 7839, Dec. 2022, Number: 1 Publisher: Nature Publishing Group. [Online]. Available: https://www.nature.com/articles/s41467-022-35321-2 (visited on 09/21/2023).